# Complex decompression and fragmentation of mingled andesite magmas driving multi-phase Plinian eruptions at Mt. Taranaki, New Zealand

Rafael Torres-Orozco [a, *], Shane J. Cronin [b], Natalia Pardo [c], Szabolcs Kósik [d], Ingrid Ukstins [b, e], Mirja Heinrich [f], Peter D. Lee [g, h]

[a] Centro de Ciencias de la Tierra, Universidad Veracruzana, Francisco J. Moreno 207, Xalapa, Veracruz 91090, México

[b] School of Environment, The University of Auckland, Private Bag 92019, Auckland 1142, New Zealand

[c] Departamento de Geociencias, Universidad de Los Andes, Cr 1 #18A-12, Bogotá, Colombia

[d] Volcanic Risk Solutions, Massey University, Private Bag 11 222, Palmerston North 4442, New Zealand

[e] Department of Earth and Environmental Sciences, The University of Iowa, 121 Trowbridge Hall, Iowa City, Iowa 52242, USA

[f] GEOMAR, Helmholtz Centre for Ocean Research Kiel, Wischhofstraße 1-3, 24148 Kiel, Germany

[g] Department of Mechanical Engineering, University College London, Torrington Place, London WC1E 7JE, United Kingdom

[h] Materials, Structures and Manufacturing Group at Harwell, Research Complex at Harwell, Rutherford Appleton Laboratory, Didcot, Oxfordshire OX11 0FA, United Kingdom

*Corresponding author. Tel.: +52 228 1820272. E-mail address: raftorres@uv.mx (R. Torres-Orozco)

## ABSTRACT

Estimating the kinetics of andesite magma vesiculation and crystallization modifying rheology inside volcanic plumbing systems before and during multiple eruptive phases, as well as their relationship with different magma storage and flow rates, are key for unraveling andesite Plinian eruption timescales,

fragmentation mechanisms, and shifts in eruption explosivity and style. This information is crucial for increasing knowledge on expected hazards and developing realistic eruption scenarios. In this work, we estimate conduit magma vesiculation and crystallization regulating rheology during the 3300 cal BP Upper Inglewood Plinian eruptive episode of Mount Taranaki, New Zealand. This episode comprised (i) onset, low-intensity, conduit-opening phases of dome-collapse PDCs; (ii) pre-climactic, highly explosive phases of diverse PDCs, of up to violent 18-km-runout lateral blasts; (iii) climactic phases of steady 22-km-high Plinian eruption columns; and (iv) waning phases of column-collapse PDCs. By employing synchrotron microtomography, combined with mineral/glass chemistry and electron-microscopy, we quantified 3D vesicle and crystal size and shape distributions in juvenile pyroclasts over time, and corresponding number densities ranging from 1.1 $x$ $10^5$ to 2.5 $x$ $10^6$ $mm^{-3}$ for vesicles, and from 8.0 $x$ $10^4$ to 5.1 $x$ $10^6$ $mm^{-3}$ for crystals. Our results indicate that tapering of chemically alike yet rheologically contrasting magmas over a multi-phase andesite eruptive episode is linked to: (a) mafic magma recharge and differentiation in multiple storage reservoirs at distinct crustal levels, (b) stepwise to rapid magma decompression while mingling, producing variable pre- and syn-eruptive degassing and crystallization, and (c) scaling melt viscosity, strain, and/or localized shear deformation inside evolving conduit geometries. Earliest and least explosive eruptive phases (± 2 $x$ $10^6$ kg $s^{-1}$) were produced at slowest rates of magma decompression (0.3 – 0.6 MPa $s^{-1}$), ascent (0.01 – 0.02 m $s^{-1}$) and strain (< 0.002 $s^{-1}$), driven by volatile diffusion and exsolution leading into simplest fragmentation mechanisms. All subsequent pre-climactic and Plinian phases (4 $x$ $10^7$ – 1 $x$ $10^8$ kg $s^{-1}$) were produced at either rapid or intermittent rates of magma decompression (2.0 – 6.0 MPa $s^{-1}$), ascent (0.06 – 0.2 m $s^{-1}$) and strain (> 0.003 – 0.010 $s^{-1}$), powered by combined magma volatile supersaturation and delayed disequilibrium degassing, decompression-induced microlite crystallization and rapid heterogeneous vesiculation kinetics, shear deformation and magma mingling. These processes enabled complex fragmentation mechanisms of the most rheologically homogeneous magmas. We discuss how changes in decompression and fragmentation regimes produce alternative eruption scenarios of andesite magmas.

**Keywords:** andesitic pyroclasts, andesite Plinian eruption, magma degassing, magma decompression, magma fragmentation, synchrotron microCT

## 1. Introduction

Multi-phase Plinian eruptive episodes at andesitic volcanoes are some of the most hazardous, complex and unpredictable due to consisting of series of eruptive phases in which volcanic activity of fluctuating intensity and seemingly erratic eruption style can be generated (e.g., Gurioli et al., 2005; Carazzo et al., 2012; Cronin et al., 2013; Romero et al., 2016; Torres-Orozco et al., 2017a; 2018; Maeno et al., 2019). This multi-phase volcanic activity is largely regulated by the kinetics of evolving magma processes acting at volcanic plumbing systems, and can encompass from relatively slow lava flows and domes ($< 10^6$ kg $s^{-1}$) to pyroclastic density currents (PDCs) and eruption columns able to quickly shift from low to high energy Plinian bursts (e.g., from $10^6$ to $10^8$ kg $s^{-1}$; Shea, 2017; Torres-Orozco et al., 2017b; Cassidy et al., 2018). The resulting eruption sequences make the scale, distribution, timescales and succession of hazards associated with long-lived Plinian eruptions difficult to anticipate, limiting risk decision makers at implementing best practices before and during volcanic crises. Thus, estimating rates of transfer of magma to the Earth's surface, as well as conduit dynamics controlling shifts in eruption intensity and style in Plinian eruptive episodes, are two of Volcanology's intrinsic main goals (e.g., Mader, 1998; Cashman and Blundy, 2000; Gonnermann and Manga, 2013; Cassidy et al., 2018; Caricchi et al., 2021), critical for best assessing potential multi-phase eruption scenarios (e.g., Torres-Orozco et al., 2018; Heinrich et al., 2020).

Andesite magma dynamics at upper volcanic conduits driving Plinian eruptions span a wide range in magma rheology and in fragmentation mechanisms produced paradoxically by even small differences in crystal and volatile contents (e.g., Cashman and Blundy, 2000; Blundy et al., 2006; Pardo et al., 2014; Pleše et al., 2018; 2019; Heinrich et al., 2020). Whilst fragmentation of low-Si andesite magmas compares to that controlling basaltic and basaltic-andesite explosions, generally depending on the

dynamics of late-stage crystallization and heterogeneous vesiculation kinetics (e.g., Blundy et al., 2006; Sable et al., 2006; Pérez et al., 2009; Heinrich et al., 2020; Lormand et al., 2020; Arzilli et al., 2019; 2022); high-Si andesite magmas fragment via mechanisms similar to those acting in rhyolitic outbursts, generally depending on the kinetics of vesiculation of volatile supersaturated magmas, rapid decompression and/or shear dynamics, and on mingling/mixing with mafic melts replenishing plumbing systems (e.g., Alidibirov and Dingwell, 2000; Mangan and Sisson, 2000; Gardner, 2007; Palladino et al., 2008; Pardo et al., 2014; Rotella et al., 2014; Paredes-Mariño et al., 2017). Additional complexities in andesite volcanism arise from evidences of mingling/mixing and shearing between different andesite magmas of near-identical chemical composition yet contrasting rheology, possibly reflecting interplaying low-Si and high-Si melt variants, commonly difficult to analyze separately (e.g., Platz et al., 2007). Such interactions between relatively different andesites can generate intricate sequences of magmatic processes that, all together, might be unique to the range of intermediate chemical compositions.

Deciphering the complexity of magma degassing and fragmentation is key for understanding how andesite explosive volcanism is triggered, why either long-lived (multi-phase) or short-lived andesite Plinian-scale eruptive episodes are produced, and what shallow conduit processes and eruption mechanisms both enable and control shifts in eruption style and intensity. In this work, we have estimated the kinetics of upper conduit magma vesiculation and crystallization, analyzed continuous mingling and shearing between rheologically different andesite magmas, estimated magma decompression, and inferred magma fragmentation mechanisms driving each of the eight eruptive phases that comprise the 3300 cal BP Upper Inglewood Plinian eruptive episode of the andesitic stratovolcano Mount Taranaki in New Zealand (Torres-Orozco et al., 2017a; 2017b; 2018).

The Upper Inglewood's eruptive phases represent a wide variety of volcanic activity escalating from low-energy, gravity-driven yet explosive summit dome-collapse PDCs; through to pre-climactic, highly unsteady and energetic laterally directed blast-type PDCs; to climactic and sustained Plinian eruption

columns, followed by column-collapse PDCs during final eruption waning (Torres-Orozco et al., 2017b; 2018). Deposits from all eruptive phases comprise juvenile pyroclasts of diverse volume percentages, sizes and geometries of vesicles and crystals, that have recorded micro-scale evidences of the upper conduit magma dynamics and fragmentation driving fluctuating intensities and eruption mechanisms in the Upper Inglewood. For completing this work, we collected evidences from mineral and glass chemistry, geothermobarometry, and conventional microanalyses of textures in two-dimensions; and quantified in three-dimensions, using synchrotron microtomography, the stratigraphically organized (i.e., relative time-constrained) pyroclast microtextures (e.g., vesicles, crystals, glass) formed during each of the eight eruptive phases of the Upper Inglewood. The results of this study reveal new insights into rates and complex interplay of series of upper conduit magma processes regulating andesite magma ascent and explosive volcanism overall, and driving long-lived andesite eruptive episodes formed by sequential phases of shifting styles and intensities of up to Plinian scale, applicable to investigate not only Taranaki but all similar andesitic stratovolcanoes.

## 2. Geological background

New Zealand's North Island lies over the south-Pacific convergent boundary between the Australian and Pacific Plates, with the latter being subducted along the Hikurangi Trough (Henrys et al., 2003; Fig. 1). The ca. 170 ka to AD 1800 Mt. Taranaki (Alloway et al., 1995) is New Zealand's westernmost (400 km west of the Trough) and largest (12 $km^3$- volume, Zernack et al., 2011) andesitic stratovolcano associated with Hikurangi's subduction system (Price et al., 2005), and is the youngest and southernmost volcano of the NNW-SSE trending chain of four < 1.75 Ma volcanoes that form the Taranaki Volcanic Lineament (TVL; Neall, 1972; Fig. 1). Volcanic products of the TVL cover the entire ca. 1500 $km^2$ Taranaki Peninsula, and cap Paleozoic-Cretaceous plutonic rocks of the Median Tectonic Zone (Mortimer et al., 1997), and 6 km-thick Cretaceous-Cenozoic water-saturated sediments of the Taranaki Basin (King and Thrasher, 1996). The eastern and western margins of the basin are marked, respectively, by active tectonics of the N-S striking compressional and trans-tensional Taranaki Fault Zone, and the NE-SW

trending extensional Cape Egmont Fault Zone (Fig. 1; Stagpoole and Nicol, 2008; Cronin et al., 2021), which have been seismically detected down to the locally 25 – 40 km-deep base of the crust (Sherburn et al., 2006).

Mt. Taranaki's long-term volcanic history consists of cycles of cone growth to a critical volume/height during explosive and effusive volcanism, followed by catastrophic edifice-collapse (Zernack et al., 2011). Last 30,000 years' explosive volcanism is represented by at least 20 tephra formations mapped in ring-plain soils (Neall, 1972; Alloway et al., 1995) and within lake and peat sediments (Turner et al., 2008b; 2009; 2011; Damaschke et al., 2017; Fig. 1). The present-day 2518 m-high Mt. Taranaki's edifice above 1400 m is younger than 10 ka (Cronin et al., 2021). Taranaki's uppermost cone is shaped by 2 – 0.4 ka lava flows (Downey et al., 1994), and the existing summit is formed by remnants of the youngest AD 1800 Sisters dome (Platz et al., 2012). The conical edifice symmetry is broken in the southeast by the 1966 m-high Fanthams Peak basaltic satellite cone (Fig. 1), which last erupted between 3000 and 1200 cal BP (Torres-Orozco et al., 2017a; 2017b).

The latest 5000 years of Taranaki's volcanism included minimum 16 sub-Plinian and Plinian andesite (54-60 wt.% $SiO_2$) and basalt to basaltic-andesite (47-54 wt.% $SiO_2$) eruptive episodes generated from either Mt. Taranaki's summit crater or Fanthams Peak's vent, respectively (Torres-Orozco et al., 2017a; 2017b; 2018). These Plinian episodes comprised multiple eruptive phases, ranging from (i) initial explosive summit dome-collapses and block-and-ash flows (BAF); through to (ii) pre-climactic, high-energy blast-type pyroclastic density currents (PDCs); to (iii) climactic eruption columns, and (iv) subsequent pumice flows from column-collapse. The climactic steady, oscillating, or partially collapsing eruption columns were 14 – 29 km-high, and ejected minimum volumes of $10^8$ – $10^9$ $m^3$ at mass discharge rates of $10^7$ – $10^8$ kg $s^{-1}$, producing magnitudes of 4 – 5 (Torres-Orozco et al., 2017b). The most explosive blast-type PDCs had the largest run-out distances of up to 18 km, and minimum volumes of $10^7$ $m^3$ (Torres-Orozco et al., 2017b).

### *2.1 The 3300 cal BP Upper Inglewood eruptive episode*

The 3300 cal BP Upper Inglewood eruptive episode (Uig, Torres-Orozco et al., 2017a; 2017b; 2018) was Mt. Taranaki's second largest late-Holocene Plinian event from the summit crater. The Uig erupted a minimum DRE volume of 0.16 $km^3$ at a mass discharge rate of 7.6 x $10^7$ kg $s^{-1}$, had a magnitude of 4.8, and formed the thickest PDCs' succession in the last 5000 years (Torres-Orozco et al., 2017b). Uig's pyroclastic deposits comprise eight different layers (Uig1 to Uig8, Fig. 2), which record distinct eruptive units that corresponded to diverse eruption intensities and styles during onset, climactic, and pre- and post-climactic eruptive phases (Torres-Orozco et al., 2017a; 2017b; 2018). The Uig started with conduit/vent opening, stepwise, explosive summit dome-collapse pulses that produced a series of BAF units spreading over the eastern flanks (Fig. 1). These onset events imply pre-Uig lava-dome effusion on top of Taranaki's summit, and gradual tapping of magma that produced layers Uig1 – Uig3 with predominantly dense andesitic clasts and minor pumice content (Fig. 2). The opening phase passed into violent pre-climactic eruptions that tapered fresh volatile-rich magmas that overpressurized the topmost part of the conduit, destroyed the remaining summit dome, and deep-down excavated the conduit. These eruptions produced high-energy, laterally directed, blast-type PDCs, which formed layers Uig4 – Uig6 consisting of particle-concentrated to dilute deposits of pumice, dense andesitic clasts, and accidental lithics (Fig. 2). These blast layers were deposited as far as 18 km east from the crater, near present-day town of Stratford (Fig. 1). A steady, 22 km-high Plinian eruption column developed in the climactic phase, and draped most of the eastern Taranaki Peninsula with 0.3 – 100 cm-thick fall deposits of layer Uig7 (Figs. 1 and 2). This Plinian column experienced minor marginal instability during the eruption, producing thin ash-rich PDC deposits until it fully collapsed and formed the PDC layer Uig8 (Fig. 2). Subsequent rain-triggered lahars rapidly remobilized Uig's uppermost primary deposits, for which, at present, the Uig8 is only preserved in scarce locations over Taranaki's upper cone.

## 3. Methods and terms

Detailed sample collection from bottom to top stratigraphic levels of every layer representing each of the eight eruptive phases of the Uig was completed at proximal sites on the volcano flanks, 1-3 km from

the summit (Fig. 1). In total, 40 samples were cleaned and dry sieved at 0.5ϕ intervals from -5ϕ to 4.5ϕ. For consistency in sample description and interpretation, we stuck to definitions of, e.g., Houghton and Wilson (1989), Gurioli et al. (2005; 2008), Polacci et al. (2006; 2009), Shea et al. (2010), and Cashman and Scheu (2015): 1) "vesicular" defines textures preserved in solidified pyroclasts and consisting in "vesicles" left behind by "bubbles" of volcanic gas that were trapped in magma as it was fragmented; 2) "vesicularity" is the volume percentage (vol.%) of vesicles in pyroclasts, ranging from poorly vesicular or dense (< 20 vol.%; incipiently vesicular in Houghton and Wilson, 1989) to highly vesicular or foamy (> 60 vol.%); 3) "microvesicular" refers to pyroclasts in which vesicles of < $10^6$ μm$^3$, < 150 μm-equivalent diameter (EqD), form ≥ 50 vol.% of bulk vesicularities; 4) "bubbles", interpreted from vesicles, refer to pockets of volatiles exsolving and growing in the erupting magma; and 5) "porosity" refers to all cavities preserved in pyroclasts due to both magma vesiculation and post-fragmentation expansion and cracking. Following Gurioli et al. (2005; 2008), Pardo et al. (2014) and Colombier et al. (2017), based on crystal size only, crystals were classified in phenocrysts (≥ $10^6$ μm$^3$ and 150 μm- EqD), microphenocrysts ($10^3$ – $10^6$ μm$^3$, 15-150 μm- EqD) and microlites (< $10^3$ μm$^3$ and 15 μm- EqD, and > 0.2 μm-maximum 2D resolution). "Highly" and "poorly crystalline" pyroclasts contain > 50 and < 20 vol.% crystals, respectively; whilst the rest of intermediate crystallinities were not specified. "Microcrystalline" refers to pyroclasts whose bulk crystallinities are mostly formed of microphenocrysts and/or microlites (≥ 50 vol.% bulk). "Banded" textures correspond to mixtures between vesicular and crystalline bands within pyroclasts.

### *3.1 Macro and 2D textural microanalyses*

Following Torres-Orozco et al. (2017b), componentry analysis (in vol.%) were completed by counting 350 particles/set in three sets of -1ϕ and 0.5ϕ modes each (0.5 – 0.2 vol.% uncertainties). Particles were classified into dense and vesicular juvenile clasts, and in non-juvenile (accidental) lithics (Fig. 2). Density data of all vesicular clasts were taken from Torres-Orozco et al. (2017b). Following procedures described in Torres-Orozco et al. (2017b) and references therein, bulk ($\rho_{bulk}$), skeletal ($\rho_{skel}$) and solid

($\rho_{sol}$) densities of 240 dense lapilli clasts (-3ϕ) were obtained (Appendix A) using a Micrometrics GeoPyc 1360 envelope density analyzer (± 1.1% reproducibility) and a $N_2$-based Quantachrome Ultrapycnometer (± 0.2% reproducibility) at Massey University (New Zealand). Using all density data, weighted average (wt. avg.) $\rho_{bulk}$ and $\rho_{sol}$ of each Uig layer were estimated (Fig. 2). Using a scanning electron microscope (SEM) at a constant 20 kV accelerating voltage at the Manawatu Microscopy and Imaging Centre, Massey University, backscatter photomicrographs of all vesicular clasts were obtained (50x to 2000x magnifications, 1 to 0.2 μm pixel-resolution). Using Avizo® software (Appendix B.1a), micrographs were binarized into solid and porous media, and further segmented into glass, crystal and vesicle phases (Fig. 3). Following Gurioli et al. (2005; 2008), Pardo et al. (2014) and Colombier et al. (2017), the 2D abundances of phenocrysts, microphenocrysts and microlites were resolved in 50x, 500x and 1000-2000x.

*3.2 3D textural microanalyses*

A total of 50 cylinders (± 1.2 mm-diameter) cored from Uig vesicular clasts (-2ϕ), spanning the complete range described in Torres-Orozco et al. (2017b), were imaged via phase-contrast x-rays computed microtomography (μCT) at the Imaging and Medical Beamline of the Australian Synchrotron. A total of 43 scans, divided in 5 slots of ± 10 scans each were completed. Each scan consists of 1000 radiographs at a voxel-size resolution of 0.647 μm, acquired at 30 keV accelerating voltage and 180° rotation in 0.1° angle steps. Flat-field corrections of background noise, and ring and zinger artifacts were completed, and radiographs were reconstructed into 3D volumes. Using ImageJ® and Avizo® (Appendix B.1a), all 43 μCT volumes were segmented into groundmass glass, vesicle and crystal phases (Fig. 4), and further divided into individual vesicle and crystal particles (Figs. 5 and 6). In agreement with Lin et al. (2015), Hughes et al. (2017) and Heinrich et al. (2020), a minimum of three to four voxels, making ± 1 $\mu m^3$, was considered representative of the smallest detectable particle. Larger particles were only measured up to $10^7$ $\mu m^3$ (± 312 μm-EqD). Some of the largest particles, corresponding to either permeable pathways of connected vesicles or crystal clusters, were not separated into individuals due to their

naturally connected character (e.g., Colombier et al., 2018). In agreement with Klug et al. (2002), Rotella et al. (2014) and Heinrich et al. (2020), these particle size limits exclude most post-fragmentation porosity (> 300 μm-EqD) and preserve utmost evidences of near-fragmentation conduit processes. Microlites were isolated from the rest of crystals using < $10^3$ $\mu m^3$ volume sieves (< 15 μm-EqD). Iron-titanium (Fe-Ti) oxide microlites were recognized due to their highest x-rays attenuation coefficients, whereas plagioclase microlites, having the lowest attenuation, required most 2D corrections. Quantifications of individual vesicles and crystals, and a series of textural and geometrical parameters (e.g., volume, EqD, 3D shape [ShpF], rugosity) were performed in Avizo® (Appendix B.1a-b). The rugosity of selected particles was used to evaluate particles of identical shape yet distinct edge morphology (e.g., euhedral to anhedral crystals of the same mineral). Vesicle and crystal shape and size distributions, and corresponding number densities, were computed following Gurioli et al. (2005), Proussevitch et al. (2007), Pardo et al. (2014) and Heinrich et al. (2020). Total numbers of vesicles were normalised to melt volume, and vesicle number densities (*VND*) corrected for groundmass crystallinity. Likewise, total crystal and microlite number densities (*CND* and *MND*) were calculated on the basis of melt volume and corrected for microvesicularity. All textural parameters were computed for every type of vesicular clast identified inside each Uig layer, and each layer's wt. avg. textural parameters were estimated.

### *3.3 Geochemistry and geothermobarometry*

Crystal and groundmass glass chemical compositions of the Uig vesicular clasts (Figs. 3 and 4) were analyzed using the JEOL JXA-8230 Superprobe of the Electron Microprobe (EMPA) Laboratory at the University of Iowa (USA) (Appendix C). Quantitative 3 – 5 μm spot focused (core-rim crystal transects) and defocused (groundmass glass) beam modes were employed. Previous Uig EMPA data of Damaschke et al. (2017) were also incorporated. Mineral stoichiometric formulas and classification were determined. For amphibole, procedures of Leake et al. (2004), and Locock (2014) and Li et al. (2020) based on Hawthorne et al. (2012), were employed. Fe-Ti oxides were classified according to Ghiorso and Evans

(2008). Amphibole geothermobarometry was performed using different combinations of selected glass, amphibole and plagioclase compositions, following a range of methods (Appendix C) included in software of Yavuz and Döner (2017). The barometer of Mutch et al. (2016) was preferred for low-*P* (≤ 100 MPa) estimates; otherwise, the most consistent *P-T* values from a range of methods were chosen. Single-clinopyroxene *P-T* meters were estimated following different methods (Appendix C) included in software of Yavuz (2013). Plagioclase and clinopyroxene liquidus *P-T* conditions were calculated in MELTS web service (Asimow and Ghiorso, 1998) with chemical data of Torres-Orozco et al. (2017b) and glass and mineral chemical compositions. Experimental, water-saturated liquidus models of Yoder (1965) and Burnham and Davis (1974), and amphibole stability experiments of Lledo and Jenkins (2008) and Mutch et al. (2016) were employed for testing all *P-T* results.

### *3.4 Estimation of physical eruption parameters*

Magma decompression rates (*dP/dt*) during the Uig were quantified using the *VND*- and *MND*-based decompression rate meters of Toramaru (2006) and Toramaru et al. (2008) (Appendix B.1b and B.2). Water diffusivity rates (*Dw*) were calculated following Toramaru (2006) using water contents ranging from 2 to 5 wt.%, and the results were further compared with Fanara et al. (2013) by extrapolating to lower temperatures. Values of surface tension for homogeneous bubble nucleation were calculated following equation 13 of Shea (2017), and compared with Bagdassarov et al. (2000) corrected by Shea (2017). A surface tension of 0.025 N $m^{-1}$ for heterogeneous bubble nucleation was taken from Cluzel et al. (2008). Both *VND* and *MND dP/dt* were calculated for every type of Uig vesicular clast inside each Uig layer, and each layer's wt. avg. *dP/dt* was also estimated. Mass discharge rates (*MDR*) and the effective conduit radius (*r* in meters) during eruption of each Uig layer were estimated following Shea (2017) (Appendix B.1b) using (i) a reference *MDR* of 7.6 x $10^7$ kg $s^{-1}$ reported in Torres-Orozco et al. (2017b) for the climactic Uig7 Plinian phase, (ii) each Uig layer's vol.% of every clast type (Fig. 2), and (iii) each layer's wt. avg. $\rho_{bulk}$ and wt. avg. heterogeneous *VND dP/dt*.

Relative buoyancy, viscosity, and strain rate of magmas close to fragmentation were estimated using the classical empirical relationship between bubble buoyancy and drag force (Marsh, 1984; Gonnermann and Manga, 2013) (Appendix B.1b). For doing this, we assumed: 1) uniform "diapiric" volumes of fixed magma foams approaching fragmentation at every eruptive phase, having a wt. avg. $\rho_{bulk}$ (i.e., $\rho$ of every type of Uig clast) and a radius ≈ conduit radius, rising at min. ascent rates from constant depths; and 2) fixed particle interactions during magma rise inside the upper conduit, equivalent to rheologically fixed homogeneous or heterogeneous magma foams. Minimum and maximum magma ascent rates (*U*) were estimated following Shea (2017) and Cassidy et al. (2018), and contrasted with *VND*- and *MND*-based water exsolution-derived *U* of Toramaru et al. (2008). Relative strain rates were roughly calculated by dividing *U* by the diameter of each corresponding magma diapir (Appendix B.1b and B.2).

## 4. Results

### *4.1 Textural classification of pyroclasts*

The Uig vesicular clasts span ranges of $\rho_{\text{bulk}}$ (700 – 2200 kg m$^{-3}$, Torres-Orozco et al., 2017b), bulk crystallinities (14 – 59 vol.%) and bulk vesicularities (15 – 64 vol.% via microanalyses, and 25 – 80 vol.% via pycnometry in Torres-Orozco et al., 2017b) (Table 1). In agreement with Torres-Orozco et al. (2017b), the vesicular clasts were classified into five types (Fig. 2): 1) Yellow-White Foamy Pumice (YWFP), 2) Yellow-White Crystalline Pumice (YWCP), 3) Grey Crystalline Pumice (GCP), 4) Grey Banded Pumice (GBP), and 5) Violet Crystalline Pumice (VCP). All types are ubiquitously microvesicular, i.e., microvesicles ≥ 80 cumulative (cum.) vol.% of bulk vesicularities (Fig. 7). Bulk vesicularities calculated from pycnometry are only 10 – 16 vol.% higher than those calculated via microanalyses, revealing that > 150 μm-diameter vesicles represent only minor fractions (Fig. 2). Similarly, all vesicular clasts are microcrystalline (i.e., microphenocrysts form 50 – 80 cum. vol.% of bulk crystallinities), and all but the YWFP are microlite-rich (i.e., 10 – 40 cum. vol.% microlites) (Fig. 7). In all cases, mineral assemblages comprise phenocrysts and microphenocrysts of plagioclase (9 – 41 vol.%), clinopyroxene (3 – 12 vol.%), amphibole (2 – 7 vol.%), and Fe-Ti oxides (0.2 – 1.8 vol.%; Fig.

3). In detail (Table 1), the YWFP stands out for having the lowermost $\rho_{bulk}$ of all pumice types, and a characteristic foamy appearance (Figs. 4 and 5) due to its highly vesicular and holohyaline groundmass (Fig. 3). YWCP's glassy vesicle walls are the finest, whereas GCP's vesicles are separated by thick rugged walls made of glass and spearing microlites (Figs. 3, 4 and 5). The GBP stands out for comprising two types of bands (Fig. 2): grey-YW crystalline (B1) and YW foamy (B2) (Figs. 3 to 5, and appendix B.1c). The VCP is the only vesicular clast type existing in all layers, has the lowermost vesicularities and the highest $\rho_{bulk}$, crystallinities and microlite contents.

The Uig dense clasts span variable $\rho_{bulk}$ (2300 – 2700 kg $m^{-3}$) and bulk crystallinities (10 – 94 vol.%), but negligible bulk vesicularities/porosities (avg. 5 – 8 and up to 14 vol.%) (Table 1); and were classified in four types (Fig. 2): 1) Dense Andesite Juveniles (AJ) and 2) "Old Dome" Accessory Dense Andesite Lithics (OD-AL), in agreement with Torres-Orozco et al. (2017b), 3) Accidental Altered Lithics (ALT), and 4) Accidental Intrusive Lithics (AIL). Both AJ and OD-AL comprise the same mineral species than the vesicular clasts. In detail (Table 1), the AJ is characterized by a defining dark (amphibole)-speckled light grey color (Fig. 2), whilst the OD-AL stands out for containing groundmass clinopyroxene and amphibole microlites exceeding plagioclase, which confer its typical white (plagioclase)-speckled dark grey groundmass color (Fig. 2). The ALT consists of light grey clasts having red/orange-stained faces and formed by quartz and hydrothermally altered grains (Fig. 2), whilst the AIL stands out for its fine-grained phaneritic texture (Fig. 2). ALT and AIL are, correspondingly, similar to Taranaki's sedimentary to metasedimentary xenoliths and plutonic xenoliths reported in Gruender et al. (2010).

### *4.2 Individual vesicle metrics*

All pumice types' vesicle shapes were classified in: 1) spherical (ShpF ≤ 1.5), 2) subspherical (ShpF = 1.6 – 2.5), 3) ellipsoidal (ShpF = 2.6 – 3.5), 4) coalesced (ShpF = 3.6 – 7.0), 5) fibrous tubular (ShpF = 7.1 – 12.0), and 6) complex (ShpF > 12.0) (Appendix B.1b). Vesicle size was organized in eight scaling orders of volume from 1 to $10^7$ $\mu m^3$, corresponding to EqD between 1 and 312 μm, respectively (Figs. 5 and 7). Of all pumice types, the YWFP comprises most $10^3$ – $10^4$ $\mu m^3$ subspherical vesicles, and has

the largest fractions of spherical vesicles (29 vol.%). YWCP and GCP have similar amounts of coalesced vesicles (4 – 8 vol.%) but contrasting vesicle sizes of $10^0$ – $10^2$ (5 – 10 vol.%) and $10^3$ – $10^5$ $\mu m^3$ (13 – 20 vol.%), respectively (Fig. 7). GBP-B1 is near identical to the YWCP, whereas GBP-B2 is formed by two contrasting vesicle populations of which modal > $10^6$ $\mu m^3$ fibrous tubular vesicles represent B2's highest vesicularity fractions (40 – 70 vol.%), form extremely large leptokurtic curves, and bury all the rest of smaller vesicles into misleading flat distributions (Figs. 5 and 7). VCP's vesicles stand out for being $10^0$ – $10^5$ $\mu m^3$ coalesced, fibrous and complex, and forming irregularly connected 3D clusters (18 vol.%, Fig. 5).

From bottom to top Uig layers (Table 2), each pumice type's vesicle shape and size distributions change (Figs. 5 and 7). Overall, layers Uig1 to Uig3 comprise vesicular clasts of only VCP type, consisting of constant, unimodal, ± $10^3$ $\mu m^3$ vesicles, changing stratigraphically upwards from having spherical to tubular shapes within bimodal distributions. Layers Uig4 to Uig6 are characterized by typical bimodal and multimodal vesicle shape and size distributions due to most pumice types' vesicles, except GBP-B1's (up to $10^7$ $\mu m^3$), either increasing or decreasing between $10^4$ and $10^5$ $\mu m^3$ modes across layers, and spanning different vol.% of modal subspherical and spherical vesicles. All other vesicle shapes, mainly tubular and complex, are most typical in GBP-B2 and VCP. Layer Uig7 is characterized by ubiquitous unimodal, mesokurtic and leptokurtic, vesicle shape and size distributions, produced by the most frequent $10^3$ – $10^4$ $\mu m^3$ subspherical to spherical vesicles; the only exceptions being GBP-B2 (modal > $10^6$ $\mu m^3$ tubular) and VCP (modal complex vesicles). Layer Uig8 is well distinguished by bimodal and platykurtic vesicle shape and size distributions due to all vesicular clasts comprising plateauing $10^1$ to $10^4$ $\mu m^3$ spherical vesicles, combined with $10^6$ – $10^7$ $\mu m^3$ ellipsoidal, coalesced, tubular or complex vesicle shapes (Table 2).

### *4.3 Individual crystal metrics*

All pumices' crystal habits were classified in: 1) equant, from cubic to spherical (ShpF ≤ 1.5), 2) cuboid to subspherical (ShpF = 1.6 – 2.5), 3) plate-like tabular (ShpF = 2.6 – 3.5), 4) blade-like tabular (ShpF

= 3.6 – 7), 5) rod-like acicular (ShpF = 7.1 – 10), 6) thinly or spearing acicular (ShpF = 10.1 – 15), and 7) from radiating to indistinct aggregates (ShpF > 15) (Appendix B.1b). Crystal habits from equant to rod-like acicular were further classified in euhedral, subhedral, and anhedral textures using Ru differences. Crystal size was organized in the same manner as vesicles (Figs. 6 and 7). At any single layer, YWFP's crystals are mostly > $10^5$ μm$^3$, whilst the rest of pumice types' crystals range from $10^2$ to $10^6$ μm$^3$ (Fig. 7). Tabular crystals are obiquitus to all pumice types, but most frequent in YWFP (> 40 vol.%, Fig. 6). Likewise, YWFP stands out for having the highest fractions of euhedral crystals. Both YWCP and GCP contain similar fractions of equant (20 – 30 vol.%) and cuboid crystals (30 – 35 vol.%) of prevailing subhedral and anhedral textures; however, whereas the YWCP comprises more acicular (up to 30 vol.%) and $10^1$ – $10^2$ μm$^3$ crystals, the GCP has plenty of tabular (35 vol.%) and $10^2$ – $10^4$ μm$^3$ crystals (Figs. 6 and 7). Furthermore, the YWCP contains noticeable > $10^3$ μm$^3$ rod-like acicular crystals that, in lower fractions, also exist in the YWFP (Fig. 6). Both GBP-B1 and YWCP have most crystal textures in common, though B1 has higher cuboid crystal fractions (up to 50 vol.%, Fig. 6) comparable to those of the GCP. The GBP-B2 stands out for comprising mostly subhedral and euhedral < $10^4$ μm$^3$ cuboid (up to 80 vol.%), few > $10^3$ μm$^3$ rod-like acicular (10 vol.%), and > $10^5$ μm$^3$ tabular crystals (± 40 vol.%, Fig.6), similar to the YWFP. The VCP is the most contrasting pumice type due to comprising all subhedral to anhedral crystal habits, having the highest acicular crystal fractions (up to 40 vol.%), and containing both microlites and microphenocrysts forming aggregates of radiating habits (Figs. 3 and 6).

Except for YWFP's unimodal tabular crystals, which are constant from Uig4 to Uig8, all other pumice types' crystal habits and size vary from bottom to top stratigraphic layers (Table 2). Layers Uig1 to Uig3 are defined by VCP's mostly unimodal tabular to equant crystals, decreasing in modal size stratigraphically upwards from > $10^5$ to $10^3$ μm$^3$. Layers Uig4 to Uig6 are overall characterized by unimodal to bimodal crystal size distributions, fluctuating between $10^3$ and $10^6$ μm$^3$, and only slightly decreasing in size towards upper stratigraphic layers. Furthermore, in these same layers, crystal shape

modes progressively change from being unimodal tabular crystals-dominated to either becoming bimodal and multimodal or plateauing from tabular to cuboid and acicular crystal modes. Layer Uig7 is dominated by cuboid crystals (and most frequent secondary tabular shapes) and by crystals ranging from $10^3$ to $10^6$ $\mu m^3$ within bimodal to multimodal distributions. Strikingly, layer Uig7's VCP clasts are dominated by tabular crystals, alike YWFP, as well as radiating and shapeless aggregates. Layer Uig8 is characterized by bimodal, multimodal, and platykurtic shape and size distributions, produced by $10^2$ to $10^6$ $\mu m^3$ cuboid, tabular, and equant crystals (Table 2).

*4.4 Vesicle, crystal, and microlite number densities*

The *VNDs* span 3201 – 40397 individual vesicles ($V_N$) in most pumice types, and 211 – 871 $V_N$ in the GBP. The lowermost *VNDs* of < 2.5 *x* $10^5$ $mm^{-3}$ were identified in VCP clasts at Uig1 – Uig3 layers, and in GCP clasts at Uig8. The highest *VNDs* of > 1.5 *x* $10^6$ $mm^{-3}$ were estimated in YWCP and GBP-B1 clasts at Uig7 layer (Table 3). From bottom to topmost Uig layers, the YWCP, GCP and GBP-B1's *VNDs* increase from the lowest values at Uig4 layer to the highest values at Uig7. Likewise, YWFP, GBP-B2 and VCP's *VNDs* increase upwards in stratigraphy, but reach their highest values between layers Uig5 and Uig6. At Uig8, every pumice type's *VND* drops (Table 3). These same patterns repeated in Uig's weighted average *VNDs* (Table 4). In the latter case, two peaks of highest *VNDs* were clearly distinguished at layers Uig5-base and Uig7, followed by a drop at Uig8, within an overall positive yet fluctuating trend starting from the lowest *VNDs* at the bottommost Uig1 – Uig3 layers.

In most pumice types, the *CNDs* and *MNDs* represent 3320 – 132094 individual crystals ($C_N$) of which 2397 – 91795 are microlites ($M_N$), whilst in the GBP represent 61 – 1566 $C_N$ and 21 – 1448 $M_N$. The lowermost *CNDs* of < 1.5 *x* $10^5$ $mm^{-3}$ were estimated in YWFP clasts, and the lowest *MNDs* of < 2.0 *x* $10^5$, and as deprived as *x* $10^4$ $mm^{-3}$, were estimated in GBP-B2 and in YWFP clasts at most layers. The highest *CNDs* and *MNDs* of > 3.0 *x* $10^6$ $mm^{-3}$ were most frequent in YWCP clasts at Uig6 – Uig7 layers, and in VCP clasts at Uig1 – Uig4 layers (Table 3). In contrast with the *VND* data, which adjusts to general trends; from bottom to top Uig layers each pumice type's *CND* and *MND* data followed different

patterns. From Uig1 to Uig3 layers, the VCP clasts had some of the highest *CNDs* and *MNDs* before progressively dropping upwards in stratigraphy. At any layer, the GCP clasts remained constant, whilst all other pumice types' *CNDs* and *MNDs* increased slightly from Uig4 to Uig7 layers. At Uig8 layer, only the YWCP and GBP-B2's *CNDs* and *MNDs* dropped (Table 3). Using weighted average *MND* data (Table 4), three peaks of highest *MNDs* were recognized at Uig3, Uig6 and Uig8 layers, whereas the largest drop in *MND* was identified at layer Uig5-base.

### *4.5 Crystal and glass chemistry*

Chemical analyses of pumice types' crystals and groundmass glass were included in appendix C. YWFP's and GBP-B2's plagioclases are mostly euhedral crystals having weak normal zoning between anorthite and bytownite compositions (80 – 95 An%). All the rest of plagioclases are subhedral crystals that exhibit weak normal, reverse, and oscillatory zoning, and have compositions forming a nearly uninterrupted array from anorthite to andesine (35 – 95 An%; Fig. 3). Clinopyroxenes (cpx) are euhedral and subhedral crystals forming a tight trend from diopside to augite compositions (40 – 50 En%, 40 – 47.5 Wo%). However, in detail (Fig. 3), YWFP's and GBP-B2's cpx are only diopsides, some of which have the lowest MnO (0.4 – 0.8 wt.% MnO, 7.5 – 9.0 wt.% FeO tot); YWCP's and GBP-B1's cpx are both diopsides (0.6 – 0.8 wt.% MnO, 7 – 8.6 wt.% FeO tot) and augites (0.9 – 1.3 wt.% MnO, 7.3 – 8.6 wt.% FeO tot); and GCP's and VCP's cpx are mostly augites (0.8 – 1.2 wt.% MnO, 7.0 – 9.4 wt.% FeO tot) and rare diopsides, some of which have the highest FeO tot (0.5 – 0.8 wt.% MnO, 7.5 – 9.7 wt.% FeO tot). Amphiboles are generally subhedral crystals of contrasting Cr-actinolite (> 7.5 Si, Mg# = 50), and either Ti-rich or typical Mg-hastingsite compositions (< 6.5 Si, Mg# > 75, Na + K in A > 0.5). Strikingly, YWFP's and B2's amphiboles are only Mg-hastingsite, whilst the rest of pumice types' amphiboles span both chemical compositions (Fig. 3). The Fe-Ti oxides are mainly subhedral and anhedral crystals of titanomagnetite (± 0.8 mol.% ulvöspinel) and hematite, which have the same Ti contents (7.0 – 7.5 wt.% $TiO_2$) but varying major element compositions: YWFP's and B2's oxides have

tight ± 3.6 wt.% $Al_2O_3$ + MgO, whilst YWCP/B1's and GCP/VCP's oxides have, correspondingly, from 3.4 to 3.7 wt.%, and from 3.2 to 3.5 wt.% $Al_2O_3$ + MgO (Fig. 3).

The vast majority of groundmass glasses are rhyolite in chemical composition (Fig. 4), and can be classified in two types: 1) YWFP/YWCP, comprising low $SiO_2$ (71 – 72 wt.%) and high Fe-MgO oxides (1.5 – 2.5 wt.% FeO tot, 0.2 – 0.4 wt.% MgO); and 2) GCP, comprising high $SiO_2$ (72 – 75 wt.%) and low Fe-MgO oxides (1 – 1.5 wt.% FeO tot, 0.05 – 0.2 wt.% MgO). Most Uig rhyolite glasses match in composition with glasses from Taranaki's granitic xenoliths described in Gruender et al. (2010; Fig. 4). In contrast, two samples of YWCP glass have trachy-dacite (± 68 wt.% $SiO_2$) and basaltic trachy-andesite compositions (54 wt.% $SiO_2$), respectively. The dacite is overall similar to the rhyolites, comparable to glasses produced by other Taranaki's summit eruptives (e.g., Burrell eruption, Fig. 4), and similar to the granitic xenoliths' glasses. The basaltic trachy-andesite glass contains the lowest alkali (6 wt.%) and highest CaO (11 wt.%), which match with glass compositions produced by Fanthams Peak's eruptives (Fig. 4); however, it comprises the lowermost Fe-Mg oxides and Cl wt.%. GBP's and VCP's glass compositions were not included/analyzed due to limitations producing misleading results: GBP's comprising glasses matching both YWFP/YWCP and GCP compositions, and VCP's highest groundmass microcrystallinities unavoidably tainting glass.

*4.6 Geothermobarometry*

Eleven different glass + mineral assemblages were integrated, ranging from mafic (lowest-$SiO_2$ glass + most mafic minerals) to felsic compositions (highest-$SiO_2$ glass + most silicic minerals), for estimating pre-eruptive *P-T*, amphibole's $H_2O$ wt.%, and melt's $SiO_2$, $H_2O$ wt.% during crystallization (Table 5). The most mafic assemblage (YW1A_BA, Table 5) comprises YWCP's basaltic trachy-andesite glass + YWFP/YWCP's Ti-rich Mg-hastingsite + anorthite. This assemblage provided equilibrium *P-T* of 639 ± 81 MPa and 1100 ± 90 °C (Fig. 8) for a 57.6 ± 3 wt.% $SiO_2$ melt, saturated at 6 – 7 wt.% $H_2O$. A set of mafic to intermediate assemblages (YW1A – YW1C, YW2, YW3A, GP1 and GP3, Table 5) were formed with glasses ranging from YWCP's basaltic trachy-andesite and dacite to either YWFP/YWCP's

or GCP's lowest-$SiO_2$ rhyolites + Mg-hastingsite + bytownite and labradorite. These assemblages delivered equilibrium *P-T* ranging from 398 ± 30 to 517 ± 18 MPa, and from 932 ± 36 to 1039 ± 95 °C (Fig. 8), for 64 – 66 wt.% $SiO_2$ melts, saturated at 3 – 5 wt.% $H_2O$. The most felsic assemblages (YW3B_1, YW3B_2 and GP2, Table 5) comprise YWFP/YWCP's or GCP's highest-$SiO_2$ rhyolite glasses + actinolite + andesine. These assemblages provided low *P-T* ranging from 61 ± 2 to 83 ± 6 MPa, and from 706 ± 76 to 783 ± 42 °C (Fig. 8), for ± 78 wt.% $SiO_2$ melts containing minimum 2 wt.% $H_2O$ for actinolite crystallization. In all cases, the oxygen fugacity buffers yielded coherent values for $P >$ 100 MPa, yet only the hematite-magnetite buffer was consistent at $P \leq 100$ MPa.

Cpx-only thermobarometry was performed using seven groups of either YWFP/YWCP's or GCP's diopside and augite at reference *T* from 500 to 1500 °C in 100 °C steps. The cpx estimates provided equilibrium *P-T* of avg. 512 ± 37 MPa and 989 ± 9 °C for diopside, and avg. 521 ± 36 MPa and 1015 ± 11 °C for augite, which are consistent with the > 400 MPa equilibrium conditions resulting from amphibole thermobarometry. The cpx results were also consistent with the stability field of diopside + anorthite calculated via MELTS (Asimow and Ghiorso, 1998), and corrected with the $H_2O$-saturated experimental curves of Yoder (1965) and Burnham and Davis (1974) (Fig. 8). Similarly, the stability field of low-An% plagioclase (mostly andesine) was constrained using MELTS and the corresponding chemical data (Fig. 8). The resulting plagioclase liquidus curves are comparable with those of experimental albite (Burnham and Davis, 1974), and consistent with andesine being stable in the low *P-T* field provided by amphibole thermobarometry of the most felsic assemblages. Likewise, actinolite is also stable in the felsic low *P-T*, in agreement with experimental stability curves of Lledo and Jenkins (2008) and Mutch et al. (2016) (Fig. 8).

### *4.7 Magma decompression and ascent rates*

For *VND dP/dt*, *Dw* ranging from 1.6 x $10^{-12}$ to 3.8 x $10^{-11}$ $m^2$ $s^{-1}$ were calculated. For *MND dP/dt*, andesine (45 An%, 4 wt.% $H_2O$) and augite microlite compositions (± 3:7 ratio), increasing liquidus rates from 0.078 to 1.1 K $s^{-1}$, andesine $H_2O$-exsolution rates from 0.0009 to 0.027 wt.% $s^{-1}$, and augite

$H_2O$-exsolution rates from 0.0021 to 0.062 wt.% $s^{-1}$ were employed (Appendix B.2). Heterogeneous surface tension-based *VND dP/dt* were preferred due to providing the most consistent results relative to experimental data (Colombier et al., 2017; Shea, 2017; Hajimirza et al., 2021; Fig. 9 b); 2 wt.% $H_2O$ – *VND dP/dt* were chosen for representing most pumice types (minimum for actinolite crystallization), and min. 3 wt.% $H_2O$ – *VND dP/dt* were selected for representing the YWFP and the GBP-B2 due to their lowermost microcrystallinities (e.g., Shea, 2017). Homogeneous surface tension-based *VND dP/dt* were only calculated for reference of maximum possible values (e.g., Shea, 2017). The *MND dP/dt* were employed for constraining the effects of decompression on late-stage crystallization (e.g., Blundy et al., 2006; Toramaru et al., 2008).

From all pumice types, YWFP's and GBP-B2's *VND dP/dt* > 7.5 MPa $s^{-1}$, and YWCP's *MND dP/dt* > 2.0 MPa $s^{-1}$ were the fastest, and GCP's rates of < 1.0 (*VND*) and < 0.2 MPa $s^{-1}$ (*MND*) were the slowest (Table 3). From bottom to top Uig layers, most pumice types' *VND dP/dt* increase consistently yet at different paces from layer Uig1 to Uig5, subsequently drop, and finally upsurge back at layer Uig7 before last declining at Uig8 to a higher or lower intensity (Fig. 9 a). Strikingly, GBP-B2's *VND dP/dt* estimates are the exception for also peaking at layers Uig4 and Uig6 (Fig. 9 a). These results were consistent with Uig's wt. avg. *VND dP/dt* data (Table 4) that follow a rapid one-order of magnitude upsurge in rates passing from layer Uig3 to Uig4 – Uig5, a second peak at Uig7, and a general decreasing rate at layer Uig8 (Fig. 9 b-c). For the *MND dP/dt* data, most pumice types reached the fastest rates at layer Uig7 (Fig. 9 a) within a general positive trend. The only exceptions were GCP's and GBP-B1's rates, which also peaked at Uig5 and Uig8, respectively; and VCP's rates that, in contrast with the rest of pumice types, were the fastest at Uig3, and thenceforth slowed down upwards gradually (Table 3, Fig. 9 a). Similarly, Uig's wt. avg. *MND dP/dt* data (Table 4) follow a general positive trend that, however, peaks to one-order of magnitude higher at layer Uig6, and subsequently drops and remains constant from Uig7 to Uig8.

Minimum wt. avg. magma ascent rates (*U*, Table 4) (e.g., Cassidy et al., 2018) range from slow 0.01 – 0.02 m $s^{-1}$ at bottommost layers Uig1 – Uig3, through to intermediate 0.06 – 0.1 m $s^{-1}$ at layers Uig5-top, Uig6 and Uig8; to peak 0.15 – 0.3 m $s^{-1}$ velocities at layers Uig4 – Uig5-base and Uig7 (Fig. 9 d). Maximum wt. avg. *U* repeat the same categories at equal layers, but rates are three-orders of magnitude higher, ranging from slow 17 – 25 m $s^{-1}$ up to supersonic 400 – 625 m $s^{-1}$, considering vesiculated magmas having wt. avg. $\rho_{bulk}$; and from slow 13 – 23 m $s^{-1}$ to rapid 150 – 200 m $s^{-1}$, assuming saturated magmas (2500 kg $m^{-3}$ $\rho_{solid}$). Conversely, wt. avg. *U* calculated from *MND dP/dt* (e.g., Toramaru et al., 2008) match with maximum wt. avg. 24.3 ± 0.5 m $s^{-1}$ slow velocities (Uig1 – Uig3), but thenceforth fluctuate between 50 and 90 m $s^{-1}$, and reach the fastest 158 m $s^{-1}$ at Uig6 only.

## 5. Discussion

### *5.1 Interpretation of textural types and chemistry*

From pyroclast macro and 2D and 3D microtextures, and mineral and glass chemistry, we have classified all pumice types in highly crystalline, crystalline-vesicular, and highly vesicular (Appendix B.1d); and inferred a variety of magmas that were involved in the onset of Uig's multiple eruptive phases. The highly crystalline VCP, which is the single vesicular component of layers Uig1 – Uig3 but exists in almost all layers, encompasses the highest crystallinities, identical phenocryst assemblages than the rest of pumice types, and the richest contents of andesine, actinolite, and oxide microphenocrysts and microlites. From these evidences, we interpret that: a) although at first-hand VCP clasts appear to be accidental, reheated, or picked-up material from older eruptions; VCP's vol.% changes across layers (Fig. 2) stand for a component that actively influenced Uig's eruption dynamics; b) the VCP magma was the first being erupted in the Uig after a period of cooling and crystallization inside conduit's topmost water-rich levels (for amphibole crystallization; e.g., Mutch et al., 2016); c) the VCP magma was the most differentiated in terms of mineralogy, comparable to the GCP; d) the VCP magma remained in the conduit since last pre-Uig eruptives, and was associated with the OD-AL lavas that shaped the pre-3300 cal BP summit dome of Taranaki (Torres-Orozco et al., 2017b; 2018); e) dome-collapse was probably

produced due to building up internal pressures of both the VCP and the rest of magmas involved in subsequent Uig phases; and it unroofed and opened the conduit, tapering the VCP magma immediately, and producing the first Uig explosive events (e.g., Thivet et al., 2020); and f) the VCP magma was probably either in contact or associated with the GCP magma.

The crystalline-vesicular YWCP, GBP-B1 and GCP have similar phenocryst assemblages but different glass, microphenocryst and microlite compositions. YWCP comprises the least silicic glass, all plagioclase, amphibole and clinopyroxene compositions, and the highest wt.% major element oxides. GCP includes the most silicic glass, all plagioclases except anorthite, all amphiboles but Ti-rich Mg-hastingsite, mainly augites, and the lowest wt.% major element oxides. Strikingly, GBP-B1 contains groundmass glass of the two silica compositions, and its crystal and vesicle shape and size distributions at every Uig layer fit with a combination of YWCP's + GCP's distributions (Figs. 5, 6 and 7). Mass-balancing the three pumices using their *CNDs*, crystal fractions, and *MNDs*, demonstrated that the GBP-B1 is primarily made of YWCP + less GCP (Fig. 9 a). As the eruption progressed from Uig4 to Uig5-top, the Uig passed from erupting GBP only (B1 and B2), through to producing GCP and GBP, to finally ejecting all three pumices simultaneously. Furthermore, whilst YWCP was GBP-B1's principal constituent in most layers, at Uig7 both YWCP and GCP formed equal GBP-B1's fractions (Fig. 9 a). These evidences suggest that: a) the GCP magma was the most differentiated, similar to the VCP; and the YWCP magma was the least evolved of all magmas associated with crystalline-vesicular pumice types; b) mixing and/or mingling to different extents of YWCP and GCP produced the GBP-B1; c) further magma interactions happened due to GBP-B1 and -B2 forming pervasive pyroclasts, and GBP-B1's vesicle distributions proving influence from YWFP; d) at Uig4, the eruption only discharged the GBP blend, suggesting that magma was generated and tapered from the hot contact between YWCP and GCP; e) more balanced YWCP + GCP magma mixing started at Uig7-base (ca. 26:24 %, Fig. 9 a) probably due to continued heating and more efficient GCP melt generation; f) we therefore infer that both YWCP and GCP magmas were initially differentiated inside a common storage level; g) assuming

a heat-pipes system (Marsh, 2015), the GCP cooled and partially crystallized, forming outer reservoir and conduit walls that wrapped hot YWCP magma inside; and h) both magmas pre- and syn-eruptively mixed, producing the GBP-B1, but were also tapered separately.

The highly vesicular YWFP and GBP-B2 have the lowermost crystallinities at any given layer, and glass wt.% silica comparable to that of the YWCP but overall higher wt.% major elements. Phenocrysts assemblages are consistent with the rest of pumice types; however, the microphenocrysts and scarce microlites comprise only bytownites and anorthites, diopsides, and the highest fractions of Ti-rich Mg-hastingsite. Strikingly, no actinolite crystals were identified. Close inspection into vesicle and crystal distributions, plus mass-balancing the corresponding *CNDs*, crystal fractions, and *MNDs* (Fig. 9 a), revealed that the GBP-B2 matched with the YWFP at all layers. From these evidences, we interpret that: a) both YWFP and GBP-B2 were formed from the same magma; b) mixing/mingling of crystalline-vesicular and highly vesicular magmas produced GBP pyroclasts, whose B1 and B2 bands mutually influenced each other's texture and composition (e.g., Paredes-Mariño et al., 2017); c) the YWFP/B2 magma, having the most mafic mineral assemblages, was the least differentiated of all Uig magmas; d) we deduce that, before the Uig, hot YWFP/B2 magmas fed YWCP/GCP's shallow heat-pipes magma reservoirs, so that shallow crystallization of YWFP/B2 produced the YWCP magma; e) eventual rapid YWFP/B2 magma decompression forced not only YWCP/GCP's reservoir/conduit failure, but also shear-deformation between contrastingly viscous magmas, yielding to syn-eruption of both GBP and YWFP at Uig4 (e.g., Papale, 1999; Gardner, 2007; Palladino et al., 2008); and f) subsequent intermittent tapering of separate YWFP, YWCP, GCP and GBP was likely produced by unsteady decompression rates.

### *5.2 Pre-eruptive magmatic processes*

Based on the chemical, geothermobarometric and textural data, we have concluded that: a) the Uig marks the start of a new cycle of mafic magma recharge inside a multi-feeder, dikes plumbing system below Taranaki, in agreement with similar conclusions for other Taranaki eruptives made by Turner et al.

(2008; 2011), Zernack et al. (2012) and Damaschke et al. (2017); b) post-Uig volcanism at Fanthams Peak vent directly tapered the deeper, recharged, and less differentiated mafic magma (Torres-Orozco et al., 2017a; 2017b); and c) before erupting, the Uig magmas were differentiated via fractional crystallization, melting and assimilation of the plutonic crust (e.g., Price et al., 2005), while residing and/or ascending inside a heat-pipes network, across at least four (1 – 4) different *P-T* conditions (Fig. 10 a). (1) At ca. 17 km-depth, 1100 °C mafic magmas accumulated within the lower crust and partially crystallized. Fractional crystallization of pyroxene ± olivine is consistent with mafic xenoliths described in Gruender et al. (2010), and could explain the genesis of anorthite ± Ti-rich Mg-hastingsite-bearing basaltic-andesite magmas (BA) having compositions similar to YWCP's BA glass and post-Uig Fanthams Peak eruptives (Fig. 4). (2) At 11 – 14 km-depth, 950 – 1000 °C BA melts reached neutral buoyancy at the base of the plutonic/metamorphic upper crust. In these conditions, instability of Ti-rich Mg-hastingsite produced mineral assemblages consisting of anorthite/bytownite ± diopside ± Mg-hastingsite ± titanomagnetite. Besides partially crystallizing, the BA magmas mixed and/or assimilated, to different extents, with high-Si melts from partial melting of the plutonic upper crust (e.g., Price et al., 1999; 2005; Zernack et al., 2012), producing a suite of BA, dacite, and rhyolite melts transporting mafic crystals (Fig. 4). Further BA magma inputs, along with fractional crystallization and assimilation, supported increasing melt volumes, volatile saturation, and exsolution inside magma storage driving subsequent magma ascent through upper crust's dikes system (e.g., Sherburn and White, 2006; Turner et al., 2008; 2011; Zernack et al., 2012). (3) At 5 – 6 km-depth, > 900 °C rhyolite melts reached neutral buoyancy on top of the plutonic crust due to reduced lithostatic pressures exerted by Tertiary Taranaki Basin's low-density sedimentary deposits forming the topmost part of the upper crust (Sherburn et al., 2006; Fig. 10 a). Although most crystals being transported in the rhyolite indicate deeper *P-T*, the few feldspars and oxide microlites, and mainly the absence of actinolite crystals (stable in the plutonic crust), support short-lived storage of hot rhyolite at ± 150 MPa (Fig. 8 c). Subsequent magma ascent was controlled by interplaying, locally active, trans-tensional and compressional tectonics (e.g., Sherburn

and White, 2006; Sherburn et al., 2006; Stagpoole and Nicol, 2008). (4) At ca. 2 – 3 km-depth, 700 – 800 °C rhyolite melts were stored and crystallized variable fractions of labradorite/andesine ± augite ± actinolite ± oxide microphenocrysts and microlites before eruption.

*5.3 Magma decompression dynamics*

From the calculated *VND dP/dt* and *MND dP/dt*, we have identified three distinct magma decompression regimes driving magma ascent and eruption during the Uig: 1) stepwise, 2) rapid and 3) intermittent (Fig. 9 c). The (1) stepwise regime was characterized by tapering and eruption of the shallowest VCP magma at relatively constant 0.3 – 0.5 MPa $s^{-1}$, producing the first Uig explosive events of conduit unroofing that formed layers Uig1 – Uig3 (Fig. 9 a). The (2) rapid decompression regime tapered the deepest and highly vesicular YWFP/B2 magmas at ± 10 MPa $s^{-1}$, and contrasting shallow and crystalline VCP, GCP and GBP-B1 magmas at 0.5 – 1 MPa $s^{-1}$ (Fig. 9 a). This regime defined Uig's most abrupt avg. *dP/dt* shift from 0.5 to 6 MPa $s^{-1}$ (Fig. 9 c), and triggered some of the most explosive eruptive events that generated layer Uig4, and the first AIL clasts-bearing layer Uig5-base (e.g., Gardner, 2007). It is noteworthy that the *MND dP/dt* data span lower rates of 0.2 – 0.3 MPa $s^{-1}$ (Fig. 9 a), highlighting the major influence that YWFP/B2's high vesicularities associated with magma decompression had in controlling the rapid regime. The (3) intermittent regime was marked by tapering of the crystalline-vesicular YWCP magma at constant 1 – 2 MPa $s^{-1}$, along with the rest of magmas at fluctuating *dP/dt* between 0.5 and 10 MPa $s^{-1}$ (Fig. 9 a). On average, the intermittent dynamics consisted of a quick drop in *dP/dt*, relative to previous events, producing the AIL clasts-bearing layers Uig5-top and Uig6; a renewed upsurge in *dP/dt* up to the fastest rates in the climactic Uig7; and declining *dP/dt* during the eruption ending and forming layer Uig8 (Fig. 9 c). Strikingly, the YWCP at all layers, and VCP from Uig1 to Uig4, had equivalent *VND dP/dt* and *MND dP/dt* (Fig. 9 a) that suggest parallel syn-eruptive effects of decompression on the kinetics of both bubbles and microlites (e.g., Cashman and Blundy, 2000; Blundy et al., 2006; Gardner, 2007).

*5.4 Magma ascent rates*

The quantification of minimum and maximum wt. avg. *U* (Fig. 9 d) comprised limitations equivalent to those of *dP/dt* estimates, depending on whether *U* derived from bubble or microlite metrics, and on initial *P-T* conditions. Thereafter, we infer that: a) min. wt. avg. *U* are the closest to real mean velocities of all ascending magmas, especially those rising from 5 – 6 km-depth (e.g., Burgisser and Degruyter, 2015; Cassidy et al., 2018; Lormand et al., 2020); and were hence preferred in comparing different eruptive phases (Fig. 9 d). b) Wt. avg. *U* calculated from *MND dP/dt*, and max. wt. avg. *U* for saturated magmas calculated from *VND dP/dt,* best represent velocities of magmas at ± 2 km-depth, where volatile diffusion and exsolution rates played major roles in vesiculation and in microlite crystallization kinetics (e.g., Shea, 2017; Lormand et al., 2020). c) Supersonic max. wt. avg. *U* for vesiculated magmas possibly represent vent-exit velocities produced during final extreme exsolution and vesiculation kinetics before fragmentation, and magma acceleration characteristic of Plinian eruptions (Taddeucci et al., 2012; Burgisser and Degruyter, 2015). Henceforth, we estimated reasonable that, in most magma's transport within the volcanic conduit, slow 0.01 – 0.02 m $s^{-1}$ *U* produced conduit unroofing explosions driven by stepwise *dP/dt* (Uig1 – Uig3), similar to lava dome eruptions ranging in intensity from, e.g., AD 1991-95 Unzen to AD 1902 Peleé (Fig. 9 c – d); intermediate 0.06 – 0.1 m $s^{-1}$ *U* triggered further pre-climactic and post-climactic explosive phases during intermittent *dP/dt* (Uig5-top, Uig6, Uig8), similar in intensity to the most explosive eruptive phases from, e.g., AD 1912 Novarupta (Fig. 9 c – d); and rapid 0.15 – 0.3 m $s^{-1}$ *U* were reached during the most explosive pre-climactic and climactic eruptive phases driven by both intermittent and rapid *dP/dt* regimes (Uig4, Uig5-base, Uig7), comparable to climactic explosive eruptions from, e.g., AD 79 Vesuvius, AD 1875 Askja, and AD 1980 Mt. St. Helens (Fig. 9 c – d). Close to fragmentation levels or at vent-exit, magmas accelerated to either 15 – 25 m $s^{-1}$, 50 – 200 m $s^{-1}$, or up to supersonic 400 – 600 m $s^{-1}$, depending on the respective eruptive phase.

### *5.5 Magma degassing and crystallization dynamics*

We have identified a series of magma degassing and crystallization processes taking place before and during the Uig (Figs. 5 to 9), using the interpretations of pumice types and magmas, vesicle and crystal

distributions, number densities and *dP/dt* data (e.g., Gurioli et al., 2005; 2008; Shea et al., 2010; Pardo et al., 2014; Rotella et al., 2014; Colombier et al., 2017; Heinrich et al., 2020; Arzilli et al., 2019; 2022). From the vesicles data, the VCP magma comprised an initial stage of bubble nucleation and prevailing equant growth from Uig1 to Uig3 (Figs. 5 and 7), driven by stepwise *dP/dt* and rapid exsolution kinetics due to shallowest storage (Fig. 9 a), generating Uig's first vent unroofing explosive eruptions. This first stage of vesiculation peaked at Uig4, in which VCP magma foams comprising bubbles of constant $10^3$ – $10^4$ $\mu m^3$ volumes yet heterogeneous spherical, coalesced, tubular, and complex shapes developed. Subsequently, all magmas followed near parallel vesiculation trends consisting of accelerated bubble nucleation and growth from Uig4 to Uig6 (Fig. 7), generating Uig's most explosive pre-climactic eruptive phase. Within this eruption timeframe, all magmas experienced at least one out of three separate stages of vesiculation driven by *dP/dt* changing from rapid to intermittent (Fig. 9 a), spanning $10^2$ – $10^4$ $\mu m^3$ freshly nucleating and equant growing bubbles, ± $10^5$ $\mu m^3$ prevailing ripening subspherical bubbles, and up to $10^6$ – $10^7$ $\mu m^3$ further ripening and coalescing elongated bubbles (Figs. 5 and 7). These coexisting vesiculation waves produced rheologically heterogeneous magma foams that supported explosions of fluctuating intensities at intermittent *dP/dt* from Uig5-base to Uig5-top (e.g., Shea et al., 2010; 2011). Further accelerated nucleation and subspherical growth of the freshest third stage bubbles in the YWCP and GBP magmas, along with ceasing tapering of YWFP, GCP and VCP magmas, and gradually upsurging *dP/dt*, drove the explosive activity that produced layer Uig6. A fourth and most intense vesiculation stage took over all magmas' bubble distributions at Uig7, producing apparent single vesiculation stage distribution curves (Fig. 7), and developing the most homogeneous magma foams consisting of near exclusive $10^3$ – $10^4$ $\mu m^3$ subspherical and highly spherical bubbles (Figs. 5 and 7). These rheologically uniform magma foams were steadily decompressed at rapid *dP/dt*, producing Uig7's Plinian eruption column (Fig. 9 a – c) (e.g., Gardner et al., 1996; Gurioli et al., 2005; Shea, 2017). Following the latter climactic phase, fast bubble coalescence and efficient outgassing from all magmas,

along with decelerating *dP/dt*, induced bubble collapse and rapid magma densification at Uig8 (Figs. 5 and 7), producing eruption column instability, partial collapse, and gradual eruption ending.

In addition, the VCP and YWFP/B2 magmas experienced complimentary bubble deformation processes (e.g., Okumura et al., 2006; Giachetti et al., 2019); that produced: 1) VCP's complex bubbles consisting of either few small bubbles attached to a single larger bubble, or manifold coalesced bubbles forming clusters, all of which formed 3D networks of spindly bubbles apparently squeezed in between crystals (Fig. 5); and 2) GBP-B2's pervasive fibrous-tubular bubbles (Fig. 7) having maximum sizes at Uig4, Uig5-base and Uig7.

From the crystals data, the VCP magma consisted mostly of $10^5$ – $10^6$ μm$^3$ tabular and less $10^2$ – $10^4$ μm$^3$ cuboid crystals at Uig1 – Uig2 (Figs. 6 and 7), either transported from deep levels and formed during old crystallization stages, or produced from undercooling before eruption (e.g., Cashman and Blundy, 2000; Toramaru et al., 2008). Subsequent nucleation and growth of $10^3$ – $10^4$ μm$^3$ equant oxide crystals quickly developed at Uig3 syn-eruptively (interpreted from Uig's eruptive dynamics), and completely modified VCP's crystal distributions. Strikingly, these oxide microphenocrysts' volumes implicated extremely fast rates of syn-eruptive crystal growth (e.g., Arzilli et al., 2019; 2022), which evolved during Uig's most abrupt *dP/dt* shift from stepwise to rapid (Fig. 9 a). VCP's oldest tabular crystals match with the rest of magmas' largest tabular crystals. From Uig4 to Uig6, the crystalline-vesicular magmas mainly consisted of acicular and tabular microphenocrysts and phenocrysts transported from deep levels, and formed in a single old crystallization stage. Overall, GCP's old crystals grew up to volumes of ± $10^6$ μm$^3$, larger than YWCP's modal $10^4$ – $10^5$ μm$^3$ old crystals (Figs. 6 and 7), suggesting GCP's lengthier cooling periods. Likewise, YWFP/B2 magma's $10^5$ – $10^6$ μm$^3$ tabular and scarce acicular crystals were formed in a single old crystallization stage and were transported from deep levels. However, whereas YWFP/B2 magma's old crystals were near entirely constant in habit and volume during the complete Uig (Figs. 6 and 7), and the YWFP/B2 magma underwent shallow crystallization of only few ± equant oxides recorded since deposition of layer Uig5-base (Appendix

B.1d); the rest of magmas experienced more intense crystallization processes. From Uig3 to Uig5-top, VCP's crystals gradually clustered into growing aggregates accompanying the remaining separate crystals. In addition, from Uig7 to Uig8, a third stage of rapid decompression-induced crystallization (e.g., Blundy et al., 2006) further produced new $10^2 – 10^3$ μm$^3$ equant and few tabular crystals, some of which continued assembling aggregates until the end of the Uig. VCP's third crystallization stage overlapped with the crystalline-vesicular magmas' second stage of accelerated nucleation and growth of $10^1 – 10^4$ μm$^3$ cuboid and few tabular crystals. The crystalline-vesicular magmas' second crystallization wave started at Uig4, driven by rapid *dP/dt* initially; and crystals produced in this second stage reached their maximum numbers and volumes during eruption of the climactic Uig7 Plinian column, after prolonged intermittent crystallization induced by either decompression or stalling affected all magmas from Uig5 to Uig7 (Fig. 9 a, and appendix B.1d) (e.g., Arzilli et al., 2019; 2022). These latest crystallization processes continued until the end of the eruption, and completely modified the crystalline-vesicular magmas' crystal distributions at Uig7 – Uig8.

Based on YWFP's chemistry and individual crystal metrics being exceptionally unchanged along the duration of the Uig, we conclude that all magmas' vast majority of > $10^4$ μm$^3$ old tabular microphenocrysts and phenocrysts are plagioclase and clinopyroxene, most > $10^5$ μm$^3$ old acicular crystals correspond to plagioclase and amphibole, and most < $10^4$ μm$^3$ late-stage plate-/blade-like tabular, acicular, and equant crystals correspond to plagioclase, clinopyroxene/amphibole, and Fe-Ti oxides, respectively.

### *5.6 Bubble – Crystal interactions*

Following Uig's magma degassing and crystallization processes, we recognized a set of mutually influential bubble – crystal interactions that powered Uig's eruption dynamics:

a) VCP's complex bubbles and radiating crystal aggregates were controlled by (1) limited space for bubble and crystal growth at high crystallinities, (2) further new microlites nucleating, and (3) crystal

aggregates themselves that confined and forced bubbles to coalesce and deform gradually within the eruption time (e.g., Taddeucci et al., 2021).

b) All magmas except YWFP/B2 experienced pre-eruptive microphenocryst and microlite crystallization while cooling inside shallow and water-rich storage levels for actinolite crystallization (e.g., Mutch et al., 2016). By these means, YWCP's initial *CND* and *MND* are those of GBP-B1 from Uig4 to Uig5-top (Fig. 9 a, and appendix B.1d), and any subsequent gains in crystal cargo were induced by magma decompression (e.g., Blundy et al., 2006). However, whereas the effects of decompression-crystallization affected mostly the YWCP magma in the last half of the Uig, GCP's crystallinities remained largely constant.

c) Of all magmas, the effects of decompression-induced degassing were most significant in the YWCP due to high *CND* and *MND* (e.g., high numbers of Ti-magnetite) providing free-energy sites for extensive heterogeneous bubble nucleation (e.g., Gardner, 2007; Colombier et al., 2017; Pleše et al., 2019), while at the same time impeding bubbles from coalescing owing to the consistent and gradually scaling, viscous, inter-pore, microlite-rich fine groundmass (Pleše et al., 2018; 2019). This evolving rheology yielded to the highest *VNDs* in the climactic Uig7 eruptive phase (Fig. 9 a). Indeed, YWCP's near identical *VND dP/dt* and *MND dP/dt* further suggest heterogeneous bubble nucleation and decompression-induced microlite crystallization acted concurrently.

d) In contrast with the rest of magmas, YWFP/B2's characteristic equant bubble shapes and smooth walls are consistent with poor microcrystallinities and lowermost *CND* and *MND*, and support quasi-homogeneous bubble nucleation from melt and on old crystals, growth limited by melt viscosity almost alone, and bubble coalescence reducing *VNDs* following the most explosive pre-climactic Uig4 – Uig5 and climactic Uig7 eruptive phases (Fig. 9 a) (e.g., Gardner, 2007; Namiki and Manga, 2008).

e) Overall poor microcrystallinities, scarce microlite contents, and absence of actinolite crystals despite the inferred ± constant wt.% $H_2O$ (Table 5), suggest that the YWFP/B2 magma was hot enough to

avoid crystallization from cooling, and that it was tapered from crust levels deeper than the rest of magmas, consistent with ± 150 MPa necessary to avoid actinolite crystallization (Fig. 8). Also, magma storage was likely brief, and magma ascent was near uninterrupted and rapid enough to prevent any significant shallow crystallization (e.g., Arzilli et al., 2019; 2022).

f) Furthermore, YWFP/B2's distinctive high and maximum *VNDs*, existing since the beginning of the most explosive pre-climactic and the climactic eruptive phases, suggest that bubble nucleation and growth were delayed up to shallow conduit levels, so that growth by coalescence and outgassing were avoided despite YWFP/B2's relatively low viscosity and ascent from deepest 5 – 6 km. Delayed vesiculation kinetics in silicic melts is consistent with magma supersaturation due to rapid *dP/dt* from deep levels, and with subsequent intense volatile diffusion and exsolution at shallow depths further powering accelerated magma ascent (e.g., Mangan and Sisson, 2000).

g) From GBP-B2's crystal shape and size distributions' having prominent GBP-B1 modes and vice versa, it is clear that the YWCP, GCP and YWFP/B2 magmas mingled and produced the GBP (Figs. 6 – 7, and appendix B.1c). Moreover, GBP-B2's fibrous tubular bubbles were produced by exsolution during deformation due to shearing between hot magma bubbles and more viscous and crystalline GBP-B1 magmas at the fastest *dP/dt* (e.g., Okumura et al., 2006). This process enabled preserving bubbles of original YWFP sizes and shapes that were not directly in contact with the GBP-B1 magma, and further support delayed YWFP/B2's vesiculation at least up to shallow YWCP/GCP magma storage levels.

h) Conversely, GBP-B1 magma was produced from mixing at different degrees between YWCP and GCP magmas (Fig. 9 a). Nonetheless, at the onset of the Uig, the YWCP melt was hotter and more voluminous than the GCP, and mostly picked up GCP's crystals without efficiently mixing with GCP's melt. This process resulted in separated tapering of YWCP and GCP, and in B1's crystals recording contributions from each member, whilst B1's bubbles mirroring YWCP's bubble metrics for most part of the Uig (Figs. 5 and 7). Outstandingly, later in the eruption, prolonged heating and

late-stage profuse GCP melting supported GBP-B1 magma's syn-eruptive differentiation from YWCP and GCP via further decompression-crystallization at Uig8 (Fig. 9 a) (e.g., Blundy et al., 2006).

i) Strikingly, Uig's two most explosive eruptive phases: pre-climactic Uig4 – Uig5 and climactic Uig7, were driven by the rapidest *dP/dt* of Uig's rheologically most homogeneous magmas (e.g., Shea et al., 2011; 2017). These magmas were produced at bubbles reaching the highest *VNDs* and constant modal volumes of $10^3$ – $10^4$ μm$^3$, and at crystals comprising maximum *CNDs* and *MNDs*, ranging mostly from $10^2$ to $10^4$ μm$^3$ (i.e., microlites and the smallest microphenocrysts), and having prevailing modal equant and cuboid habits. However, whereas the Uig4 – Uig5 magmas comprised heterogeneous bubble shapes, including plenty of deformed VCP and GBP bubbles, the Uig7 magmas contained near exclusive spherical to subspherical bubbles. We thus interpret that the processes driving these differences in bubble shape (e.g., Okumura et al., 2006; Wright and Weinberg, 2009; Giachetti et al., 2019) could have induced contrasting pre-climactic and climactic intensities.

*5.7 Conduit radius and mass discharge rates*

The climactic Plinian column that formed layer Uig7 was erupted at 7.6 *x* $10^7$ kg s$^{-1}$ (Torres-Orozco et al., 2017b) from a conduit of avg. 10.5 ± 0.05 m-radius (Fig. 9 c, d). Subsequent magma outgassing and further conduit widening to 12 m-radius (Fig. 9 d), consistent with magma densification (Fig. 9 a), produced overall declining eruption intensities represented by slight decreasing *dP/dt* and *MDR* (6 x $10^7$ kg s$^{-1}$), driving column collapse and generating gravity-driven PDCs that formed the AJ- and ALT-rich layer Uig8. According with compositions, textures, densities and vol.% of Uig's dense clasts, as well as with Uig's eruption styles and corresponding deposit distributions (Torres-Orozco et al., 2017b), the Uig7 conduit was established since the onset of a series of highly explosive pre-climactic events (e.g., Carazzo et al., 2012; Cronin et al., 2013; Maeno et al., 2019). These events: a) widened from ca. 5.5 to 9.1 – 10.5 m-radius, and deep-down excavated the conduit, producing the unique AIL-bearing Uig5 – Uig6 deposits (Fig. 2), consistent with Uig4 – Uig5's fastest *dP/dt* and ascent rates (Fig. 9 c, d); b)

erupted at *MDRs* fluctuating between min. 4.1 x $10^7$ and up to 9.3 x $10^7$ kg $s^{-1}$ (Fig. 9 c); and c) produced a series of PDCs of varying intensity that formed layers Uig4 – Uig6. Before these pre-climactic events, the conduit was unroofed and opened to avg. 3.7 ± 0.07 m-radius by moderate explosive eruptions scaling from 1.1 x $10^6$ to 4.1 x $10^6$ kg $s^{-1}$ (Fig. 9 c, d). These unroofing explosions gradually destroyed the summit dome and produced BAF pulses, forming the AJ, OD-AL, and VCP-rich layers Uig1 – Uig3, similar to the eruptive activity of other lava-dome forming andesitic volcanoes (Fig. 9 d) (e.g., de' Michieli Vitturi et al., 2008; Capra et al., 2016; Thivet et. al., 2020).

*5.8 Magma fragmentation and eruption styles*

Using all previous data plus relative calculations of magma buoyancy, viscosity, and strain rates (e.g., Papale, 1999; Mader, 1998; Gonnermann and Manga, 2013; Cassidy et al., 2018), we have inferred the mechanisms of magma fragmentation, divided into five general stages (1) to (5), controlling eruption styles and intensities during every Uig eruptive phase (Fig. 10 b, c).

1) In Uig's vent-unroofing and conduit-opening phase (1), the shallowest, least buoyant and vesicular, but most crystalline VCP magmas were tapered at Uig's slowest *dP/dt*, ascent, and strain rates; driving the slowest *MDR*s from conduits reaching the narrowest diameters (Fig. 10 d - e). In addition, VCP's *VNDs* were also the lowest, but still as high as in, e.g., AD 2008 Chaitén (Fig. 9 b), and provided evidence of syn-eruptive bubble nucleation complementing slightly increasing *MNDs*. From these evidences, we interpret that fragmentation of the VCP magma was mostly controlled by rapid volatile diffusion and exsolution inside fractures below Taranaki's summit dome and in evolving shallow narrow conduits, yielding into melt's passing glass transition due to higher viscosities, along with increasing magma volumes and internal pressure enough for breaking VCP magma's brittle strength (Alidibirov, 1994; Gonnermann, 2015; Cassidy et al., 2018). This is consistent with VCP magma's shallowest storage at water-rich levels indicated by actinolite. During the Uig, VCP's rapid volatile exsolution kinetics could have been triggered by heating from all: microlite crystallization's latent heat, strain localization produced by friction in local faulting/fracturing, and heat-transfer and stress

induced by decompression of the rest of deeper Uig magmas (Blundy et al., 2006; Gonnermann 2015; Lavallée et al., 2015). In fact, rapid exsolution induced by heating is consistent with VCP's complex 3D-spindly bubble shapes developing later in the Uig (Fig. 5), similar to textures observed in Santiaguito volcano (Lavallée et al., 2015), demonstrating scaling internal stress due to difficulties for gas expansion and melt flow within VCP's crystallinities. It is noteworthy that, due to limited magma supply, VCP magma's fragmentation powered relatively low to moderate and transient explosive eruptions only, inducing mostly gravity-driven stepwise summit dome-collapses in Taranaki, and forming successive Uig1 – Uig3 BAF pulses (Fig. 10 c) whose deposits contained only < 5 vol.% VCP (max. 20 vol.%; Figs. 1, 2), somewhat intermediate between, e.g., PDC eruptions of June 10 and 11, 2015, of Colima volcano (Capra et al., 2016). In any case, these types of Taranaki dome-collapse eruptions were able to transform the summit vent area's morphology (e.g., de' Michieli Vitturi et al., 2008), gradually develop initial narrow upper volcanic conduits, and reach intensities and style similar to the eruptions of AD 1902 Pelée and AD 1991-1995 Unzen (Fig. 9 c, d).

2) Uig's pre-climactic explosive phase comprised two halves (2 and 3) in which the Uig passed from reaching the highest intensities to shifting into moderate explosivity. In the first half (2), represented by layers Uig4 – Uig5-base, all magmas except the YWCP were tapered, including slug fractions of the deepest, least crystalline but most buoyant and vesicular YWFP/B2 magma rising at the rapidest *dP/dt*, ascent, and strain rates; producing the fastest *MDR*s from conduits that duplicated their diameters abruptly passing from Uig3 to Uig4 events (Fig. 10 f - g). We interpret that in (2), magmas crossed glass transition and fragmented (e.g., Gardner, 2007; Gonnermann 2015; Cassidy et al., 2018) owing to interplaying: a) high viscosities due to tapering of GCP and VCP magmas, and increasing YWFP/B2's *VNDs*, up to *VNDs* produced in the AD 79 Vesuvius and AD 1991 Pinatubo eruptions (Fig. 9 b), driving internal stress higher than magma's brittle strength; b) fastest strain rates produced by scaling internal pressures due to syn-eruptive vesiculation, increasing magma volumes, and Uig's fastest *dP/dt* and ascent rates (e.g., Papale, 1999; Alidibirov and Dingwell, 1996; 2000), maximized

by YWFP/B2's disequilibrium degassing (Mangan and Sisson, 2000); and c) strain localization given by mingling of rheologically contrasting and syn-eruptive vesiculating YWFP/B2 and YWCP + GCP magmas, producing shear intensities locally higher than melt/crystals' tensile strength (e.g., Wright and Weinberg, 2009; Paredes-Mariño et al., 2017). These fragmentation mechanisms are consistent with YWFP/B2's delayed and subsequently extremely rapid vesiculation kinetics close to fragmentation, developing only poor permeability despite YWFP/B2's relative low viscosity and deep origin (e.g., Mueller et al., 2008); with strain localization producing GBP's fibrous tubular bubbles and broken crystals having fracture planes aligned with shear bands (e.g., Wright and Weinberg, 2009; Pál et al., 2016; Taddeucci et al., 2021); and with Uig's magma ascent at wt. avg. min. *U* inside connected dikes in most > 2 km-depths, driven by trans-tensional tectonics supporting rapid dike propagation (e.g., Lormand et al., 2020). The mechanisms of magma ascent and fragmentation in (2) involved such intense strain rates that they produced the eruption of the most energetic, laterally directed, blast-type PDCs, largely driven by their own internal pressures (e.g., Papale, 1999; Belousov et al., 2007; Fig. 10 b, c). Strikingly, no major edifice-collapse, commonly associated with fast decompression driving lateral-blast PDCs, was recognized in Uig's geological records (Torres-Orozco et al., 2017a; 2017b; 1018). Instead, we propose that the ± 5 km-deep supersaturated magmas' rapidest *dP/dt* and ascent, comparable to rates in eruptions of AD 79 Vesuvius, AD 1875 Askja, and AD 1980 Mt. St. Helens (Fig. 9 c, d), were initially powered by active tectonics. These magmas reached and overpressurized below VCP magma plugs, and first fragmented in topmost narrow Uig1 – Uig3 conduits (e.g., Thivet et al., 2020). A fragmentation wave suddenly propagated deep-down, deepening and widening the conduit up to diameters ranging from 18 to 21 m, similar to those produced in AD 1902 Mt. Pelée, AD 1912 Novarupta, and AD 1980 Mt. St. Helens (Fig. 9 d), forming AIL clasts-bearing deposits. The laterally directed PDC distributions were likely controlled by the explosive flank-collapse of domes, shaping topmost poorly developed conduits and vent geometries since Uig1 – Uig3 (e.g., Belousov et al., 2007; Cronin et al., 2013), overall similar to mechanisms

controlling blast-type PDCs in Pelean and Plinian-style eruptions of, e.g., AD 1300 and 1902 Mt. Pelée (Pichavant et al., 2002; Carazzo et al., 2012), and AD 2014 Kelud (Maeno et al., 2019).

3) In the second pre-climactic half (3), represented by layers Uig5-top – Uig6, the YWFP/B2 magma slug stopped rising, and the YWCP magma was first tapered within the most rheologically heterogeneous magma foams; producing drastic falls in wt. avg. *dP/dt*, ascent, strain, and *MDRs*, up to one order of magnitude slower than in previous pre-climactic activity (Fig. 10 h - i). During (3), tapering of the YWFP/B2 magma ended due to more viscous magmas replenishing dikes and building overpressure closer to YWCP/GCP storage levels, and the conduit developing further deeper (Fig. 10 a), both producing fluctuating *dP/dt*. Despite this change in plumbing structure, magma fragmentation was sustained by YWCP's rapid volatile diffusion and heterogeneous vesiculation kinetics (e.g., Gardner, 2007) moving the fragmentation surface deeper, along with increasing high viscosities due to tapering of all crystalline magmas individually, and decompression-induced both YWCP's vesiculation and YWCP's and GCP's microlite crystallization (e.g., Blundy et al., 2006; Gardner, 2007). In fact, YWCP's *VNDs* became nearly as high as YWFP/B2's, driving upsurging *dP/dt*, ascent, and strain rates at Uig6 (Fig. 9 a). In addition, shear fragmentation associated with strain localization became more important than in previous eruptive phases due to slowed YWFP/B2's *dP/dt* yielding to extended mingling with YWCP + GCP magmas, producing the largest vol.% of GBP in layers Uig5-top – Uig6 (Fig. 2) (e.g., Pál et al., 2016). In contrast with pre-climactic (2), decompression of relatively denser, less buoyant, and more viscous magmas in pre-climactic (3) sustained further PDC eruptions that, contrastingly, fluctuated in intensity and flowed by gravity in Uig5-top – Uig6 (Fig. 10 b, c). These PDCs, however, recorded renewed scaling YWCP's *VNDs*, which supported PDCs' reaching intensities comparable to those produced in explosive eruptive phases of, e.g., AD 1875 Askja, AD 1912 Novarupta, and AD 2008 Chaitén (Fig. 9 c, d). Thus, fragmentation mechanisms and intensities associated with gravity-driven PDC dynamics in (3) were controlled by extremely different

strain rates produced by both decompression of rheologically contrasting magmas inside syn-eruptive evolving conduits, and YWCP's degassing processes.

4) During Uig's climactic Uig7 Plinian phase (4) all magmas were tapered, including renewed decompression of supersaturated YWFP/B2 magmas, and YWCP magmas reaching Uig's highest *VNDs* (Fig. 9 a). Both magmas powered rapid *dP/dt*, ascent, and strain rates, and erupted at fast *MDRs* (Fig. 10 j - k), comparable with intensities produced in eruptions of, e.g., AD 79 Vesuvius, AD 1875 Askja, and AD 1980 Mt. St. Helens (Fig. 9 b, c, d). We interpret that Uig7's fragmentation mechanisms combined those that drove all Uig4 to Uig6 explosive events, and comprised magmas passing glass transition and breaking due to high viscosities and fast strain rates resulting from: a) tapering of all crystalline magmas, b) scaling magma internal stress during fast *dP/dt*, c) GCP's more efficient melting further fueling internal pressures by increasing magma volumes, d) YWFP/B2's delayed disequilibrium degassing, e) YWCP's decompression-induced crystallization and heterogeneous vesiculation kinetics, and f) strain localization recorded in GBP clasts. In contrast with pre-climactic explosions, magmas in the climactic Uig7 phase were decompressed inside a well-connected fixed conduit, easing magma passage (forming AIL clasts-free deposits) – only hindered by magma foam's differences in viscosities (Fig. 10 j - k). The combination of Uig's highest YWFP/B2 + YWCP *VNDs* in Uig7 suggests that fragmentation could have been reached deeper or at least stayed at the same conduit level than in Uig6. This mature conduit enabled: a) development and ascent of Uig's rheologically most homogeneous magma foams, b) YWCP's reaching the highest *VNDs* limited by viscosity only; c) balanced mingling of YWFP/B2, YWCP and GCP magmas (Fig. 9 a), and d) more efficient bubble growth and coalescence yielding into permeability development and outgassing (Mueller et al., 2008; Namiki and Manga, 2008), recorded in declining GCP's and YWFP/B2's *VNDs* between Uig7-top and Uig8 (Fig. 9 a). We conclude that the fact that this stable conduit allowed uninterrupted decompression of magmas at strain rates being fast yet slower than in Uig4 – Uig5-base, supported acceleration of magmas up to supersonic vent-exit velocities (e.g.,

Taddeucci et al., 2012; Burgisser and Degruyter, 2015; Lormand et al., 2020), and continuous eruption of buoyant and relatively coherent masses of gas and pyroclasts forming Uig's steady Plinian column (Fig. 10 b, c).

5) In Uig's post-climactic phase (5), represented by layer Uig8, all magmas continued being tapered but became denser due to: a) gradually increasing bubble coalescence developing magma permeability and outgassing (Mueller et al., 2008; Namiki and Manga, 2008), and ultimately leading to bubble collapse (Fig. 7) and YWCP's crystal aggregation (Fig. 9 a); b) YWFP/B2's and GBP-B1's latest crystallization (Fig. 9 a); and c) conduit walls' thickening due to VCP and GCP magmas' outgassing and cooling. Accordingly, velocities of all *dP/dt*, ascent, strain, and *MDR* dropped close to Uig5-top – Uig6 rates, along with the conduit further widening (Fig. 10 l). Magma outgassing and densification, and late-stage conduit widening, produced Uig8 deposits rich in AJ and ALT clasts (Fig. 2). Fragmentation was thus controlled by magmas' viscosity crossing glass transition, and internal stress intensities overcoming melts' brittle strength, powered by late-stage bubble expansion. Fragmentation from strain localization remained also active due to continuing shearing between crystalline-vesicular and YWFP/B2 magmas at relatively fast to moderate *dP/dt*. Lastly, these conditions drove Uig7's Plinian column collapse and generation of dense, gravity-driven PDCs (Fig. 10 b, c) (e.g., Shea et al., 2011). Further outgassing, cooling, and thickening of conduit walls limited bubble expansion in narrowing conduits, and generated weakly explosive waning eruptive activity (Fig. 10 m). Progressive YWFP/B2's stalling, YWFP/B2's and YWCP's prolonged outgassing by well-developed permeability, and slowing *dP/dt*, stopped Uig's fragmentation and produced effusive volcanism (e.g., Namiki and Manga, 2008; Cassidy et al., 2018).

### *5.9 Implications for andesite Plinian eruptions*

A series of alternative scenarios of potential andesite Plinian eruptions could be produced from slight yet feasible changes in Uig's conditions:

a) Based on Uig1 – Uig3, larger vol.% volatiles in VCP-type magmas, sustained magma supply, and/or magma-water interactions, could produce more energetic explosive dome-collapses, and associated BAF pulses, that would form conduits wider than in the earliest stages of the Uig, similar to eruptions from Kelud, Merapi and Pelée volcanoes (e.g., Carazzo et al., 2012; Cronin et al., 2013; Maeno et al., 2019).

b) From Uig4 – Uig5-base, the more developed and wider conduits and vent geometries could support reduced conduit overpressurization and strain of rheologically homogeneous and highly buoyant magma foams, likely producing violent Vulcanian or sub-Plinian plumes instead of laterally directed PDCs (e.g., Thivet et al., 2020). This is the case of many eruptions in Taranaki's Holocene geological records (e.g., Torres-Orozco et al., 2017a; 2018; Cronin et al., 2021), and in eruptions like, e.g., AD 2010 Merapi (e.g., Cronin et al., 2013).

c) Based on Uig5-top – Uig6, either full or partial eruption column instability due to dense magmas being tapered would produce subsequent PDCs, e.g., AD 79 Vesuvius (Shea et al., 2011), AD 1655 Taranaki (Platz et al., 2007), AD 1913 Colima (Saucedo et al., 2010). In this comparatively short-lived Plinian column scenario (e.g., Cronin et al., 2021), the eruption would reach its climax during the first plume, and will end due to the conduit developing deeper, and magmas becoming sufficiently permeable and outgassed. In consequence, YWFP/B2-type magmas would stall and crystallize, forming further YWCP-type magmas.

d) Alternatively, the YWFP/B2 magmas could neither outgas nor stall, but stay mostly buoyant due to continuous magma decompression, similar to the multi-phase Uig. In this scenario, the first plume wouldn't collapse but would remain fluctuating, probably representing the onset unsteady phase of an evolving and more energetic steady Plinian column, potentially larger than the Uig7 plume, similar to other Taranaki's last 5000 years eruptions (e.g., Torres-Orozco et al., 2017a; 2017b; 2018), and comparable to Plinian eruptions from Calbuco, Kelud, Pelée and Vesuvius (e.g., Carazzo et al., 2012; Shea et al., 2011; Romero et al., 2016; Maeno et al., 2019).

Strikingly, in any scenario, Taranaki's Plinian eruptions would comprise higher intensities than Plinian eruptions from other andesitic volcanoes in New Zealand, e.g., Tongariro and Ruapehu (Fig. 9 c). We conclude that plainly different volcano-tectonic settings, with Tongariro and Ruapehu sitting over the widely extensional and hot Taupo Volcanic Zone, in contrast with Taranaki's trans-tensional/compressional regime, far from the subduction area (e.g., Cronin et al., 2021), not only relate to different magma chemical compositions and contrasting rheologies (e.g., Pardo et al., 2014; Heinrich et al., 2020; Lormand et al., 2020), but also to activation of different decompression and strain regimes that must be further studied.

## 6. Conclusions

Uig's multiple eruption styles and explosive phases of up to Plinian scale were associated with different andesite magmas, some of which mingled to varying extents. The different andesite magmas were determined from pyroclasts comprising: a) slight variations in bulk chemistry, b) varying crystallinities, mineralogies, and melt chemical compositions; and c) variable vesicle and crystal size and shape distributions, *VNDs*, *CNDs* and *MNDs*; all indicating multiple pre- and syn-eruptive magma degassing and crystallization histories producing contrasting magma rheology. Based on magma evolution and Taranaki's last 5000 yrs. eruption records, we conclude that the Uig marked the start of a new cycle of mafic magma recharge in Taranaki's plumbing system. All magmas were decompressed and ascended to the surface in different phases and at stepwise to rapid rates under Taranaki's trans-tensional tectonics. Before decompression, most magmas experienced relatively shallow crystallization while cooling. During decompression, all magmas underwent several stages of vesiculation and crystallization. Large vol.% microphenocrysts and microlites formed during decompression implied extremely fast rates of syn-eruptive crystal nucleation and growth.

Earliest and least explosive eruptive phases of slowest decompression rates were mostly controlled by rapid volatile diffusion and exsolution. All subsequent eruptive phases were produced in rapid and intermittent decompression regimes controlled by: a) YWFP/B2's rapidest ascent, supersaturation and

delayed disequilibrium degassing, b) YWCP's decompression-induced microlite crystallization and rapid heterogeneous vesiculation kinetics inside evolving and widening conduits, and c) GBP-B1 + YWFP/B2's mingling efficiency and shear deformation intensity.

Between contiguous eruptive phases, Uig's eruption styles and intensities changed by means of magma fragmentation mechanisms consisting of either separate or mingled magmas passing glass transition because of increasing, each or all, melt viscosity, strain, and localized shear deformation; followed by magmas breaking due to their own internal stress intensities overcoming melt/crystals' brittle strength. The fragmentation mechanisms acted either individually or collectively depending on: a) slow, rapid, or intermittent rates of decompression, ascent and strain; b) intermittent or continuous tapering of each or all of the rheologically diverse magmas from separate *P-T* storage, c) distinct magma degassing and crystallization processes, d) syn-eruptive rheologically evolving magma foams, e) different fragmentation surface depths, and f) different stages of conduit maturity and vent geometry evolution. The simplest fragmentation drove Uig's vent-unroofing and conduit-opening phases through VCP magmas passing glass transition and breaking due to increasing viscosities at slowest decompression. The most intricate fragmentation mechanisms of the rheologically most homogeneous magmas powered Uig's pre-climactic blast-type PDCs and the climactic Plinian column, in which all the conditions for magmas passing glass transition met with the highest internal stress.

Slight changes in Uig's fragmentation and decompression mechanisms could produce alternative eruptive scenarios comparable to other Taranaki's Holocene eruptions, and to Plinian eruptions from andesitic to silicic volcanoes such as, e.g., Calbuco, Colima, Kelud, Merapi, Pelée and Vesuvius. For instance, more energetic initial explosive phases, possibly involving magma-water interactions, could form wider/deeper conduits and vents that would yield into short-lived, unsteady, Vulcanian to sub-Plinian plumes. However, these plumes might as well remain buoyant due to intermittent to continuous volatile-rich magma decompression, and evolve into lengthier steady Plinian eruptive phases.

## Acknowledgements

RTO is supported by a level 1 stipend of CONACyT, Mexico, National Researchers System [No. 164356]; was benefited from a UNAM's DGAPA Postdoctoral Fellowship granted in 2019 – 2021, and was supported by a UK's NERC grant to PDL [NE/M013561/1] for completing this work's digital data analyses. RTO, NP and SJC were awarded beamtime at the Australian Synchrotron in two separate applications [AS131/IM/5811 and AS142/IMBL/7939] for carrying out all μCT experiments. We are fully in debt with Anton Maksimenko for assistance during beamtime. RTO, SJC, NP and IU are funded by New Zealand's MBIE-Endeavour Project "Transitioning Taranaki to a Volcanic Future" [No. UOAX1913].

## References

Alidibirov, M.A., 1994. A model for viscous magma fragmentation during volcanic blasts. Bull. Volcanol. 56, 459-465

Alidibirov, M.A., Dingwell, D.B., 1996. Magma fragmentation by rapid decompression. Nature 380, 146-8

Alidibirov, M.A., Dingwell, D.B., 2000. Three fragmentation mechanisms for highly viscous magma under rapid decompression. J. Volcanol. Geotherm. Res. 100, 413-421

Alloway, B.V., Neall, V.E., Vucetich, C.G., 1995. Late Quaternary (post 28,000 year B.P.) tephrostratigraphy of northeast and central Taranaki, New Zealand. Journal of the Royal Society of New Zealand 25, 385-458.

Arzilli, F., La Spina, G., Burton, M.R., Polacci, M., Le Gall, N., Hartley, M.E., Di Genova, D., Cai, B., Vo, N.T., Bamber, E.C., 2019. Magma fragmentation in highly explosive basaltic

eruptions induced by rapid crystallization. Nature Geos. 12 (12), 1023–1028. https://doi.org/10.1038/s41561-019-0468-6.

Arzilli, F., Polacci, M., La Spina, G., Le Gall, N., Llewellin, E., Brooker, R., Torres-Orozco, R., Di Genova, D., Neave, D., Hartley, M.E., Mader, H., Giordano, D., Atwood, R., Lee, P., Heidelbach, F., Burton, M., 2022. Dendritic crystallization in hydrous basaltic magmas controls magma mobility within the Earth's crust. Nature Comm, **in press.**

Asimow, P.D., Ghiorso, M.S., 1998. Algorithmic Modifications Extending MELTS to Calculate Subsolidus Phase Relations. American Mineralogist 83, 1127-1131

Bagdassarov, N., Dorfman, A., Dingwell, D., 2000. Effect of alkalis, phosphorus, and water on the surface tension of haplogranite melt. Am. Mineral. 85, 33–40.

Behrens, H., Zhang, Y., Xu, Z., 2004. $H_2O$ diffusion in dacitic and andesitic melts. Geochem Cosmochem Acta 68, 5139–5150

Belousov. A., Voight, B., Belousova, M., 2007. Directed blast and blast-generated pyroclastic density currents: a comparison of the Bezymianny 1956, Mount St Helens 1980, and Soufriere Hills, Montserrat 1997 eruptions and deposits. Bull. Volcanol. 69, 701-740

Blundy, J., Cashman, K., Humphreys, M., 2006. Magma heating by decompression-driven crystallization beneath andesite volcanoes. Nature 443, 76-80, doi: 10.1038/nature05100

Burgisser, A., Degruyter, W., 2015. Magma Ascent and Degassing at Shallow Levels. In: Sigurdsson, H., Houghton, B., Rymer, H., Stix, J., McNutt, S. (eds.) The Encyclopedia of Volcanoes, Academic Press, Cambridge, Massachusetts, USA, pp. 225–236.

Burnham, C.W., Davis, N.F., 1974. The role of $H_2O$ in silicate melts: II. Thermodynamic and phase relations in the system $NaAlSi_3O_8 - H_2O$ to 10 kilobars, 700 °C to 1100 °C. Am. J. Sci. 274, 902–940.

Capra, L., Macias, J.L., Cortés, A., Dávila, N., Saucedo, R., Osorio-Ocampo, S., Arce, J.L., Gavilanes-Ruiz, J.C., Corona-Chávez, P., García-Sánchez, L., Sosa-Ceballos, G., Vázquez, R.,

2016. Preliminary report on the July 10–11, 2015 eruption at Volcán de Colima: Pyroclastic density currents with exceptional runouts and volume. J Volcanol Geoth Res 310, 39-49

Carazzo, G., Tait, S., Kaminski, E., Gardner, J.E., 2012. The recent Plinian explosive activity of Mt. Pelée volcano (Lesser Antilles): The P1 AD 1300 eruption. Bull Volcanol 74, 2187-2203

Caricchi, L., Townsend, M., Rivalta, E., Namiki, A., 2021. The build- up and triggers of volcanic eruptions. Nature Reviews. Earth and Environment. https://doi.org/10.1038s43017-021-00174-8

Cashman, K.V., Blundy, J., 2000. Degassing and crystallization of ascending andesite and dacite. Phil. Trans. Roy. Soc. 358, 1487-1513

Cashman, K.V., Scheu, B., 2015. Magmatic fragmentation. In: Sigurdsson, H., Houghton, B., McNutt, S.R., Rymer, H., Stix, J. (eds) The Encyclopedia of Volcanoes. Second edition, Elsevier, San Diego, CA, pp. 459–471. https://doi.org/10.1016/B978-0-12-3859389.00025-0.

Cassidy, M., Manga, M., Cashman, K., Bachmann, O., 2018. Controls on explosive-effusive volcanic eruption styles. Nature Comm. 9 (1), 2839, https://doi.org/10.1038/s41467018-05293-3

Cluzel, N., Laporte, D., Provost, A., Kannewischer, I., 2008. Kinetics of heterogeneous bubble nucleation in rhyolitic melts: implications for the number density of bubbles in volcanic conduits and for pumice textures. Contrib. Mineral. Petrol. 156, 745-763

Colombier, M., Gurioli, L., Druitt, T.H., Shea, T., Boivin, P., Miallier, D., Cluzel, N., 2017. Textural evolution of magma during the 9.4-ka trachytic explosive eruption at Kilian Volcano, Chaîne des Puys, France. Bull. Volcanol. 79 (2), 17. https://doi.org/10.1007/s00445-017-1099-7.

Colombier, M., Scheu, B., Wadsworth, F., Cronin, S., Vasseur, J., Dobson, K., Hess, K.U., Tost, M., Yilmaz, T., Cimarelli, C., 2018. Vesiculation and quenching during Surtseyan eruptions

at Hunga Tonga-Hunga Ha'apai volcano, Tonga. J. Geophys. Res. Solid Earth, doi: 10.1029/2017JB015357.

Cronin, S.J., Lube, G., Dayudi, D.S., Sumarti, S., Subrandiyo, S., Surono, 2013. Insights into the October-November 2010 Gunung Merapi eruption (Central Java, Indonesia) from the stratigraphy, volume and characteristics of its pyroclastic deposits: J Volc. Geoth. Res. 261, 244-259

Cronin, S.J., Zernack, A.V., Ukstins, I.A., Turner, M.B., Torres-Orozco, R., Stewart, R.B., Smith, I.E.M., Procter, J.N., Price, R., Platz, T., Petterson, M., Neall, V.E., McDonald, G.S., Lerner, G., Damaschke, M., Bebbington, M.S., 2021. The geological history and hazards of a long-lived stratovolcano, Mt. Taranaki, New Zealand. New Zealand Journal of Geology and Geophysics, doi: 10.1080/00288306.2021.1895231

Damaschke, M., Cronin, S.J., Torres-Orozco, R., Wallace, R.C., 2017. Unifying tephrostratigraphic approaches to redefine major Holocene marker tephras, Mt Taranaki, New Zealand. Journal of Volcanology and Geothermal Research 337, 29–43.

de' Michieli Vitturi, M., Clarke, A.B., Neri, A., Voight, B., 2008. Effects of conduit geometry on magma ascent dynamics in dome-forming eruptions. Earth and Planetary Science Letters 272, 567–578.

Downey, W.S., Kellett, R.J., Smith, I.E.M., Price, R.C., Stewart, R.B., 1994. New palaeomagnetic evidence for the recent eruptive activity of Mt. Taranaki, New Zealand. Journal of Volcanology and Geothermal Research 60, 15–27.

Erdmann, S., Martel, C., Pichavant, M., Kushnir, A., 2014. Amphibole as an archivist of magmatic crystallization conditions: problems, potential, and implications for inferring magma storage prior to the paroxysmal 2010 eruption of Mount Merapi, Indonesia. Contrib Mineral Petrol 167:1016, doi: 10.1007/s00410-014-1016-4

Fanara, S., Behrens, H., Zhang, Y., 2013. Water diffusion in potassium-rich phonolitic and trachytic melts. Chemical Geology 346, 149-161, doi: 10.1016/j.chemgeo.2012.09.030

Fegley, B., 2013. Practical Chemical Thermodynamics for Geoscientists, 1st ed., Elsevier, 732pp.

Gardner, J.E., 2007. Heterogeneous bubble nucleation in highly viscous silicate melts during instantaneous decompression from high pressure. Chem. Geol. 236, 1-12

Gardner, J.E., Thomas, R.M.E., Jaupart, C., Tait, S., 1996. Fragmentation of magma during Plinian volcanic eruptions. Bull Volcanol 58 (2-3), 144-162

Ghiorso, M.S., Evans, B.W., 2008. Thermodynamics of rhombohedral oxide solid solutions and a revision of the Fe-Ti two-oxide geothermometer and oxygenbarometer. American Journal of Science 308 (9), 957–1039

Giachetti, T., Gonnermann, H.M., Gardner, J.E., Burgisser, A., Hajimirza, S., Earley, T.C., Truong, N., Toledo, P., 2019. Bubble coalescence and percolation threshold in expanding rhyolitic magma. Geoch Geoph Geos, doi.org/10.1029/2018GC008006

Gonnermann, H.M., 2015. Magma Fragmentation. Annu. Rev. Earth Planet. Sci. 43, 431-458, doi: 10.1146/annurev-earth-060614-105206

Gonnermann, H.M., Manga, M., 2013. Dynamics of magma ascent in the volcanic conduit. In: Fagents, S., Gregg, T., Lopes, R., (Eds). Modeling Volcanic Processes: The Physics and Mathematics of Volcanism (pp. 55-84). Cambridge: Cambridge University Press. doi:10.1017/CBO9781139021562.004

Gruender, K., Stewart, R.B., Foley, S., 2010. Xenoliths from the sub-volcanic lithosphere of Mt. Taranaki, New Zealand. Journal of Volcanology and Geothermal Research 190, 192-202.

Gurioli, L., Harris, A., Houghton, B., Polacci, M., Ripepe, M., 2008. Textural and geophysical characterization of explosive basaltic activity at Villarrica volcano. J. Geophys. Res. Solid Earth 113 (B8). https://doi.org/10.1029/2007JB005328.

Gurioli, L., Houghton, B.F., Cashman, K.V., Cioni, R., 2005. Complex changes in eruption dynamics during the 79 AD eruption of Vesuvius. Bull Volcanol 67, 144-159

Hajimirza, S., Gonnermann, H.M., Gardner, J.E., 2021. Reconciling bubble nucleation in explosive eruptions with geospeedometers. Nature Comm. 12 (1), doi: 10.1038/s41467-020-20541-1

Hammarstrom, J.M., Zen, E-an., 1986. Aluminum in hornblende: An empirical igneous geobarometer. American Mineralogist 71, 1297-1313.

Hawthorne, F.C., Oberti, R., Harlow, G.E., Maresch, W.V., Martin, R.F., Schumacher, J.C., Welch, M., 2012. Nomenclature of the amphibole supergroup. IMA Report. American Mineralogist 97, 2031–2048, http://dx.doi.org/10.2138/am.2012.4276

Heinrich, M., Cronin, S.J., Torres-Orozco, R., Colombier, M., Scheu, B., Pardo, N., 2020. Micro-porous pyroclasts reflecting multi-vent basaltic-andesite Plinian eruptions at Mt. Tongariro, New Zealand. Journal of Volcanology and Geothermal Research 401, 106936, https://doi.org/10.1016/j.jvolgeores.2020.106936

Henrys, S., Reyners, M., Bibby, H., 2003. Exploring the plate boundary structure of North Island, New Zealand. EOS, Trans Am. Geophys Union 84, 289-294

Holland, T., Blundy, J., 1994. Non-ideal interactions in calcic amphiboles and their bearing on amphibole-plagioclase thermometry. Contributions to Mineralogy and Petrology 116, 433-447.

Houghton, B.F., Wilson, C.J.N., 1989. Vesicularity index for pyroclastic deposits. Bull Volcanol 51, 451-462

Hughes, E.C., Neave, D.A., Dobson, K.J., Withers, P.J., Edmonds, M., 2017. How to fragment peralkaline rhyolites: observations on pumice using combined multi-scale 2D and 3D imaging. J. Volcanol. Geotherm. Res. 336, 179–191. https://doi.org/10.1016/j.jvolgeores.2017.02.020

King, P.R., Thrasher, G.P., 1996. Cretaceous-Cenozoic geology and petroleum systems of the Taranaki Basin, New Zealand. Institute of Geological and Nuclear Sciences Monograph 13

Klug, C., Cashman, K.V., Bacon, C.R., 2002. Structure and physical characteristics of pumice from the climactic eruption of Mt Mazama (Crater Lake), Oregon. Bull Volcanol 64, 486-501

Larocque, J., Canil, D., 2010. The role of amphibole in the evaluation of arc magmas and crust: the case from the Jurassic Bonanza arc section, Vancouver Island, Canada. Contributions to Mineralogy and Petrology 159, 475-492.

Lavallée, Y., Dingwell, D.B., Johnson, J.B., Cimarelli, C., Hornby, A.J., Kendrick, J.E., von Aulock, F.W., Kennedy, B.M., Andrews, B.J., Wadsworth, F.B., Rhodes, E., Chigna, G., 2015. Thermal vesiculation during volcanic eruptions. Nature 528, doi:10.1038/nature16153

Leake, B., Woolley, A.R., Birch, W.D., Burke, E.A.J., Ferraris, G., Grice, J.D., Hawthorne, F.C., Kisch, H.J., Krivovichev, V.G., Schumacher, J.C., Stephenson, N.C.N., Whittaker, E.J.W., 2004. Nomenclature of amphiboles: Additions and revisions to the International Mineralogical Association's amphibole nomenclature. American Mineralogist 89, 883–887

Li, X., Zhang, C., Behrens, H., Holtz, F., 2020. Calculating amphibole formula from electron microprobe analysis data using a machine learning method based on principal components regression. Lithos 362-363, https://doi.org/10.1016/j.lithos.2020.105469

Lin, Q., Neethling, S., Dobson, K.J., Courtois, L., Lee, P.D., 2015. Quantifying and minimizing systematic and random errors in X-ray micro-tomography based volume measurements. Comput. Geosc. 77, 1–7. https://doi.org/10.1016/j.cageo.2014.12.008.

Lledo, H.L., Jenkins, D.M., 2008. Experimental Investigation of the Upper Thermal Stability of Mg-rich Actinolite; Implications for Kiruna-Type Iron Deposits. Journal of Petrology 49 (2), 225-238, doi:10.1093/petrology/egm078

Locock, A.J., 2014. An Excel spreadsheet to classify chemical analyses of amphiboles following the IMA 2012 recommendations. Computers & Geosciences 62, 1-11, doi: 10.1016/j.cageo.2013.09.011

Lormand, C., Zellmer, G.F., Kilgour, G.N., Németh, K., Palmer, A.S., Sakamoto, N., Yurimoto, H., Kuritani, T., Iizuka, Y., Moebis, A., 2020. Slow Ascent of Unusually Hot Intermediate Magmas Triggering Strombolian to Sub-Plinian Eruptions. Journal of Petrology 61, 10, doi:10.1093/petrology/egaa077

Mader, H.M., 1998. Conduit flow and fragmentation. In: JS Gilbert y RSJ Sparks, eds., The physics of explosive volcanic eruptions. Geol Soc Lon Spec Publ 145, 51-71

Maeno, F., Nakada, S., Yoshimoto, M., Shimano, T., Hokanishi, N., Zaennudin, A., Iguchi, M., 2019. A sequence of a plinian eruption preceded by dome destruction at Kelud volcano, Indonesia, on February 13, 2014, revealed from tephra fallout and pyroclastic density current deposits. J. Volcanol. Geoth Res 382, 24-41, http://dx.doi.org/10.1016/j.jvolgeores.2017.03.002

Mangan, M.T., Sisson, T., 2000. Delayed, disequilibrium degassing in rhyolite magma: decompression experiments and implications for explosive volcanism. Earth Planet. Sci. Lett. 183, 441-455

Marsh, B.D., 1984. Mechanics and energetics of magma formation and ascension. In: Boyd, F.R. (Ed) Explosive Volcanism: Inception, Evolution, and Hazards. National Academy Press, Washington, DC, pp. 67–83.

Marsh, B.D., 2015. Magma chambers. Encyclopedia of Volcanoes. Academic Press, San Diego, CA, United States. https://doi.org/10.1016/B978-0-12-385938-9.00008-0.

Mortimer, N., Tulloch, A.J., Ireland, T.R., 1997. Basement geology of Taranaki and Wanganui Basins, New Zealand. NZ J Geol Geoph 40, 223-236

Mueller, S., Scheu, B., Spieler, O., Dingwell, D.B., 2008. Permeability control on magma fragmentation. Geology 36 (5), 399-402

Mutch, E.J.F., Blundy, J.D., Tattitch, B.C., Cooper, F.J., Brooker, R.A., 2016. An experimental study of amphibole stability in low‐pressure granitic magmas and a revised Al‐in‐hornblende geobarometer. Contrib Mineral Petrol 171, 85, doi:10.1007/s00410-016-1298-9

Namiki, A., Manga, M., 2008. Transition between fragmentation and permeable outgassing of low viscosity magmas. J. Volcanol. Geotherm. Res. 169, 48-60

Neall, V.E., 1972. Tephrochronology and tephrostratigraphy of western Taranaki (N108-109), New Zealand. NZ J Geol Geoph 15, 507-557

Nimis, P., 1999. Clinopyroxene geobarometry of magmatic rocks. Part 2. Structural geobarometers for basic to acid, tholeiitic and mildly alkaline magmatic systems. Contributions to Mineralogy and Petrolgy 135, 62–74

Nimis, P., Taylor, W.R., 2000. Single clinopyroxene thermobarometry for garnet peridotites. Part I. Calibration and testing of a Cr-in-Cpx barometrer and an enstatite-in-Cpx thermometer. Contributions to Mineralogy and Petrolgy 139, 541–554

Okumura, S., Nakamura, M., Tsuchiyama, A., 2006. Shear-induced bubble coalescence in rhyolitic melts with low vesicularity. Geophys. Res. Lett. 33 (20), 1-5

Pál, G., Jánosi, Z., Kun, F., Main, I.G., 2016. Fragmentation and shear band formation by slow compression of brittle porous media. Physical Review E, doi: 10.1103/PhysRevE.94.053003

Palladino, D.M., Simei, S., Kyriakopoulos, K., 2008. On magma fragmentation by conduit shear stress: Evidence from the Kos Plateau Tuff, Aegean Volcanic Arc. J. Volcanol. Geotherm. Res. 178, 807-817

Papale, P., 1999. Strain-induced magma fragmentation in explosive eruptions: Nature 397, 425-428

Pardo, N., Cronin, S.J., Wright, H.M.N., Schipper, C.I., Smith, I., Stewart, R.B., 2014. Pyroclastic textural variation as an indicator of eruption column steadiness in andesitic Plinian eruptions at Mt. Ruapehu. Bull Volcanol 76, 822

Paredes-Mariño, J., Dobson, K.J., Ortenzi, G., Kueppers, U., Morgavi, D., Petrelli, M., Hess, K.-U., Laeger, K., Porreca, M., Pimentel, A., Perugini, D., 2017. Enhancement of eruption explosivity by heterogeneous bubble nucleation triggered by magma mingling. Scientific Reports 7, 16897, doi: 10.1038/s41598-017-17098-3

Pérez, W., Freundt, A., Kutterolf, S., Schmincke, H.U., 2009. The Masaya Triple Layer: A 2100 year old basaltic multi-episodic Plinian eruption from the Masaya Caldera Complex (Nicaragua). J. Volcanol. Geotherm. Res. 179, 191-205

Pichavant, M., Martel, C., Bourdier, J.L., Scaillet, B., 2002. Physical conditions, structure, and dynamics of a zoned magma chamber: Mount Pelee (Martinique, Lesser Antilles Arc). J. Geoph. Res. 107, doi: 10.1029/2001JB000315

Platz, T., Cronin, S.J., Cashman, K.V., Stewart, R.B., Smith, I.E.M., 2007. Transitions from effusive to explosive phases in andesite eruptions-A case-study from the AD 1655 eruption of Mt. Taranaki, New Zealand. J Volcanol Geoth Res 161, 15-34

Platz, T., Cronin, S.J., Procter, J.N., Neall, V.E., Foley, S.F., 2012. Non-explosive dome-forming eruptions at Mt. Taranaki, New Zealand. Geomorphology 136, 15-30

Pleše, P., Higgins, M.D., Baker, D., Prašek, M.K., 2019. Nucleation and growth of bubbles on plagioclase crystals during experimental decompression degassing of andesitic melts. J. Volcanol. Geotherm. Res. 388, 106679, https://doi.org/10.1016/j.jvolgeores.2019.106679

Pleše, P., Higgins, M.D., Mancini, L., Lanzafame, G., Brun, F., Fife, J., Casselman, J., Baker, D.R., 2018. Dynamic observations of vesiculation reveal the role of silicate crystals in bubble

nucleation and growth in andesitic magmas. Lithos 296, 532–546. https://doi.org/10.1016/j.lithos.2017.11.024

Polacci, M., Baker, D.R., Mancini, L., Favretto, S., Hill, R.J., 2009. Vesiculation in magmas from Stromboli and implications for normal Strombolian activity and paroxysmal explosions in basaltic systems. J. Geophys. Res. 114, B01206, doi:10.1029/2008JB005672

Polacci, M., Baker, D.R., Mancini, L., Tromba, G., Zanini, F., 2006. Three-dimensional investigation of volcanic textures by X-ray microtomography and implications for conduit processes. Geoph Res Lett 33

Price, R.C., Gamble, J.A., Smith, I.E.M., Stewart, R.B., Eggins, S., Wright, I.C., 2005. An integrated model for the temporal evolution of andesites and rhyolites and crustal development in New Zealand's North Island. J. Volcanol. Geotherm. Res. 140 (1-3), 1-24

Price, R.C., Stewart, R.B., Woodhead, J.D., Smith, I.E.M., 1999. Petrogenesis of high-K arc magmas: evidence from Egmont Volcano, North Island, New Zealand. Journal of Petrology 40, 167-197.

Proussevitch, A.A., Sahagian, D.L., Tsentalovich, E.P., 2007. Statistical analysis of bubble and crystal size distributions: Formulations and procedures. J. Volcanol. Geotherm. Res. 164, 95-111

Putirka, K. D., 2008. Thermometers and barometers for volcanic systems. In: Putirka, K. D., Tepley, F. (eds) Mineralogical Society of America and Geochemical Society, Reviews in Mineralogy and Geochemistry 69, 61–120.

Putirka, K.D., 2016. Amphibole thermometers and barometers for igneous systems and some implications for eruption mechanisms of felsic magmas at arc volcanoes. American Mineralogist 101, 841-858.

Ridolfi, F., Renzulli, A., 2012. Calcic amphiboles in calcalkaline and alkaline magmas: thermobarometric and chemometric empirical equations valid up to 1130 $^{o}$C and 2.2 GPa. Contributions to Mineralogy and Petrology 163, 877-895

Ridolfi, F., Renzulli, A., Puerini, M., 2010. Stability and chemical equilibrium of amphibole in calc-alkaline magmas: an overview, new thermobarometric formulations and application to subduction-related volcanoes. Contributions to Mineralogy and Petrology 160 (1), 45–66

Romero, J.E., Morgavi, D., Arzilli, F., Daga, R., Caselli, A., Reckziegel, F., Viramonte, J., Díaz-Alvarado, J., Polacci, M., Burton, M., Perugini, D., 2016. Eruption dynamics of the 22–23 April 2015 Calbuco Volcano (Southern Chile): Analyses of tephra fall deposits. J Volcanol Geoth Res 317, 15-29, doi: 10.1016/j.jvolgeores.2016.02.027

Rotella, M.D., Wilson, C.J., Barker, S.J., Cashman, K.V., Houghton, B.F., Wright, I.C., 2014. Bubble development in explosive silicic eruptions: insights from pyroclast vesicularity textures from Raoul volcano (Kermadec arc). Bull. Volcanol. 76 (8), 826, https://doi.org/10.1007/s00445-014-0826-6

Sable, J.E., Houghton, B.F., Del Carlo, P., Coltelli, M., 2006. Changing conditions of magma ascent and fragmentation during the Etna 122 BC basaltic Plinian eruption: Evidence from clast microtextures. J Volcanol Geoth Res 158, 333-354

Saucedo, R., Macías, J.L., Gavilanes, J.C., Arce, J.L., Komorowski, J.C., Gardner, J.E., Valdez-Moreno, G., 2010. Eyewitness, stratigraphy, chemistry, and eruptive dynamics of the 1913 Plinian eruption of Volcán de Colima, México: J Volcanol Geoth Res 191, 149-166

Shea, T., 2017. Bubble nucleation in magmas: a dominantly heterogeneous process? J. Volcanol. Geotherm. Res. 343, 155–170. https://doi.org/10.1016/j.jvolgeores.2017.06.025

Shea, T., Gurioli, L., Houghton, B.F., Cioni, R., Cashman, K.V., 2011. Column collapse and generation of pyroclastic density currents during the AD 79 eruption of Vesuvius: the role of pyroclast density. Geology 39 (7), 695-698

Shea, T., Houghton, B.F., Gurioli, L., Cashman, K.V., Hammer, J.E., Hobden, B.J., 2010. Textural studies of vesicles in volcanic rocks: An integrated methodology. J. Volcanol. Geotherm. Res. 190, 271-289

Sherburn, S., White, R.S., 2006. Tectonics of the Taranaki region, New Zealand: earthquake focal mechanisms and stress axes. NZ J Geol and Geoph 49, 269-279

Sherburn, S., White, R.S., Chadwick, M., 2006. Three-dimensional tomographic imaging of the Taranaki volcanoes, New Zealand. Geophysical Journal International 166, 957-969.

Stagpoole, V., Nicol, A., 2008. Regional structure and kinematic history of a large subduction back thrust: Taranaki Fault, New Zealand. J Geoph Res: Solid Earth, 113(B1)

Taddeucci, J., Cimarelli, C., Alatorre‐Ibargüengoitia, M.A., Delgado-Granados, H., Andronico, D., Del Bello, E., Scarlato, P., Di Stefano, F., 2021. Fracturing and healing of basaltic magmas during explosive volcanic eruptions. Nature Geoscience 14, 248-254, doi: 10.1038/s41561-021-00708-1

Taddeucci, J., Scarlato, P., Capponi, A., Del Bello, E., Cimarelli, C., Palladino, D. M. and Kueppers, U., 2012. High-speed imaging of Strombolian explosions: The ejection velocity of pyroclasts. Geophysical Research Letters 39.

Thivet, S., Gurioli, L., Di Muro, A., Derrien, A., Ferrazzini, V., Gouhier, M., Coppola, D., Galle, B., Arellano, S., 2020. Evidences of Plug Pressurization Enhancing Magma Fragmentation During the September 2016 Basaltic Eruption at Piton de la Fournaise (La Réunion Island, France). Geochemistry Geophysics Geosystems, doi: 10.1029/2019GC008611

Toramaru, A., 2006. BND (bubble number density) decompression rate meter for explosive volcanic eruptions. J. Volcanol. Geotherm. Res. 154, 303-316

Toramaru, A., Noguchi, S., Oyoshihara, S. and Tsune, A., 2008. MND (microlite number density) water exsolution rate meter. Journal of Volcanology and Geothermal Research 175, 156–167.

Torres-Orozco, R., Cronin, S.J., Damaschke, M., Pardo, N., 2017b. Diverse dynamics of Holocene mafic-intermediate Plinian eruptions at Mt. Taranaki (Egmont), New Zealand. Bull Volcanol 79, 76, doi: 10.1007/s00445-017-1162-4

Torres-Orozco, R., Cronin, S.J., Pardo, N., Palmer, A.S., 2017a. New insights into Holocene eruption episodes from proximal deposit sequences at Mt. Taranaki (Egmont), New Zealand. Bull Volcanol 79 (3), 1-25, doi 10.1007/s00445-016-1085-5

Torres-Orozco, R., Cronin, S.J., Pardo, N., Palmer, A.S., 2018. Volcanic hazard scenarios for multi-phase andesitic Plinian eruptions from lithostratigraphy: insights into pyroclastic density current diversity at Mount Taranaki, New Zealand. GSA Bull, doi:10.1130/B31850.1

Turner, M.B., Bebbington, M.S., Cronin, S.J., Stewart, R.B., 2009. Merging eruption datasets: building an integrated Holocene eruptive record for Mt. Taranaki, New Zealand. Bull. Volcanol. 71, 903-918

Turner, M.B., Cronin, S.J., Bebbington, M.S., Platz, T., 2008 a. Developing probabilistic eruption forecasts for dormant volcanoes: a case study from Mt Taranaki, New Zealand. Bull Volcanol 70, 507-515

Turner, M.B., Cronin, S.J., Bebbington, M.S., Smith, I.E.M., Stewart, R.B., 2011. Integrating records of explosive and effusive activity from proximal and distal sequences: Mt. Taranaki, New Zealand. Quaternary Intl 246, 364-373

Turner, M.B., Cronin, S.J., Smith, I.E.M., Stewart, R.B., Neall, V.E., 2008 b. Eruption episodes and magma recharge events in andesitic systems, Mt Taranaki, New Zealand. J Volcanol Geoth Res 177, 1063-1076

Wright, H.M.N., Weinberg, R.F., 2009. Strain localization in vesicular magma: Implications for rheology and fragmentation. Geology 37, 1023-1026

Yavuz, F., 2013. WinPyrox: A Windows program for pyroxene calculation classification and thermobarometry. Am. Mineral. 98, 1338-1359.

Yavuz, F., Döner, Z., 2017. WinAmptb: A Windows program for calcic amphibole thermobarometry. Periodico di Mineralogia 86, 135-167, doi: 10.2451/2017PM710

Yoder Jr., H.S., 1965. Diopside–anorthite–water at five and ten kilobars and its bearing on explosive volcanism. Yearbook of Carnegie Institution of Washington 64, 82–89

Zernack, A.V., Cronin, S.J., Neall, V.E., Procter, J.N., 2011. A medial to distal volcaniclastic record of an andesite stratovolcano: Detailed stratigraphy of the ring-plain succession of south-west Taranaki, New Zealand. International Journal of Earth Sciences 100, 1936-1966

Zernack, A.V., Price, R.C., Smith, I.E.M., Cronin, S.J., Stewart, R.B., 2012. Temporal Evolution of a High-K Andesitic Magmatic System: Taranaki Volcano, New Zealand. J Petrol 53 (2), 325-363

Zhang, Y., Behrens, H., 2000. $H_2O$ diffusion in rhyolitic melts and glasses. Chem Geol 169, 243-262

**Figure Captions**

**Fig. 1** (a) Tectonic setting of the North Island (NI) of New Zealand (modified from King and Thrasher, 1996; Henrys et al., 2003; Sherburn and White, 2006; Stagpoole and Nicol, 2008). Cape Egmont Fault Zone (CEFZ), Mount Ruapehu (R), South Island (SI), Taranaki Fault (TF), Taranaki Volcanic Lineament (TVL, yellow line), Taupo Volcanic Zone (TVZ). (b) Zoomed area of the Taranaki Peninsula. The TVL (Neall 1972) includes: Paritutu, Kaitake, Pouakai and Mt. Taranaki (and the satellite cone of Fanthams Peak). Trans-tensional Faults: Inglewood (IGF), Manaia (MF) and Norfolk (NFF). Main studied sites and isopachs (cm-thick) of fall deposits (layer Uig7) produced by the 3300 cal BP Upper Inglewood eruptive episode (Uig; Torres-Orozco et al., 2017a; 2017b; 2018) are outlined. (c) Zoomed area of Mt. Taranaki's eastern flanks, and Uig's pyroclastic density current (PDC) deposit distributions (Uig1 – Uig6; Torres-Orozco et al., 2017b). NZGD 2000 New Zealand Transverse Mercator.

**Fig. 2** Lithostratigraphic layers (Uig1 – Uig8) and interpretation of associated surface processes, eruption magnitude (M), componentry, and pumice density data of the 3300 cal BP Upper Inglewood eruptive episode (Uig) compiled from Torres-Orozco et al. (2017a; 2017b; 2018). Dense clasts'

classification and densities determined in this work. Shaded area in the density section represents weighted mean, minimum and maximum bulk densities of each Uig layer. Bulk vesicularity limits (in vol.%) are indicated. Particle-concentrated (C), dilute (D), pyroclastic density current (PDC), block-and-ash flow (BAF), free crystals (FC). The rest of initials were described in the legend.

**Fig. 3** Backscatter electron photomicrographs of the range of pumice textures of the Upper Inglewood eruptive episode (Torres-Orozco et al., 2017a; 2017b; 2018), and binary diagrams of major-element chemical compositions of mineral phases identified: amphibole (Amp), clinopyroxene (Cpx), plagioclase (Plg), Fe-Ti oxides (Ox). From left to right columns, micrographs are displayed in original (a – f, 500x magnification), binarized, zoomed (a' – f', 1000x – 2000x), and segmented formats (yellow glass, purple crystals, blue oxide crystals). Notice YWFP's and GBP-B2's holohyaline groundmass, VCP's highest microcrystallinity, YWCP's finest vesicles, GCP's and GBP-B1's vesicle/crystal textures, and GBP's deformed vesicle areas (red shading). Notice YWFP/GBP-B2 (B2)'s restricted mineral compositions: anorthite (An) and bytownite (By) ± diopside ± Mg-hastingsite (mostly Ti-rich MgHst) ± titanomagnetite (Tmn). The rest includes labradorite (La), andesine (Ad), augite, actinolite, and hematite (Hm).

**Fig. 4** X-rays computed microtomography and glass chemistry. (a) Single x-rays attenuation slice (1000 slices total per scan), (b) complete segmented 3D-volume renderings (black crystals, grey filled-vesicles, and yellow groundmass), and (c) segmented 3D-subvolume renderings of the range of pumice textures of the Upper Inglewood eruptive episode (Uig; Torres-Orozco et al., 2017a; 2017b; 2018). Bulk vol.% vesicles (Vf) and crystals (Cf) are indicated. GBP's grey-YW crystalline (B1) and YW foamy (B2) bands are delimited. Notice the least crystalline and glassiest YWFP (c1), and the most crystalline VCP (c5). (d) Binary diagrams of Uig's major-element pumice glass chemical compositions. Basaltic-andesite (BA), basaltic trachyandesite (TBA), andesite (A), trachyandesite (TA), dacite (D), trachydacite (TD), rhyolite (R). Other glass compositions: Fanthams Peak eruptives (FPE) and AD 1655 Burrell pumice (BU) (Damaschke et al., 2017), and ultramafic (Ux, light-grey) and intermediate-plutonic (Ix, dark-grey)

xenoliths (Gruender et al., 2010). Pyroxene (Px) + olivine (Ol) fractional crystallization (FC). Notice YWFP's least silicic rhyolite, and YWCP's TBA and D glasses, comparable to FPE and BU, respectively.

**Fig. 5** 3D-subvolume renderings of Upper Inglewood (Uig)'s pumice vesicles (c1 – c5) classified by shape (shape factor) and volume (in $\mu m^3$ intervals), and vesicle shape distributions for each pumice type per layer (Uig1 – Uig8). Shape factors are proportional and inversely proportional, respectively, with vesicle elongation and sphericity. (c4) GBP-B2's fibrous-tubular vesicles. A graphic scale (1:1) of vesicle volumes was included. Notice YWFP's highly spherical vesicles, GBP's shape and size contrasting vesicle bands, and VCP's 3D-spindly vesicles. Different processes transforming each pumice type's vesicle shape distributions with stratigraphic time were inferred.

**Fig. 6** 3D-subvolume renderings of Upper Inglewood (Uig)'s pumice crystals (c1 – c5) classified by habit (shape factor) and volume (in $\mu m^3$ intervals), and crystal shape distributions for each pumice type per layer (Uig1 – Uig8). Shape factors are proportional and inversely proportional, respectively, with crystal elongation and sphericity. Particle rugosity was employed to discriminate between euhedral, subhedral, and anhedral crystals. A graphic scale (1:1) of crystal volumes was included. Notice YWFP's lowermost microcrystallinities, YWCP's and VCP's highest microcrystallinities, and GBP bands' contrasting microcrystallinities. Different processes controlling each pumice type's crystal shape distributions with stratigraphic time were inferred.

**Fig. 7** Vesicle and crystal volume and cumulative volume distributions of all Upper Inglewood (Uig)'s pumice types at every layer (Uig1 – Uig8). Interpretation of bubble kinetics: (a) single stage nucleation-growth, (b) collapse, (c) multiple stages of nucleation-growth, (d) fresh continuous/accelerating nucleation-growth following (e) old coalescence; (f) general ripening, (g) shear deformation-induced growth/coalescence. Interpretation of crystal kinetics: (h) single stage nucleation-growth, (i) multiple stages of nucleation-growth. Two different crystallization histories in a single Uig layer: (j1) fresh

accelerating microlite crystallization gradually passing to older stage microphenocrysts, and (j2) single stage microlite crystallization abruptly passing to old "cold" microphenocrysts. Crystal size evolution during the Uig: from (k1) old microphenocrysts-dominated (Uig1), to (k2) fresh microlites-dominated (Uig8).

**Fig. 8** Phase diagrams of plagioclase, diopside, and amphibole of Upper Inglewood (Uig)'s pumice types, using results from geothermobarometry (Table 5). (a) Plagioclase liquidi calculated using MELTS (Asimow and Ghiorso, 1998), and data of this work, Damaschke et al. (2017), and Torres-Orozco et al. (2017b). (b) Uig's different *P-T* conditions compared with water-saturated albite and anorthite (An) + diopside (Di) liquidi from Yoder (1965) and Burnham and Davis (1974). (c) Uig's low *P-T* actinolites and high *P-T* amphiboles compared with stability curves of Lledo and Jenkins (2008), and water-saturated haplogranite solidus of Mutch et al. (2016).

**Fig. 9** Upper Inglewood (Uig)'s rates of magma decompression (*dP/dt*), min. ascent, and mass discharge (*MDR*), conduit diameters, and vesicle (*VND*) and microlite (*MND*) number densities. (a) Stratigraphic time-constrained (Uig1 – Uig8) diagrams of *VND*, *MND*, and corresponding *VND dP/dt* (heterogeneous surface tension, 2 – 3 wt.% $H_2O$) and *MND dP/dt* (4 wt.% $H_2O$) for each pumice type. Notice evolution of Uig's magma degassing and crystallization processes recorded by pumice types' diverse vesicle and microlite textures. IZO1986: AD 1986B Izu-Oshima eruption's *MND* and *dP/dt* from Toramaru et al. (2008). Mass-balancing magma mingling curves in *MND* diagrams were defined using YWCP, GCP, GBP-B1 and GBP-B2's *CND*, *Cf* and *MND*. Crystal aggregation (CA), decompression-induced crystallization (DC), decreasing decompression (DD), intermittent decompression (ID), rapid decompression (RD), stepwise decompression (SD). (b) Diagram of weighted average *VND* and *VND dP/dt* for each Uig layer (homogeneous and heterogeneous surface tensions). (c) Diagram of each Uig layer's *MDR* and *VND dP/dt*. Three different decompression regimes were identified. Corresponding estimated minimum conduit diameters (D) are indicated. (d) Diagram of each Uig layer's minimum weighted average magma ascent rate (*U*) and minimum D. Data of 9.4 ka Kilian from Colombier et al.

(2017), and 13,000 cal BP Ruapehu from Pardo et al. (2014). The rest of eruption data compiled in Shea (2017), Cassidy et al. (2018), and references therein.

**Fig. 10** (a) Conceptual model of Mt. Taranaki's plumbing system, and Upper Inglewood (Uig) magmas' storage depths, temperature gradient (dashed line) and differentiation trail. Melts: basaltic-andesite (BA), andesite (A), dacite (D), rhyolite (R). Fractional crystallization (FC). Crystals: anorthite (An), clinopyroxene (Cpx), Mg-hastingsite (MgHst), olivine (Ol), pyroxenes (Px), titanomagnetite (Tmn). (b) Diagram of each Uig layer's weighted average relative magma buoyancy (B), strain rate (SR), and viscosity (n). Arrows outline Uig's progression (Uig1 – Uig8). Horizontal dashed lines separate distinct SR fields in which Uig's gravity-driven pyroclastic density currents (PDCs), including block-and-ash flows (BAF), Plinian columns, and internal pressure-driven PDCs occurred. (c) Sketch of Uig's eruption progression, different eruption styles and mechanisms. (d–m). Conceptual model of upper conduit's magma foam architecture, foam evolution, conduit diameter, and min. ascent velocity profiles, for every type of magma during each Uig's eruptive phase (Uig1 – Uig8). Weighted average vesicle number densities and rates of magma decompression, ascent (minimum) and mass discharge are included. Red arrows represent shearing planes between magmas mingling, deforming, and producing GBP. Blue arrows represent magmas cooling, outgassing, and conduit walls thickening.

Table 1. General characteristics of the Uig vesicular and dense pyroclasts

| | Vesicular Juvenile Clasts | | | | | |
|---|---|---|---|---|---|---|
| | Yellow-White Foamy Pumice (YWFP) | Yellow-White Crystalline Pumice (YWCP) | Grey Crystalline Pumice (GCP) | Grey Banded Pumice (GBP) | | Violet Crystalline Pumice (VCP) |
| | | | | Banded (B1 and B2 bands) | | |
| Generalities | Porphyritic, seriated. Holohyaline and highly vesicular groundmass. Foamy appearance | Porphyritic, seriated. Hypocrystalline and moderately to highly vesicular groundmass | Porphyritic, seriated. Hypocrystalline and moderately vesicular groundmass | Grey-YW crystalline (B1): hypocrystalline and moderately vesicular groundmass | YW foamy (B2): holohyaline and highly vesicular groundmass | Porphyritic, seriated. Hypocrystalline and poorly vesicular groundmass |
| Presence | 14 – 30 vol.% from Uig4 to Uig8. Most abundant component of Uig4, Uig5-base and Uig7 | 15 – 39 vol.% from Uig5-top to Uig8. Most abundant component of Uig5-top and Uig6 | 6 – 13 vol.% from Uig5 to Uig8. Least abundant pumice type overall | 11 – 18 vol.% from Uig4 to Uig8. Second most abundant component from Uig4 to Uig6 | | 2 – 8 vol.% from Uig4 to Uig8. Up to 20 vol.% and only vesicular component from Uig1 to Uig3 |
| $\rho_{bulk}$ (kg m^-3) | 700 – 860 | 1020 – 1100 | 1350 – 1580 | 1070 – 1280 | | 1960 – 2200 |
| Vesicularity (vol.%) | 59 – 64 | 53 – 60 | 39 – 51 | 49 – 56 | 59 – 63 | 15 – 21 |
| Vesicle wall thickness (μm) | 1 – 10 (smooth) | 0.5 – 10 (rare 10-30) | 5 – 25 (rugged) | 5 – 20 | 1 – 10 | 10 – 20 |
| Glass phase (vol.%) | 17 – 24 | 13 – 19 | 15 – 25 | 10 – 21 | 16 – 24 | 20 – 32 |
| Crystal phase (vol.%) | 17 – 23 | 27 – 31 | 27 – 33 | 27 – 41 | 14 – 21 | 54 – 59 |
| Microcrystal (vol.%) | < 1 | 4 – 9 | 3 – 7 | 2 – 10 | < 1 | 6 – 23 |

Table 1 continues

| | Dense Clasts | | | |
|---|---|---|---|---|
| | Dense Andesite Juveniles (AJ) | "Old-Dome" Accessory Dense Andesite Lithics (OD-AL) | Accidental Altered Lithics (ALT) | Accidental Intrusive Lithics (AIL) |
| Generalities | Dark (amphibole)-speckled, light grey, porphyritic. Hypocrystalline and very poorly vesicular groundmass hosting plagioclase and amphibole | White (plagioclase)-speckled, dark grey, porphyritic. Lower fractions of amphibole phenocrysts than the AJ. Groundmass clinopyroxene and amphibole microlites >>> plagioclase | Light grey clasts, red/orange-stained faces. Moderately sorted quartz and hydrothermally altered opaque and white grains. Microgranular matrix (50-80 vol.%). | Fine-grained phaneritic with plagioclase, feldspar, quartz, amphibole, and rare clinopyroxene |
| Presence | All layers. Most abundant component (22 – 35 vol.%) of Uig3 and Uig8 | All layers. Most abundant component (38 – 42 vol.%) of Uig1 and Uig2 | 7 vol.% of most Uig layers, and up to 12 vol.% of Uig8 | 1 – 2 vol.% of layers Uig5 and Uig6 |
| $\rho_{bulk}$ (kg m^-3) | 2300 – 2670 | 2540 – 2670 | 2230 – 2530 | 2660 – 2700 |
| Vesicularity (vol.%) | 10 | < 5 | Porosity: 9 – 14 | |
| Vesicle wall thickness (μm) | N/A | N/A | | Taranaki's plutonic xenoliths reported in Gruender et al. (2010). |
| Glass phase (vol.%) | 35 – 45 (including microlites) | 30 – 42 (including microlites) | N/A: sedimentary to metasedimentary xenoliths described in Gruender et al. (2010) | |
| Crystal phase (vol.%) | 45 – 55 (pheno / micropheno) | 53 – 64 (pheno / micropheno) | | 90 - 94 (pheno / micropheno) |
| Microcrystal (vol.%) | Not quantified | Not quantified | | Not quantified |

Table 2. Micro vesicle and crystal shape and size characteristics of every Uig layer and pumice type

Yellow-White Foamy Pumice (YWFP)

| | Vesicles | | | | Crystals | | | |
|---|---|---|---|---|---|---|---|---|
| | *Modal Shape (ShpF)* | *Modal size (μm^3)* | *Shape Distribution (kurtosis + symmetry)* | *Size Distribution (kurtosis + symmetry)* | *Modal Shape (ShpF)* | *Modal size (μm^3)* | *Shape Distribution (kurtosis + symmetry)* | *Size Distribution (kurtosis + symmetry)* |
| Uig8 | Spherical & tubular | 10^1 – 10^4, & 2ND 10^6 – 10^7 | Bimodal | Bimodal & platykurtic | | | | |
| Uig7 | Subspherical | 10^3 – 10^4 | Mesokurtic & leptokurtic | Mesokurtic & leptokurtic | | | | |
| Uig6 | Not Present | | | | Constant modal blade-like tabular | 10^5 – 10^6 | Negatively skewed or symmetrical leptokurtic & mesokurtic | Negatively skewed or symmetrical leptokurtic & mesokurtic |
| Uig5 | Upwards from subspherical to wide range of vesicle shapes | Upwards from 10^5 to 10^3 – 10^4 | Positively skewed, mesokurtic to platykurtic | Negatively skewed, bimodal to multimodal | | | | |
| Uig4 | | | | | | | | |
| Uig3 | Not Present | | | | | | | |
| Uig2 | | | | | | | | |
| Uig1 | | | | | | | | |
| Gral. | 10^3 – 10^4 μm^3 modal vesicles. Largest fractions of spherical vesicles (29 vol.%) | | | | >10^5 μm^3 modal crystals. > 40 vol.% euhedral tabular | | | |

ShpF = SA^3 / 36π *V*^2 (Appendix B.1b). 2ND: secondary mode.

Table 2 continues

| Yellow-White Crystalline Pumice (YWCP) | | | | | | | | |
|---|---|---|---|---|---|---|---|---|
| | Vesicles | | | | Crystals | | | |
| | *Modal Shape (ShpF)* | *Modal size (µm^3)* | *Shape Distribution (kurtosis + symmetry)* | *Size Distribution (kurtosis + symmetry)* | *Modal Shape (ShpF)* | *Modal size (µm^3)* | *Shape Distribution (kurtosis + symmetry)* | *Size Distribution (kurtosis + symmetry)* |
| Uig8 | Spherical & coalesced | 10^1 – 10^4 plateau, & 2ND 10^6 | Bimodal | Bimodal & platykurtic | Cuboid & tabular | 10^3 – 10^5 | | |
| Uig7 | From subspherical to predominant spherical | Decrease towards ± 10^3 | Leptokurtic | Leptokurtic | Cuboid | 10^3, and secondary 10^5 | From unimodal platykurtic to mesokurtic | From unimodal leptokurtic to multimodal platykurtic |
| Uig6<br>Uig5 | Subspherical | Upwards from 10^5 & 2ND 10^3 & 10^7, to 10^4 | Bimodal to unimodal | Negatively skewed, multimodal to unimodal | Tabular and rod-like acicular | 10^3 – 10^5, & 2ND 10^5 – 10^7 | | |
| Uig4 | Not Present | | | | | | | |
| Uig3<br>Uig2<br>Uig1 | Not Present | | | | | | | |
| Gral. | 10^2 – 10^4 µm^3 subspherical to spherical vesicles. Coalesced vesicles (4 - 8 vol.%). Numerous 10^0 – 10^2 µm^3 vesicles (5 - 10 vol.%) | | | | Subhedral to anhedral 10^3 – 10^5 µm^3 modal crystals. Equant (20 – 30 vol.%) & cuboid (30 – 35 vol.%), plus few rod-like acicular | | | |

Table 2 continues

| Grey Crystalline Pumice (GCP) | | | | | | | | |
|---|---|---|---|---|---|---|---|---|
| | Vesicles | | | | Crystals | | | |
| | *Modal Shape (ShpF)* | *Modal size (µm^3)* | *Shape Distribution (kurtosis + symmetry)* | *Size Distribution (kurtosis + symmetry)* | *Modal Shape (ShpF)* | *Modal size (µm^3)* | *Shape Distribution (kurtosis + symmetry)* | *Size Distribution (kurtosis + symmetry)* |
| Uig8 | Spherical to ellipsoidal | 10^4 – 10^5 & 2ND 10^6 - 10^7 | Platykurtic | Bimodal | From equant to plate-like tabular | 10^4, & 2ND 10^5 - 10^7 | | |
| Uig7 | Subspherical to spherical from base to top level | ± 10^4 | Leptokurtic to Positively skewed & mesokurtic | Leptokurtic | From Uig5 to Uig7: blade-like tabular, through to cuboid & tabular, to cuboid at Uig7-top | From Uig5 to Uig7: decrease from 10^6, through to 10^5 - 10^6, to 10^3 - 10^4, & 2ND 10^4 - 10^6. Size fixes to 10^4 at Uig7 top | Leptokurtic to platykurtic | From bimodal to multimodal |
| Uig6 | Not Present | | | | | | | |
| Uig5 | Subspherical to mostly spherical from base to top level | ± 10^5 | Positively skewed leptokurtic to mesokurtic from base to top level | Negatively skewed to symmetrical from base to top level | | | | |
| Uig4 | Not Present | | | | | | | |
| Uig3 | Not Present | | | | | | | |
| Uig2 | | | | | | | | |
| Uig1 | | | | | | | | |
| Gral. | 10^4 – 10^5 µm^3 subspherical to spherical vesicles. Coalesced and ellipsoidal vesicles (4 - 8 vol.%). Numerous 10^3 – 10^5 µm^3 vesicles (13 - 20 vol.%) | | | | Subhedral to anhedral 10^4 µm^3 modal crystals. Equant (20 – 30 vol.%), cuboid (30 – 35 vol.%) & tabular (35 vol.%) | | | |

Table 2 continues

| Grey Banded Pumice (GBP) | | | | | | | | |
|---|---|---|---|---|---|---|---|---|
| B1 | | | | | | | | |
| | Vesicles | | | | Crystals | | | |
| | *Modal Shape (ShpF)* | *Modal size (µm^3)* | *Shape Distribution (kurtosis + symmetry)* | *Size Distribution (kurtosis + symmetry)* | *Modal Shape (ShpF)* | *Modal size (µm^3)* | *Shape Distribution (kurtosis + symmetry)* | *Size Distribution (kurtosis + symmetry)* |
| Uig8 | Spherical & 2ND fibrous | 10^2 – 10^3, & 2ND 10^6 | Bimodal | Bimodal & platykurtic | Blade-like tabular & 2ND cuboid | 10^6 | Bimodal | Skewed unimodal |
| Uig7 | Subspherical | ± 10^3 | Leptokurtic | Leptokurtic | Shift back into cuboid & 2ND blade-like tabular | Increases from 10^4 to 10^5 - 10^6 | Bimodal | Bimodal |
| Uig6 | | | | | | | | |
| Uig5 | From spherical, through to subspherical, to spanning the complete range from spherical to ellipsoidal | Upwards from 10^5 to 10^6, & 2ND 10^7 | From positively skewed mesokurtic to platykurtic | From negatively skewed, unimodal to multimodal, through to normal, to negatively skewed & platykurtic | From cuboid, through to ranging equant to blade-like tabular, to spanning tabular to rod-like acicular | Constant 10^4 – 10^5 | Unimodal to bimodal mesokurtic & platykurtic | Unimodal to bimodal mesokurtic & platykurtic |
| Uig4 | | | | | | | | |
| Uig3 | | | | | | | | |
| Uig2 | Not Present | | | | | | | |
| Uig1 | | | | | | | | |
| Gral. | 10^3 – 10^5 µm^3 subspherical to spherical vesicles. Vesicles are nearly identical to YWCP. | | | | Modal 10^5 µm^3 crystals having all YWCP-like textures plus GCP-like high cuboid crystal fractions (up to 50 vol.%) | | | |

Table 2 continues

| Grey Banded Pumice (GBP) | | | | | | | | |
|---|---|---|---|---|---|---|---|---|
| B2 | | | | | | | | |
| | Vesicles | | | | Crystals | | | |
| | *Modal Shape (ShpF)* | *Modal size (µm^3)* | *Shape Distribution (kurtosis + symmetry)* | *Size Distribution (kurtosis + symmetry)* | *Modal Shape (ShpF)* | *Modal size (µm^3)* | *Shape Distribution (kurtosis + symmetry)* | *Size Distribution (kurtosis + symmetry)* |
| Uig8 | Largest are tubular. Other spherical & 2ND coalesced | Largest > 10^6. Rest: 10^2 – 10^3, & 2ND 10^6 | Largest leptokurtic. Rest bimodal | Largest leptokurtic. Rest: bimodal | | | | |
| Uig7 | Largest are tubular. Other subspherical | Largest > 10^6. Rest: decrease from 10^4 to 10^3 – 10^4 | All leptokurtic | All leptokurtic | Cuboid & 2ND tabular | 10^5 - 10^6, & 2ND 10^3 - 10^5 | From negatively skewed & symmetrical, mesokurtic & leptokurtic, to bimodal & multimodal with frequent leptokurtic modes | From negatively skewed & symmetrical, mesokurtic & leptokurtic, to bimodal & multimodal with frequent leptokurtic modes |
| Uig6<br>Uig5<br>Uig4 | Largest are tubular. The rest shift upwards from subspherical, through to ranging from spherical to coalesced, to ellipsoidal, & last spherical in Uig6 | Largest > 10^6. Rest fluctuates between 10^5 – 10^6, & shift down to 10^4 in Uig6 | Largest extremely leptokurtic. Rest: positively & negatively skewed, platykurtic or symmetrical | Largest extremely leptokurtic. Rest: negatively skewed mesokurtic | Plate-like & blade-like tabular, & 2ND cuboid | | | |
| Uig3<br>Uig2<br>Uig1 | Not Present | | | | | | | |
| Gral. | Two vesicle populations. Largest > 10^5 µm^3 (30 - 70 vol.%) fibrous tubular vesicles (60 vol.%). The rest 10^3 – 10^4 µm^3 spherical to subspherical | | | | Subhedral to euhedral 10^4 – 10^5 µm^3 modal crystals. Cuboid (up to 80 vol.%), tabular (± 40 vol.%) & rod-like acicular (10 vol.%) | | | |

Table 2 continues

| Violet Crystalline Pumice (VCP) | | | | | | | | |
|---|---|---|---|---|---|---|---|---|
| | Vesicles | | | | Crystals | | | |
| | *Modal Shape (ShpF)* | *Modal size (µm^3)* | *Shape Distribution (kurtosis + symmetry)* | *Size Distribution (kurtosis + symmetry)* | *Modal Shape (ShpF)* | *Modal size (µm^3)* | *Shape Distribution (kurtosis + symmetry)* | *Size Distribution (kurtosis + symmetry)* |
| Uig8 | Spherical & complex | 10^1 – 10^3, & 2ND 10^6 | Bimodal & platykurtic | Bimodal & platykurtic | Become modal equant | 10^2 - 10^3 | Platykurtic to Multimodal | Multimodal |
| Uig7 | From base to top level, shift from ellipsoidal & complex shapes to modal tubular | ± 10^4 | From unimodal platykurtic or leptokurtic to normal | From unimodal platykurtic or leptokurtic to normal | Back to blade-like tabular, & 2ND equant plus radiating & shapeless aggregates | 10^3, & 2ND 10^5 - 10^7 | Bimodal & multimodal | Bimodal & multimodal |
| Uig6 | Not Present | | | | Not Present | | | |
| Uig5 | Modal tubular & complex & 2ND spherical | Increases from 10^4 to 10^5 | Negatively skewed & bimodal | Unimodal to bimodal | Cuboid to rod-like acicular | 10^3 - 10^4, & 2ND 10^6 | From unimodal, symmetrical or skewed leptokurtic to platykurtic, to bimodal | From unimodal, symmetrical or skewed leptokurtic to platykurtic, to bimodal |
| Uig4 | | | | | From blade-like tabular to progressive modal equant | Decrease from 10^5 - 10^6 to 10^3 - 10^4 | | |
| Uig3<br>Uig2<br>Uig1 | Spherical to increasingly fibrous tubular | ± 10^3 | Positively skewed, bimodal | Negatively skewed to symmetrical mesokurtic & leptokurtic | | | | |
| Gral. | 10^3 – 10^4 µm^3 spherical, tubular and complex vesicles. Numerous 10^0 – 10^1 µm^3 vesicles. Complex 3D clusters of irregularly contorted vesicles (18 vol.%) | | | | Subhedral to anhedral 10^3 – 10^4 µm^3 modal crystals. Highest acicular crystal fractions (up to 40 vol.%) & aggregates of radiating habits | | | |

Table 3. Microtextural parameters and rates calculated for every Uig layer and pumice type

| | Sample | Ground mass | Vesicles | | | | Total Crystals | | | Microlites | | |
|---|---|---|---|---|---|---|---|---|---|---|---|---|
| | Volume $x10^{..}$ mm^3 | Volume $x10^{..}$ mm^3 | Volume $x10^{..}$ mm^3 | $V_N$ | *VND* $x10^{..}$ mm^-3 | dP/dt Het σ MPa s^-1 | Volume $x10^{..}$ mm^3 | $C_N$ | *CND* $x10^{..}$ mm^-3 | $M_N$ | *MND* $x10^{..}$ mm^-3 | dP/dt Plg-Px MPa s^-1 |
| YWFP | | | | | | | | | | | | |
| Uig8 | 1.3 (-1) | 2.3 (-2) | 7.3 (-2) | 20871 | 8.9 (5) | 5.9 | 2.8 (-2) | 6947 | 3.0 (5) | 4530 | 1.9 (5) | 0.35 |
| Uig7t | 1.2 (-1) | 2.1 (-2) | 7.4 (-2) | 27826 | 1.3 (6) | 7.6 | 2.2 (-2) | 4572 | 2.2 (5) | 2397 | 1.1 (5) | 0.25 |
| Uig7b | 1.2 (-1) | 1.9 (-2) | 7.0 (-2) | 25991 | 1.3 (6) | 7.7 | 2.6 (-2) | 6711 | 3.5 (5) | 4705 | 2.4 (5) | 0.41 |
| Uig6 | - | - | - | - | - | - | - | - | - | - | - | - |
| Uig5t | - | - | - | - | - | - | - | - | - | - | - | - |
| Uig5b | 1.1 (-1) | 1.9 (-2) | 7.3 (-2) | 28171 | 1.5 (6) | 8.3 | 2.1 (-2) | 5021 | 2.7 (5) | 3087 | 1.7 (5) | 0.32 |
| Uig4 | 1.3 (-1) | 3.2 (-2) | 7.7 (-2) | 35601 | 1.1 (6) | 6.8 | 2.2 (-2) | 3320 | 1.0 (5) | Not identified | | |
| YWCP | | | | | | | | | | | | |
| Uig8 | 9.1 (-2) | 1.7 (-2) | 5.0 (-2) | 17115 | 1.0 (6) | 1.2 | 2.4 (-2) | 42601 | 2.5 (6) | 37578 | 2.2 (6) | 1.79 |
| Uig7t | 9.1 (-2) | 1.2 (-2) | 5.5 (-2) | 29202 | 2.5 (6) | 2.2 | 2.4 (-2) | 40272 | 3.4 (6) | 37700 | 3.2 (6) | 2.27 |
| Uig7b | 8.3 (-2) | 1.3 (-2) | 4.4 (-2) | 22331 | 1.7 (6) | 1.7 | 2.6 (-2) | 46823 | 3.7 (6) | 42394 | 3.3 (6) | 2.33 |
| Uig6 | 8.5 (-2) | 1.2 (-2) | 4.8 (-2) | 16546 | 1.3 (6) | 1.5 | 2.5 (-2) | 42877 | 3.5 (6) | 39568 | 3.2 (6) | 2.28 |
| Uig5t | 7.2 (-2) | 1.0 (-2) | 4.2 (-2) | 9839 | 9.7 (5) | 1.2 | 2.0 (-2) | 18024 | 1.8 (6) | 15312 | 1.5 (6) | 1.38 |
| GCP | | | | | | | | | | | | |
| Uig8 | 2.6 (-1) | 4.8 (-2) | 1.3 (-1) | 9957 | 2.1 (5) | 0.5 | 7.8 (-2) | 48370 | 1.0 (6) | 34061 | 7.1 (5) | 0.18 |
| Uig7t | 2.2 (-1) | 4.6 (-2) | 1.0 (-1) | 12397 | 2.7 (5) | 0.6 | 7.0 (-2) | 45010 | 9.9 (5) | 35110 | 7.7 (5) | 0.19 |
| Uig7b | 2.5 (-1) | 7.9 (-2) | 1.0 (-1) | 40397 | 5.1 (5) | 0.9 | 7.0 (-2) | 79010 | 9.9 (5) | 51528 | 6.5 (5) | 0.17 |
| Uig6 | - | - | - | - | - | - | - | - | - | - | - | - |
| Uig5t | 2.0 (-1) | 3.0 (-2) | 9.9 (-2) | 15171 | 5.0 (5) | 0.9 | 7.2 (-2) | 46332 | 1.5 (6) | 38198 | 1.3 (6) | 0.26 |
| Uig5b | 2.3 (-1) | 3.9 (-2) | 1.1 (-1) | 7026 | 1.8 (5) | 0.5 | 7.5 (-2) | 38251 | 9.8 (5) | 27782 | 7.1 (5) | 0.18 |
| GBP - B1 | | | | | | | | | | | | |
| Uig8 | 2.0 (-3) | 1.9 (-4) | 9.6 (-4) | 227 | 1.2 (6) | 1.5 | 8.2 (-4) | 1021 | 5.4 (6) | 964 | 5.1 (6) | 0.67 |
| Uig7t | 2.6 (-3) | 5.4 (-4) | 1.4 (-3) | 871 | 1.6 (6) | 1.8 | 7.2 (-4) | 1566 | 2.9 (6) | 1448 | 2.7 (6) | 0.43 |
| Uig7b | 2.4 (-3) | 4.2 (-4) | 1.2 (-3) | 509 | 1.2 (6) | 1.5 | 7.2 (-4) | 1350 | 3.2 (6) | 1205 | 2.9 (6) | 0.46 |
| Uig6 | 2.0 (-3) | 4.2 (-4) | 9.8 (-4) | 363 | 8.7 (5) | 1.2 | 5.7 (-4) | 604 | 1.4 (6) | 492 | 1.2 (6) | 0.25 |
| Uig5t | 1.8 (-3) | 2.9 (-4) | 9.6 (-4) | 249 | 8.6 (5) | 1.2 | 5.3 (-4) | 401 | 1.4 (6) | 323 | 1.1 (6) | 0.24 |
| Uig5b | 2.4 (-3) | 3.6 (-4) | 1.3 (-3) | 286 | 7.8 (5) | 1.1 | 6.8 (-4) | 617 | 1.7 (6) | 519 | 1.4 (6) | 0.29 |
| Uig4 | 1.6 (-3) | 3.2 (-4) | 8.8 (-4) | 244 | 7.7 (5) | 1.1 | 4.5 (-4) | 557 | 1.8 (6) | 524 | 1.7 (6) | 0.32 |
| GBP - B2 | | | | | | | | | | | | |
| Uig8 | 1.0 (-3) | 2.1 (-4) | 6.0 (-4) | 218 | 1.0 (6) | 6.5 | 2.0 (-4) | 97 | 4.6 (5) | 34 | 1.6 (5) | 0.31 |
| Uig7t | 1.0 (-3) | 2.4 (-4) | 6.4 (-4) | 314 | 1.3 (6) | 7.5 | 1.4 (-4) | 156 | 6.4 (5) | 103 | 4.2 (5) | 0.59 |
| Uig7b | 9.5 (-4) | 2.0 (-4) | 6.0 (-4) | 238 | 1.2 (6) | 7.1 | 1.5 (-4) | 131 | 6.5 (5) | 61 | 3.0 (5) | 0.47 |
| Uig6 | 1.1 (-3) | 2.3 (-4) | 6.8 (-4) | 335 | 1.5 (6) | 8.2 | 2.3 (-4) | 119 | 5.3 (5) | 59 | 2.6 (5) | 0.43 |
| Uig5t | 9.7 (-4) | 2.0 (-4) | 5.9 (-4) | 211 | 1.1 (6) | 6.6 | 1.8 (-4) | 97 | 4.9 (5) | 44 | 2.2 (5) | 0.38 |
| Uig5b | 1.4 (-3) | 2.7 (-4) | 8.6 (-4) | 287 | 1.1 (6) | 6.6 | 3.1 (-4) | 93 | 3.5 (5) | 21 | 8.0 (4) | 0.20 |
| Uig4 | 1.3 (-3) | 2.1 (-4) | 8.2 (-4) | 269 | 1.3 (6) | 7.5 | 2.7 (-4) | 61 | 2.9 (5) | 39 | 1.9 (5) | 0.34 |

Table 3 continues

| | Sample | Ground mass | Vesicles | | | | Total Crystals | | | Microlites | | |
|---|---|---|---|---|---|---|---|---|---|---|---|---|
| | Volume *x*10^(..) mm^3 | Volume *x*10^(..) mm^3 | Volume *x*10^(..) mm^3 | $V_N$ | *VND* *x*10^(..) mm^-3 | dP/dt Het σ MPa s^-1 | Volume *x*10^(..) mm^3 | $C_N$ | *CND* *x*10^(..) mm^-3 | $M_N$ | *MND* *x*10^(..) mm^-3 | dP/dt Plg-Px MPa s^-1 |
| | | | | | | VCP | | | | | | |
| Uig8 | 1.3 (-1) | 3.5 (-2) | 2.4 (-2) | 9886 | 2.8 (5) | 0.6 | 7.3 (-2) | 75115 | 2.1 (6) | 64719 | 1.8 (6) | 0.34 |
| Uig7t | 1.4 (-1) | 3.2 (-2) | 2.7 (-2) | 13080 | 4.0 (5) | 0.8 | 7.7 (-2) | 77907 | 2.4 (6) | 70880 | 2.2 (6) | 0.38 |
| Uig7b | 1.2 (-1) | 2.9 (-2) | 2.0 (-2) | 16110 | 5.5 (5) | 1.0 | 7.0 (-2) | 72809 | 2.5 (6) | 62627 | 2.1 (6) | 0.37 |
| Uig6 | - | - | - | - | - | - | - | - | - | - | - | - |
| Uig5t | 1.4 (-1) | 2.8 (-2) | 2.9 (-2) | 19572 | 6.9 (5) | 1.1 | 8.2 (-2) | 84120 | 3.0 (6) | 76512 | 2.7 (6) | 0.44 |
| Uig5b | - | - | - | - | - | - | - | - | - | - | - | - |
| Uig4 | 1.3 (-1) | 3.1 (-2) | 2.5 (-2) | 7703 | 2.5 (5) | 0.6 | 7.4 (-2) | 95010 | 3.1 (6) | 91795 | 3.0 (6) | 0.46 |
| Uig3 | 1.4 (-1) | 3.4 (-2) | 2.3 (-2) | 8092 | 2.4 (5) | 0.6 | 8.0 (-2) | 132094 | 3.9 (6) | 128579 | 3.8 (6) | 0.55 |
| Uig2 | 9.7 (-2) | 2.9 (-2) | 1.5 (-2) | 4803 | 1.6 (5) | 0.4 | 5.3 (-2) | 92980 | 3.2 (6) | 89955 | 3.1 (6) | 0.48 |
| Uig1 | 9.5 (-2) | 3.0 (-2) | 1.4 (-2) | 3201 | 1.1 (5) | 0.3 | 5.1 (-2) | 90337 | 3.0 (6) | 87237 | 2.9 (6) | 0.46 |

Numbers inside brackets correspond to powers of the corresponding volume and density estimates in scientific notation *x*10^(..)

$V_N$: Number of vesicles identified in every sample

*VND:* Vesicle Number Density corrected for vol.% groundmass, crystallinity and microcrystallinity

$C_N$: Number of crystals identified in every sample

*CND:* Crystal Number Density corrected for vol.% groundmass, vesicularity and microvesicularity.

$M_N$: Number of microlites identified in every sample. Estimated from 3D microtomographs, corrected with data from 2D photomicrographs, using shape and size discrimination sieves.

*MND:* Microlite Number Density calculated from $M_N$ and corrected using *CND*

dP/dt: Decompression rate calculated using either vesicle or microlite data

Het σ: dP/dt estimated using heterogeneous surface tension values

Plg-Px: dP/dt estimated using plagioclase and pyroxene microlite data

Uig5 and Uig7's "t" and "b" indicate top and bottom levels of the layer

Table 4. Uig's weighted average microtextural parameters and magma rates

| Wt. Avg. | *VND* | *VND* dP/dt | *MND* | *MND* dP/dt | *U* | MDR | Conduit Radius | Relative Strain R |
|---|---|---|---|---|---|---|---|---|
| | mm^-3 | MPa s^-1 | mm^-3 | MPa s^-1 | m s^-1 | Kg s^-1 | m | s^-1 |
| Uig8 | 8.6 *x* 10^5 | 3.1 | 1.6 *x* 10^6 | 0.8 | 0.10 | 6.0 *x* 10^7 | 11.8 | 0.0042 |
| Uig7t | 1.5 *x* 10^6 | 4.8 | 1.3 *x* 10^6 | 0.8 | 0.16 | 7.7 *x* 10^7 | 10.5 | 0.0080 |
| Uig7b | 1.3 *x* 10^6 | 4.7 | 1.4 *x* 10^6 | 0.8 | 0.16 | *7.6 *x* 10^7 | 10.5 | 0.0074 |
| Uig6 | 5.2 *x* 10^5 | 2.5 | 2.4 *x* 10^6 | 1.7 | 0.08 | 4.7 *x* 10^7 | 10.5 | 0.0040 |
| Uig5t | 4.8 *x* 10^5 | 1.9 | 1.3 *x* 10^6 | 0.7 | 0.06 | 4.1 *x* 10^7 | 10.5 | 0.0030 |
| Uig5b | 8.4 *x* 10^5 | 5.7 | 4.3 *x* 10^5 | 0.3 | 0.20 | 9.5 *x* 10^7 | 10.0 | 0.0100 |
| Uig4 | 6.8 *x* 10^5 | 5.0 | 1.6 *x* 10^6 | 0.4 | 0.17 | 7.6 *x* 10^7 | 9.1 | 0.0100 |
| Uig3 | 2.4 *x* 10^5 | 0.6 | 3.8 *x* 10^6 | 0.6 | 0.02 | 4.1 *x* 10^6 | 5.5 | 0.0017 |
| Uig2 | 1.6 *x* 10^5 | 0.4 | 3.1 *x* 10^6 | 0.5 | 0.01 | 1.4 *x* 10^6 | 3.5 | 0.0020 |
| Uig1 | 1.1 *x* 10^5 | 0.3 | 2.9 *x* 10^6 | 0.5 | 0.01 | 1.1 *x* 10^6 | 3.5 | 0.0015 |

Wt. Avg. calculations produced using vol.% of each pumice type at every Uig layer

*VND*: Vesicle Number Density; *MND*: Microlite Number Density

dP/dt: Decompression rate calculated from either *VND* or *MND* data

*U*: Magma ascent rate. MDR: Magma discharge rate.

Uig5 and Uig7's "t" and "b" indicate top and bottom levels of the layer

*Data from Torres-Orozco et al. (2017b)

Table 5. Amphibole geothermobarometry of magmas associated with the 3300 cal BP Upper Inglewood eruptive episode

| Comb | T °C [a] | SD | P MPa [b] | SD | $H_2O$ Amp wt% [d] | SD | $SiO_2$ melt wt% [e] | SD | $H_2O$ melt wt% [f] | SD | $H_2O$ sat wt% [g] | SD | QFM[h] | SD | NNO[h] | SD | HM[h] | SD |
|---|---|---|---|---|---|---|---|---|---|---|---|---|---|---|---|---|---|---|
| GP1 | 987 | 66 | 443 | 26 | 1.94 | 0.02 | 64.69 | 2.00 | 5.85 | 0.50 | 2.34 | 1.10 | -12.31 | 0.16 | -11.49 | 0.15 | -6.70 | 0.15 |
| GP2 | 734 | 61 | 69 [c] | 6 | 2.11 | 0.02 | 78.44 | 0.52 | ---- | ---- | ---- | ---- | -11.08 | 0.98 | -11.74 | 0.63 | -7.86 | 0.44 |
| GP3 | 932 | 36 | 460 | 30 | 1.94 | 0.02 | 65.26 | 3.50 | 6.51 | 1.30 | 5.06 | 2.40 | -12.31 | 0.49 | -11.54 | 0.43 | -6.77 | 0.42 |
| YW1A_BA | 1100 | 90 | 639 | 81 | 1.96 | 0.01 | 57.57 | 2.50 | 6.76 | 0.80 | 6.70 | 0.52 | -11.52 | 0.12 | -10.81 | 0.16 | -6.04 | 0.21 |
| YW1A | 1039 | 95 | 398 | 30 | 1.92 | 0.01 | 65.91 | 1.60 | 5.63 | 0.30 | 1.30 | 0.80 | -12.22 | 0.26 | -11.41 | 0.23 | -6.62 | 0.22 |
| YW1B | 1023 | 98 | 398 | 30 | 1.92 | 0.01 | 65.91 | 1.60 | 5.63 | 0.30 | 2.56 | 1.80 | -12.23 | 0.26 | -11.42 | 0.23 | -6.63 | 0.22 |
| YW1C | 1014 | 93 | 398 | 30 | 1.92 | 0.01 | 66.00 | 1.50 | 5.60 | 0.29 | 3.24 | 0.70 | -12.34 | 0.15 | -11.54 | 0.14 | -6.76 | 0.14 |
| YW2 | 933 | 25 | 495 | 46 | 1.94 | 0.02 | 64.17 | 4.20 | 6.90 | 1.40 | 4.58 | 2.20 | -12.25 | 0.45 | -11.47 | 0.40 | -6.69 | 0.39 |
| YW3A | 937 | 29 | 517 | 18 | 1.94 | 0.02 | 64.17 | 4.20 | 6.90 | 1.40 | 5.10 | 2.10 | -12.21 | 0.46 | -11.44 | 0.41 | -6.67 | 0.40 |
| YW3B_1 | 783 | 42 | 61 [c] | 2 | 2.12 | 0.01 | 78.75 | 0.11 | ---- | ---- | ---- | ---- | -9.84 | 0.52 | -10.95 | 0.34 | -7.30 | 0.25 |
| YW3B_2 | 706 | 76 | 83 [c] | 6 | 2.09 | 0.02 | 77.72 | 0.20 | ---- | ---- | ---- | ---- | -13.03 | 0.44 | -13.03 | 0.27 | -8.78 | 0.18 |

Combinations (Comb) of distinct amphibole + plagioclase + glass chemical compositions from electron microprobe data (Appendix C).

a. Average temperature calculated using selected amphibole-only, Si-in-hornblende, amphibole-plagioclase, liquid-only, and amphibole-liquid thermometers of Holland and Blundy (1994), Ridolfi et al. (2010), Ridolfi and Renzulli (2012, equations b and c), Mutch et al. (2016), and Putirka (2016).

b. Average pressure calculated using amphibole-only and Al-in-hornblende barometers of Larocque and Canil (2010), Ridolfi and Renzulli (2012, equations b and c), Mutch et al. (2016), and Putirka (2016, calibrated for Hammarstrom and Zen, 1996).

c. Pressure calculated using only the Al-in-hornblende barometer of Mutch et al. (2016) for low-pressure amphibole crystallization.

d. Average stoichiometric $H_2O$ content of amphibole analysis estimated from Yavuz and Doner (2017).

e. Average $SiO_2$ melt content estimated using the amphibole-only and amphibole-liquid models of Ridolfi and Renzulli (2012) and Putirka (2016), respectively.

f. Average $H_2O$ melt content estimated using the amphibole-only model of Ridolfi and Renzulli (2012).

g. Average liquid $H_2O$ content at saturation estimated using the amphibole-liquid model of Putirka (2016)

h. Average oxygen fugacity buffers (logfO2): QFM (Quartz-Fayalite-Magnetite), NNO (Nickel-Nickel Oxide), and HM (Hematite-Magnetite) from Fegley (2013) for P-T calibrations of Putirka (2016)

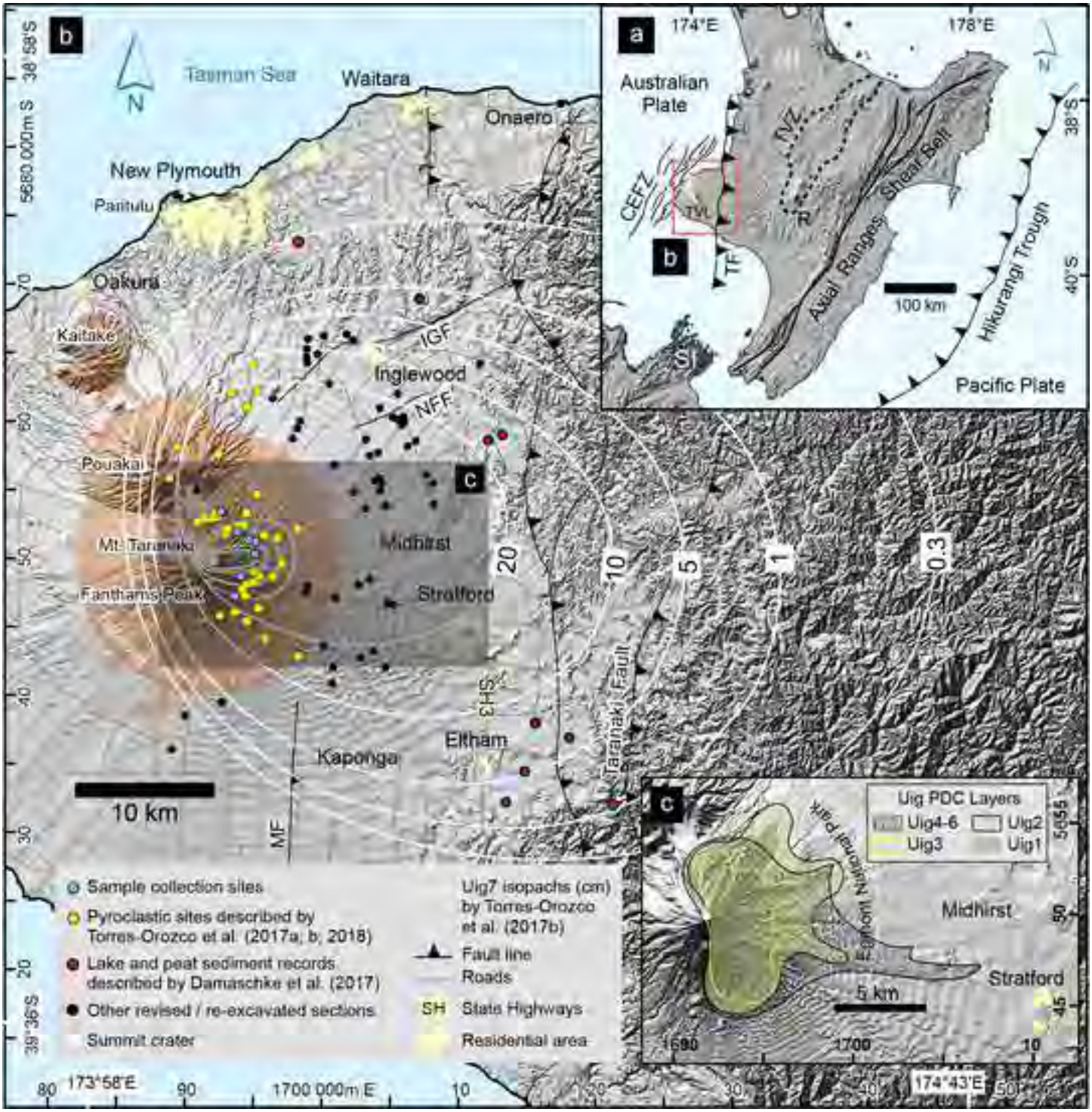
b
Tasman Sea
N
Waitara
Onaero
New Plymouth
Paritutu
Oakura
Kaitake
IGF
Inglewood
NFF
Pouakai
Mt Taranaki
Fanthams Peak
Midhirst
Stratford
SH3
Eltham
Kaponga
MF
10 km
Taranaki Fault
20
10
5
1
0.3
c
a
174°E
178°E
Australian Plate
Pacific Plate
CEFZ
TVL
TF
NVZ
Shear Belt
Axial Ranges
Hikurangi Trough
100 km
38°S
40°S
SI
Sample collection sites
Pyroclastic sites described by Torres-Orozco et al. (2017a, b, 2018)
Lake and peat sediment records described by Damaschke et al. (2017)
Other revised / re-excavated sections
Summit crater
Uig7 isopachs (cm) by Torres-Orozco et al. (2017b)
Fault line
Roads
SH State Highways
Residential area
Uig PDC Layers
Uig4-6
Uig2
Uig3
Uig1
Egmont National Park
Midhirst
Stratford
5 km
1690
1700
10
45
50
5655
39°36'S
173°58'E
1700 000m E
174°43'E

Figure 1

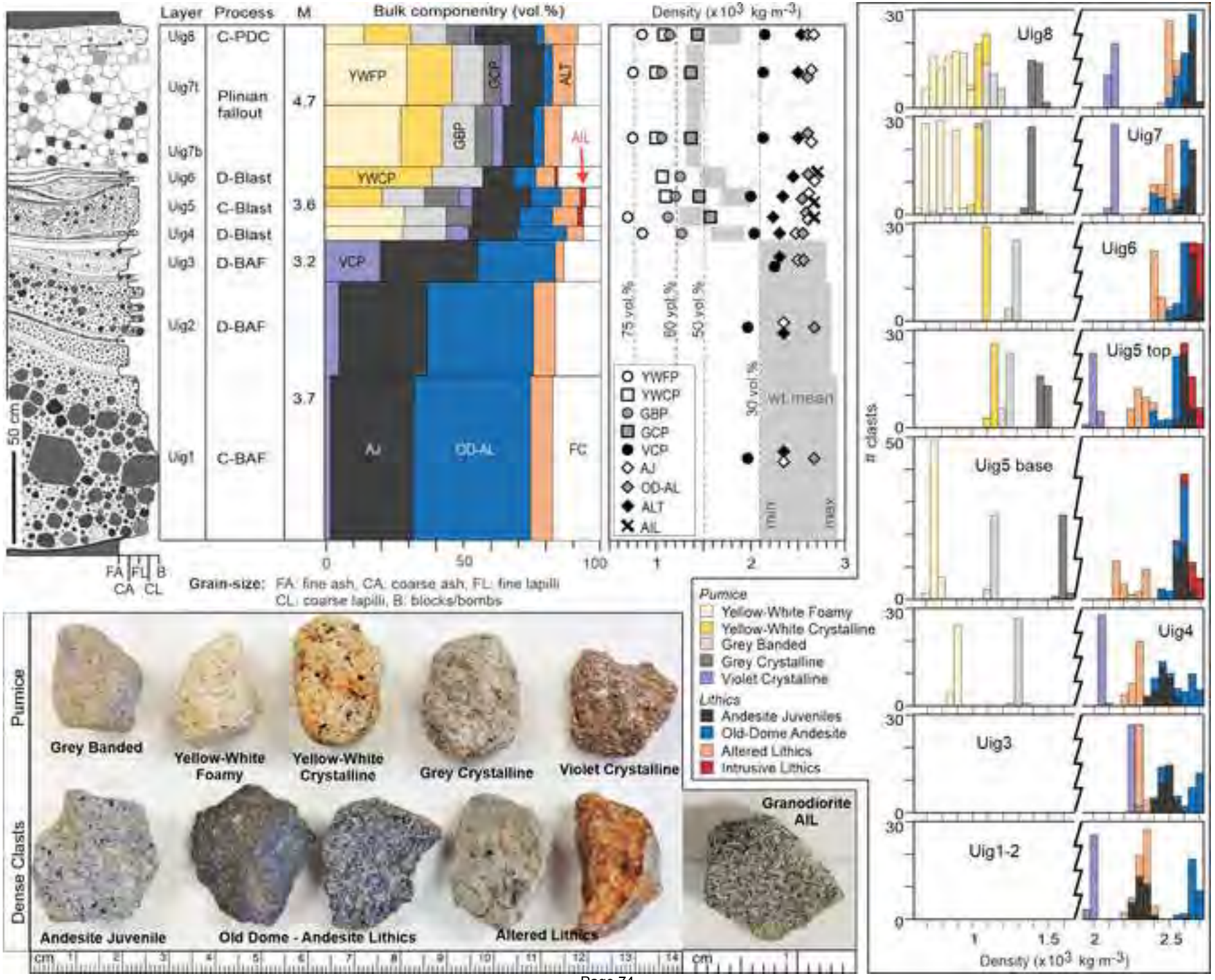
Layer
Process
M
Bulk componentry (vol.%)
Density (x10³ kg·m⁻³)
Ug8
C-PDC
Ug7t
Plinian fallout
4.7
Ug7b
Ug6
D-Blast
Ug5
C-Blast
3.6
Ug4
D-Blast
Ug3
D-BAF
3.2
Ug2
D-BAF
3.7
Ug1
C-BAF
YWFP
YWCP
GBP
GCP
VCP
AJ
OD-AL
ALT
AIL
FC
50 cm
FA
FL
B
CA
CL
Grain-size: FA: fine ash, CA: coarse ash, FL: fine lapilli
CL: coarse lapilli, B: blocks/bombs
75 vol.%
60 vol.%
50 vol.%
30 vol.%
wt.mean
main
max
# clasts
Ug8
Ug7
Ug6
Ug5 top
Ug5 base
Ug4
Ug3
Ug1-2
Density (x10³ kg·m⁻³)
Pumice
Yellow-White Foamy
Yellow-White Crystalline
Grey Banded
Grey Crystalline
Violet Crystalline
Lithics
Andesite Juveniles
Old-Dome Andesite
Altered Lithics
Intrusive Lithics
Pumice
Dense Clasts
Grey Banded
Yellow-White Foamy
Yellow-White Crystalline
Grey Crystalline
Violet Crystalline
Andesite Juvenile
Old Dome - Andesite Lithics
Altered Lithics
Granodiorite AIL
cm



Figure 2

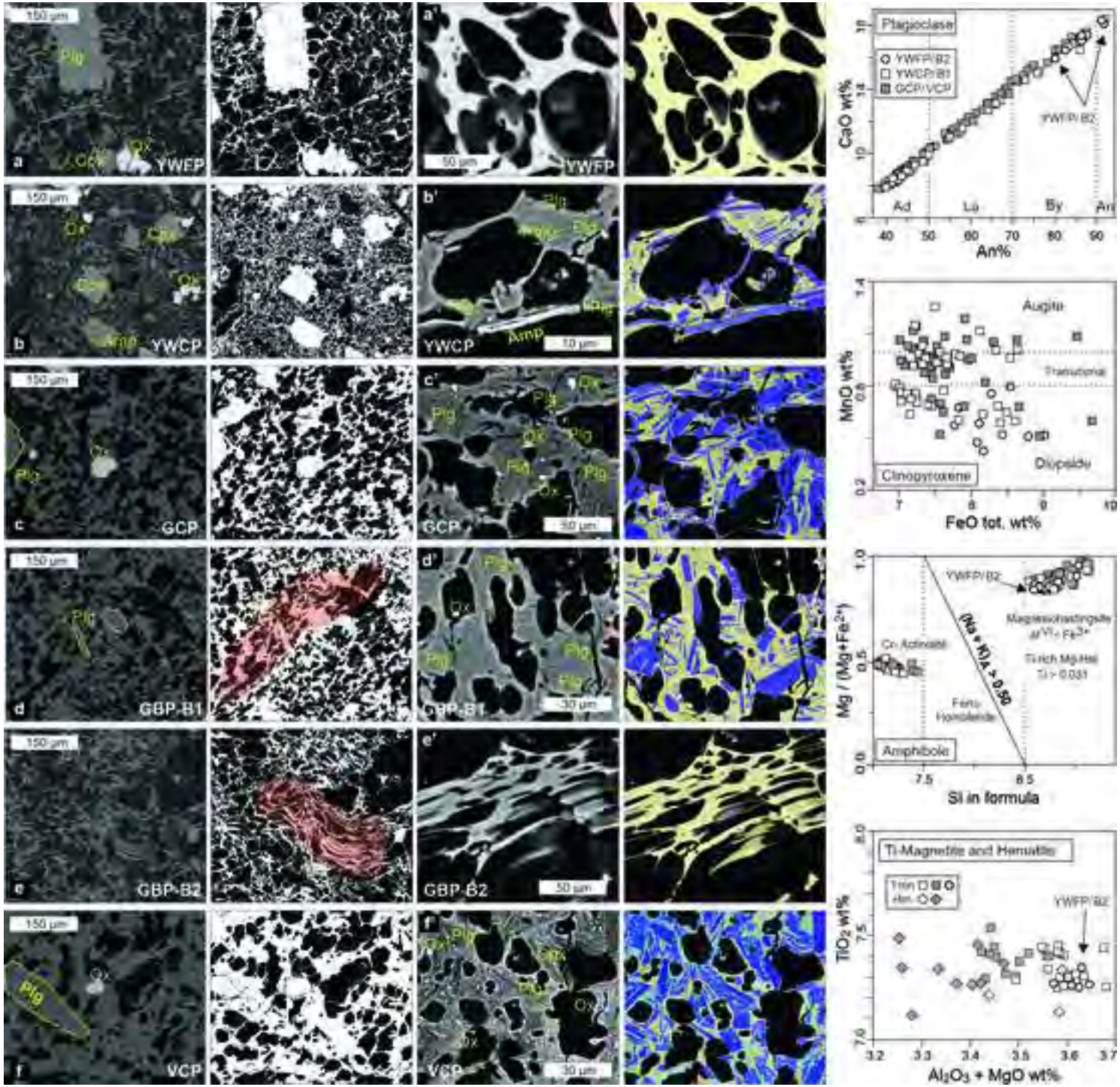
150 µm
Plg
Cpx
Ox
YWFP
50 µm
Amp
YWCP
GCP
GBP-B1
GBP-B2
VCP
30 µm
Plagioclase
YWFP/B2
YWCP/B1
GCP/VCP
CaO wt%
An%
Ab
La
By
An
Augite
Pigeonite
Diopside
Clinopyroxene
MnO wt%
FeO tot. wt%
Mg / (Mg+Fe2+)
Si in formula
Amphibole
Ti-Magnetite and Hematite
TiO2 wt%
Al2O3 + MgO wt%



Figure 3

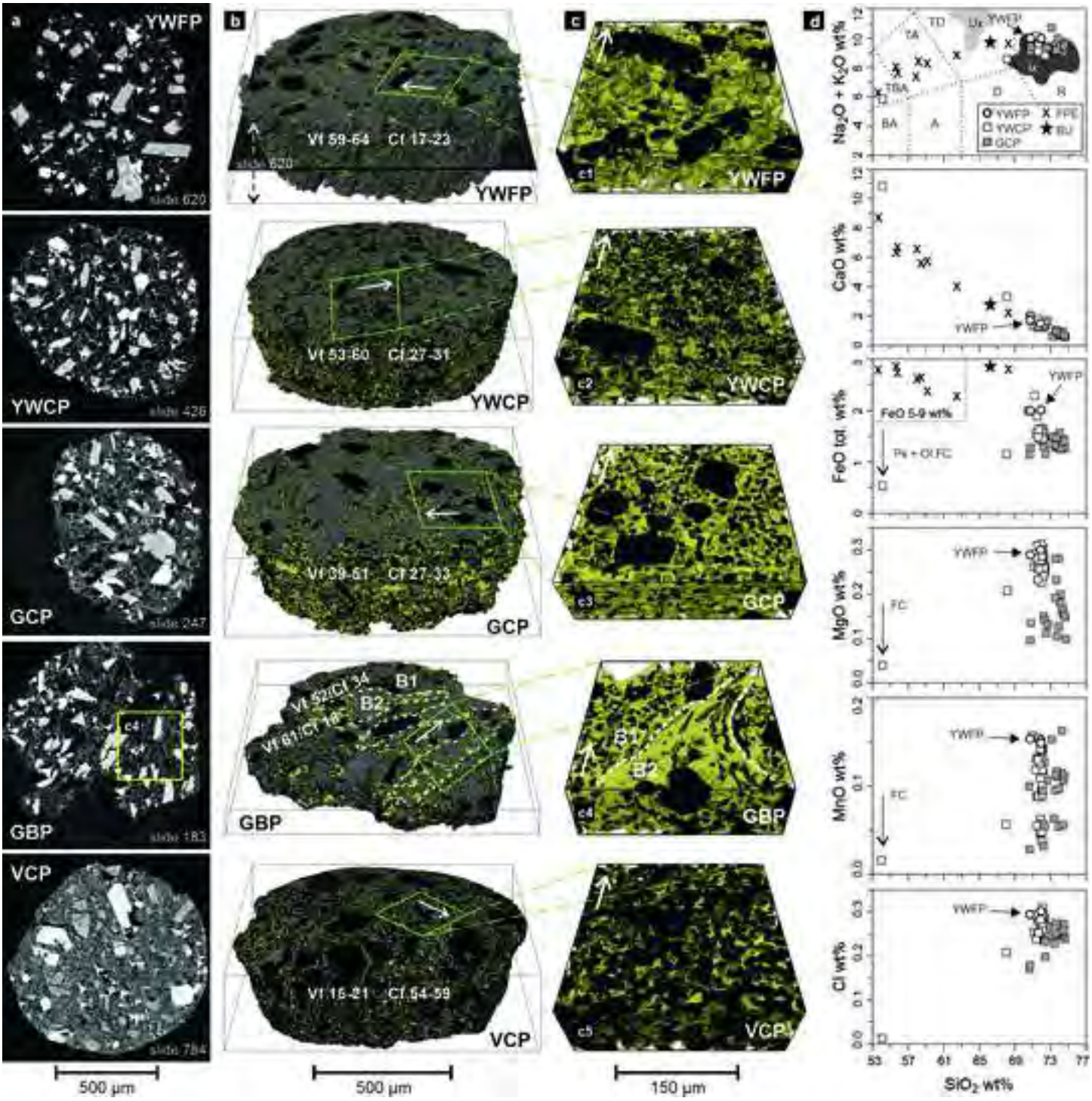
a
YWFP
slide 620
YWCP
slide 426
GCP
slide 247
GBP
slide 183
VCP
slide 784
500 µm
b
Vt 59-64 Cl 17-23
YWFP
Vt 53-60 Cl 27-31
YWCP
Vt 39-61 Cl 27-33
GCP
B1
B2
GBP
Vt 15-21 Cl 54-59
VCP
500 µm
c
c1
YWFP
c2
YWCP
c3
GCP
c4
GBP
c5
VCP
150 µm
d
TD
TA
TBA
BA
A
D
R
YWFP
FPE
YWCP
BU
GCP
Na2O + K2O wt%
CaO wt%
FeO tot wt%
FeO 5-9 wt%
Pl + Ol FC
MgO wt%
FC
MnO wt%
Cl wt%
SiO2 wt%

Figure 4

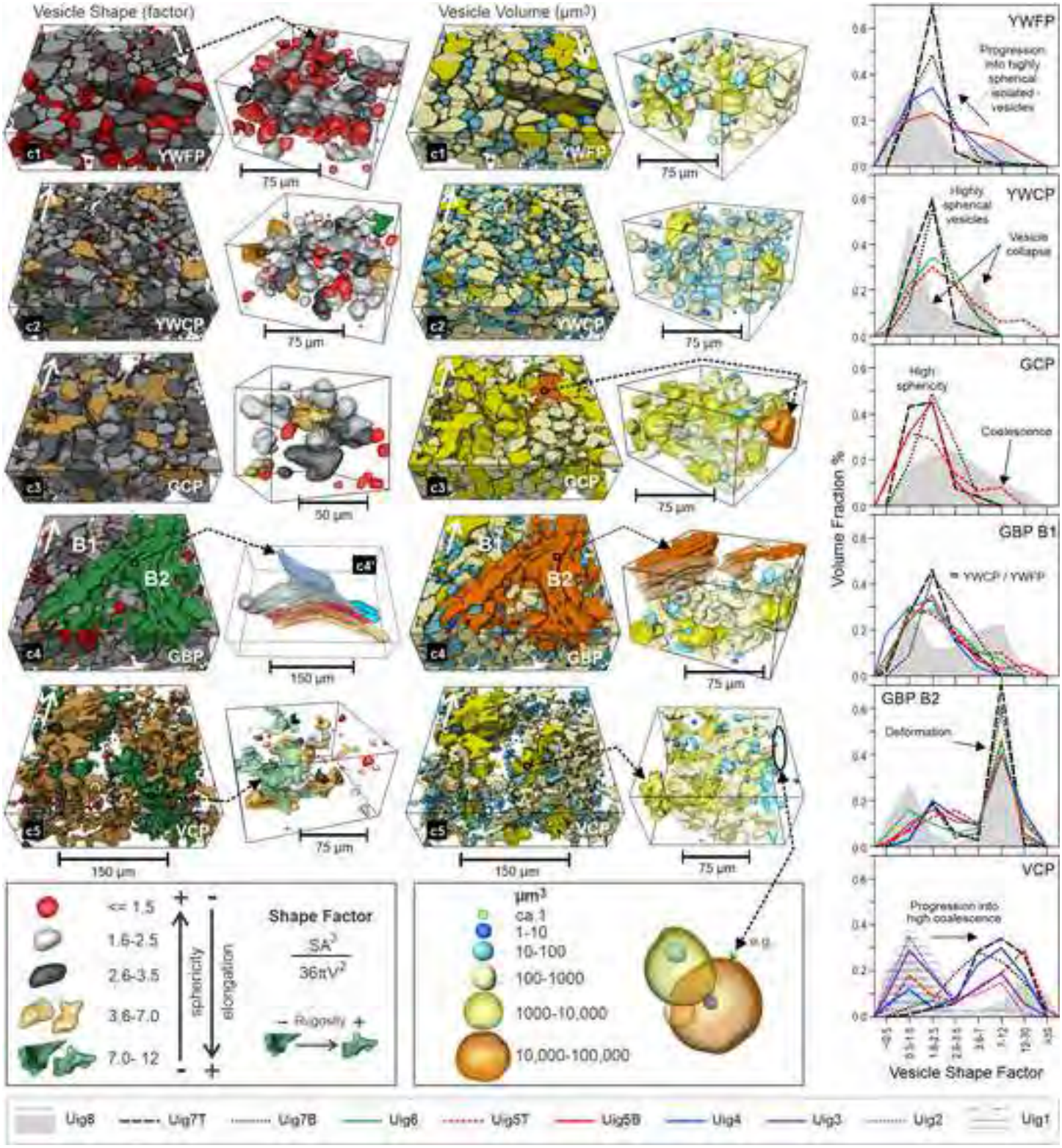
Vesicle Shape (factor)
Vesicle Volume (µm³)
c1
YWFP
c2
YWCP
c3
GCP
c4
B1
B2
GBP
c4'
c5
VCP
75 µm
50 µm
150 µm
<= 1.5
1.6-2.5
2.6-3.5
3.6-7.0
7.0- 12
sphericity
elongation
Shape Factor
SA³ / 36πV²
Rugosity
µm³
ca.1
1-10
10-100
100-1000
1000-10,000
10,000-100,000
YWFP
Progression into highly spherical isolated vesicles
YWCP
Highly spherical vesicles
Vesicle collapse
GCP
High sphericity
Coalescence
GBP B1
= YWCP / YWFP
GBP B2
Deformation
VCP
Progression into high coalescence
Volume Fraction %
Vesicle Shape Factor
Uig8
Uig7T
Uig7B
Uig6
Uig5T
Uig5B
Uig4
Uig3
Uig2
Uig1

Figure 5

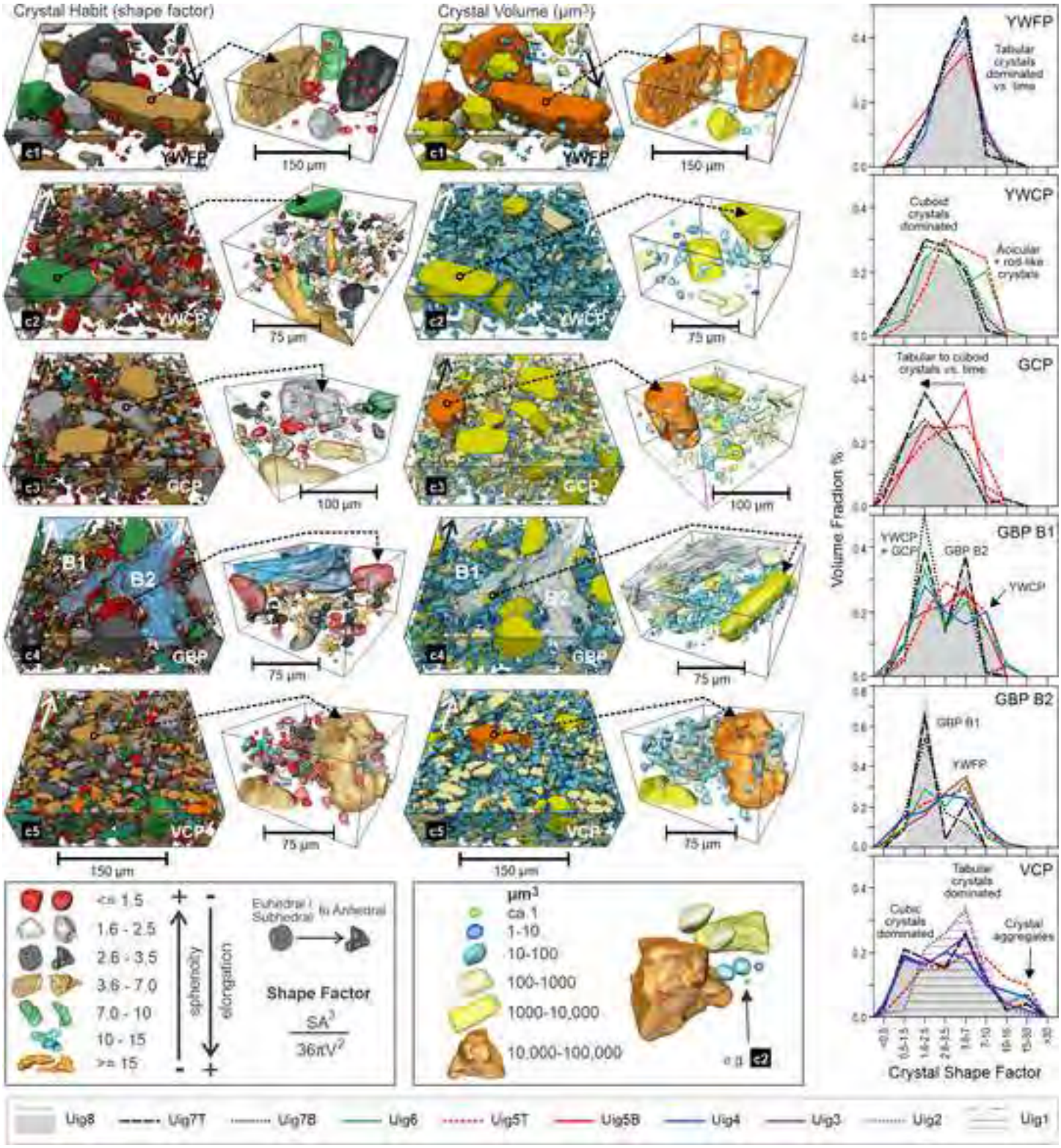
Crystal Habit (shape factor)
Crystal Volume (µm³)
c1
YWFP
c2
YWCP
c3
GCP
c4
B1
B2
GBP
c5
VCP4
150 µm
75 µm
100 µm
<= 1.5
1.6 - 2.5
2.6 - 3.5
3.6 - 7.0
7.0 - 10
10 - 15
>= 15
sphericity
elongation
Euhedral / Subhedral
to Anhedral
Shape Factor
SA³ / 36πV²
µm³
ca. 1
1-10
10-100
100-1000
1000-10,000
10,000-100,000
e.g. c2
YWFP
Tabular crystals dominated vs. time
YWCP
Cuboid crystals dominated
Acicular + rod-like crystals
GCP
Tabular to cuboid crystals vs. time
GBP B1
YWCP + GCP
GBP B2
YWCP
GBP B2
GBP B1
YWFP
VCP
Tabular crystals dominated
Cubic crystals dominated
Crystal aggregates
Volume Fraction %
Crystal Shape Factor
Uig8
Uig7T
Uig7B
Uig6
Uig5T
Uig5B
Uig4
Uig3
Uig2
Uig1

Figure 6

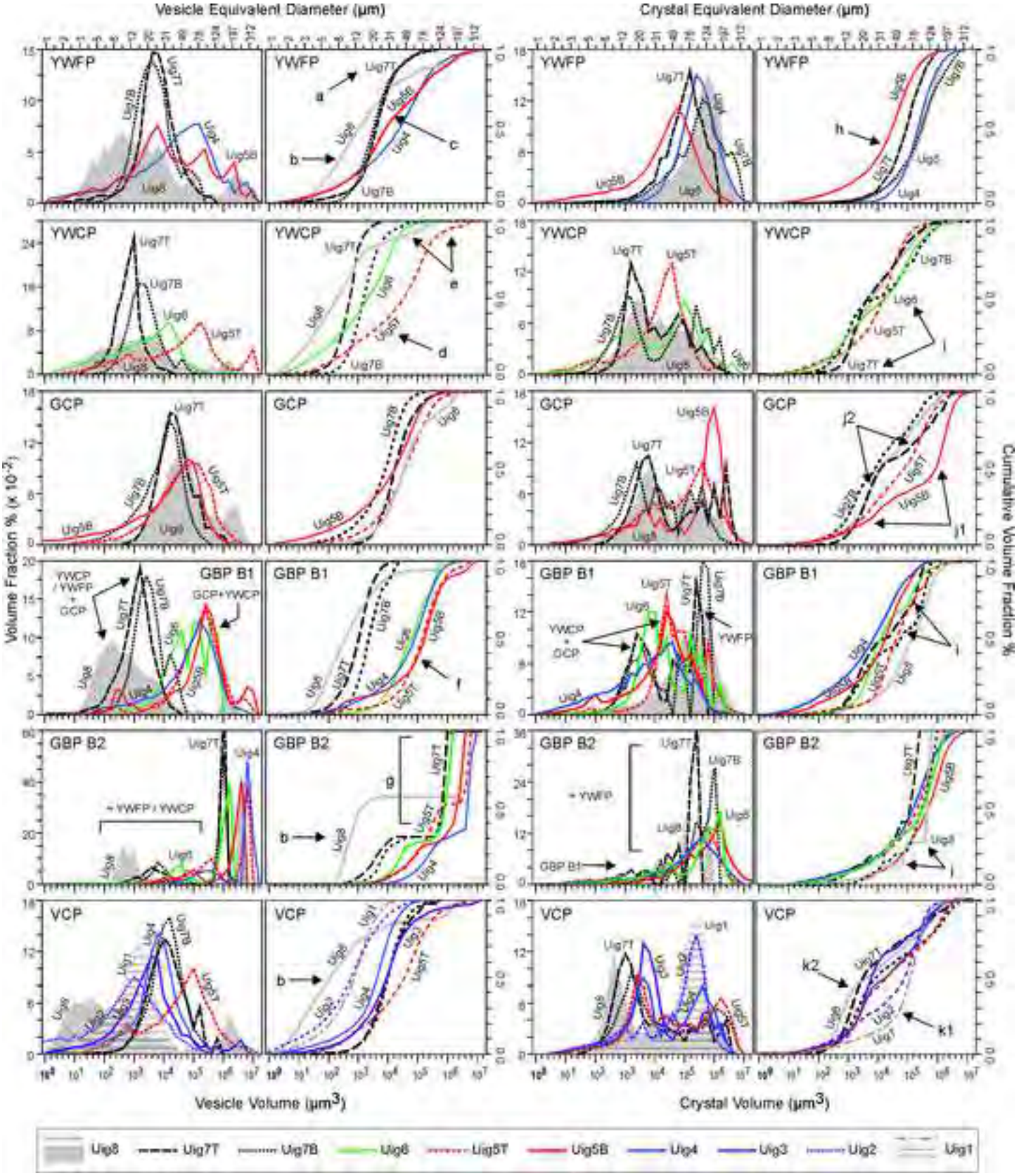
Vesicle Equivalent Diameter (μm)
Crystal Equivalent Diameter (μm)
YWFP
YWCP
GCP
GBP B1
GBP B2
VCP
Volume Fraction % (x 10-2)
Cumulative Volume Fraction %
Vesicle Volume (μm3)
Crystal Volume (μm3)
Ug8
Ug7T
Ug7B
Ug6
Ug5T
Ug5B
Ug4
Ug3
Ug2
Ug1

Figure 7

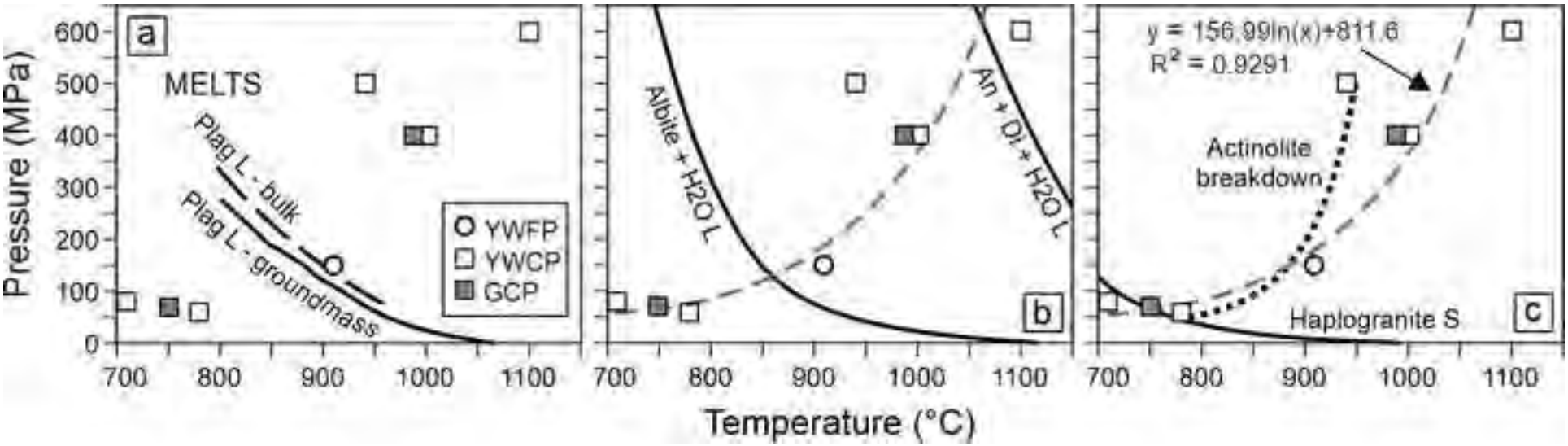
a
MELTS
Plag L - bulk
Plag L - groundmass
YWFP
YWCP
GCP
Pressure (MPa)
600
500
400
300
200
100
0
700
800
900
1000
1100
b
Albite + H2O L
An + Di + H2O L
c
y = 156.99ln(x)+811.6
R² = 0.9291
Actinolite
breakdown
Haplogranite S
Temperature (°C)

Figure 8

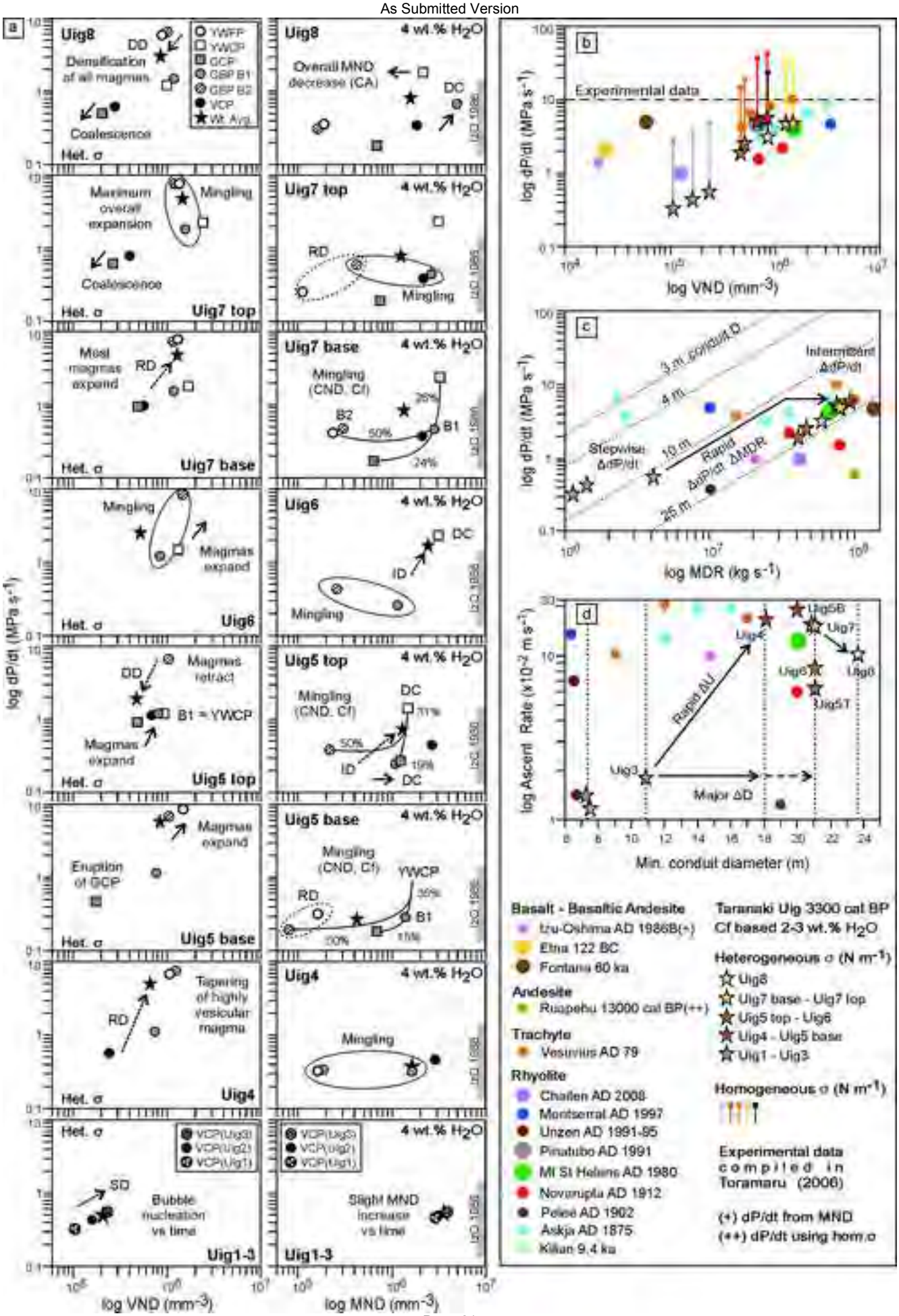
a
Uig8
DD
Densification of all magmas
Coalescence
Het. σ
YWFP
YWCP
GCP
GBP B1
GBP B2
VCP
Wt. Avg.
4 wt.% H2O
Overall MND decrease (CA)
DC
Maximum overall expansion
Mingling
Uig7 top
RD
Most magmas expand
Uig7 base
Mingling (CND, Cf)
B2
B1
50%
25%
24%
Magmas expand
Uig6
ID
Magmas retract
B1 ≈ YWCP
Uig5 top
77%
19%
Eruption of GCP
Uig5 base
YWCP
30%
15%
Tapering of highly vesicular magma
Uig4
SD
Bubble nucleation vs time
Uig1-3
VCP(Uig3)
VCP(Uig2)
VCP(Uig1)
Slight MND increase vs time
log dP/dt (MPa s-1)
log VND (mm-3)
log MND (mm-3)
b
Experimental data
log dP/dt (MPa s-1)
log VND (mm-3)
c
3 m, scrutut D
4 m
Intermittent ΔdP/dt
Stepwise ΔdP/dt
10 m
Rapid ΔdP/dt ΔMDR
25 m
log dP/dt (MPa s-1)
log MDR (kg s-1)
d
Uig5B
Uig7
Uig4
Uig6
Uig8
Uig5T
Uig3
Rapid ΔU
Major ΔD
log Ascent Rate (x10-2 m s-1)
Min. conduit diameter (m)
Basalt - Basaltic Andesite
Izu-Oshima AD 1986B(+)
Etna 122 BC
Fontana 60 ka
Andesite
Ruapehu 13000 cal BP(++)
Trachyte
Vesuvius AD 79
Rhyolite
Chaitén AD 2008
Montserrat AD 1997
Unzen AD 1991-95
Pinatubo AD 1991
Mt St Helens AD 1980
Novarupta AD 1912
Pelée AD 1902
Askja AD 1875
Kilian 9.4 ka
Taranaki Uig 3300 cal BP
Cf based 2-3 wt.% H2O
Heterogeneous σ (N m-1)
Uig8
Uig7 base - Uig7 top
Uig5 top - Uig6
Uig4 - Uig5 base
Uig1 - Uig3
Homogeneous σ (N m-1)
Experimental data compiled in Toramaru (2006)
(+) dP/dt from MND
(++) dP/dt using hom.σ



Figure 9

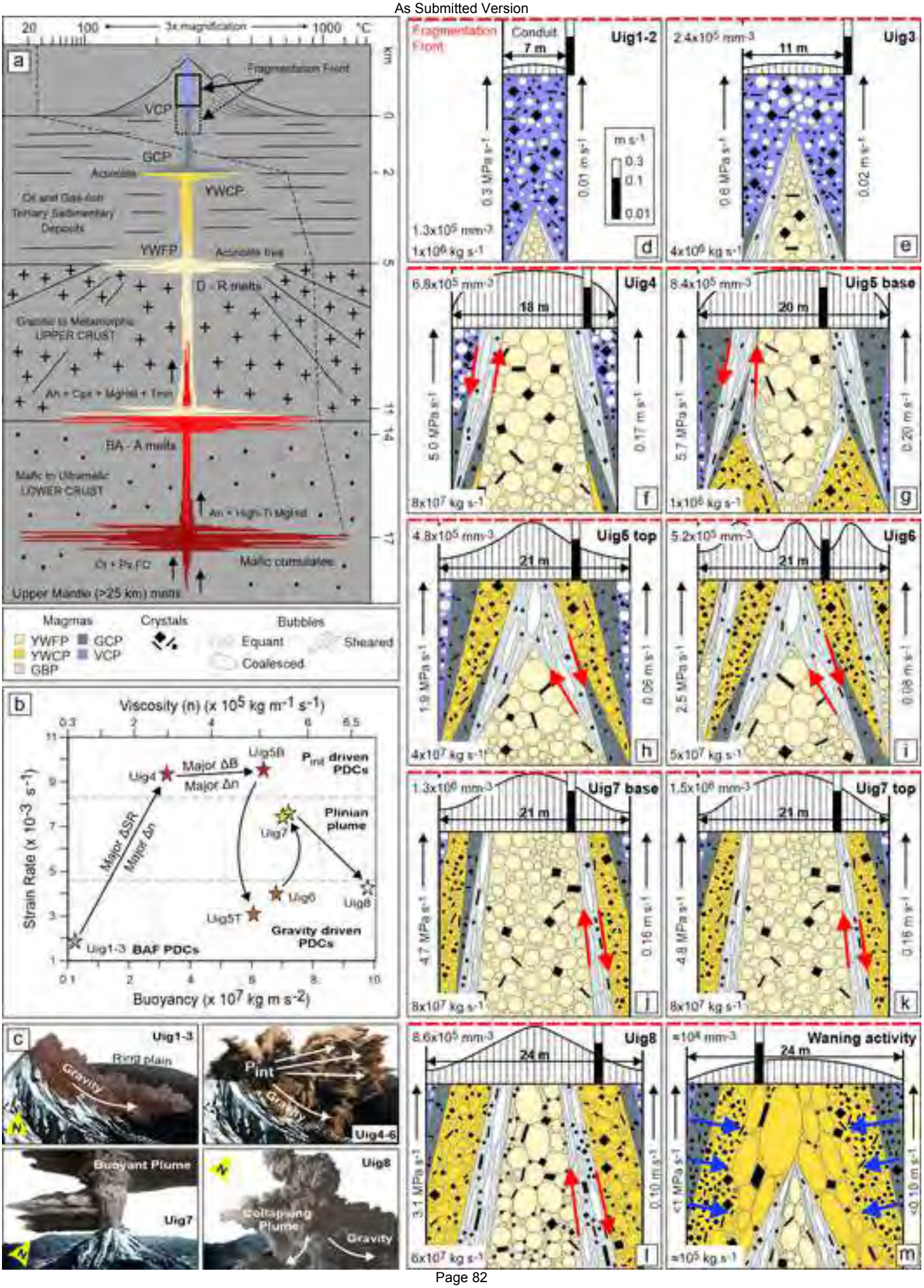
a
VCP
GCP
YWCP
YWFP
Fragmentation Front
Accretion
Oil and Gas-bearing Tertiary Sedimentary Deposits
Accretion lava
D - R melts
Granite to Metamorphic UPPER CRUST
An + Cpx + Mgrhbl + Trm
BA - A melts
Mafic to Ultramafic LOWER CRUST
An + High-Ti Mgrhbl
Ol + Px FC
Mafic cumulates
Upper Mantle (>25 km) melts
km
Magmas
YWFP
YWCP
GBP
GCP
VCP
Crystals
Bubbles
Equant
Coalesced
Sheared
b
Viscosity (η) (x 10^5 kg m^-1 s^-1)
Strain Rate (x 10^-3 s^-1)
Buoyancy (x 10^7 kg m s^-2)
Uig1-3 BAF PDCs
Uig4
Uig5B
Major ΔB
Major Δη
Major ΔSR
Major Δη
Pint driven PDCs
Plinian plume
Uig7
Uig6
Uig8
Uig5T
Gravity driven PDCs
c
Uig1-3
Ring plain
Gravity
N
Pint
+ Gravity
Uig4-6
Buoyant Plume
Uig7
Uig8
Collapsing Plume
Gravity
Fragmentation Front
Conduit
Uig1-2
7 m
0.3 MPa s-1
0.01 m s-1
m s-1
0.3
0.1
0.01
1.3x10^5 mm-3
1x10^6 kg s-1
d
2.4x10^5 mm-3
11 m
Uig3
0.6 MPa s-1
0.02 m s-1
4x10^6 kg s-1
e
6.8x10^5 mm-3
18 m
Uig4
5.0 MPa s-1
0.17 m s-1
8x10^7 kg s-1
f
8.4x10^5 mm-3
20 m
Uig5 base
5.7 MPa s-1
0.20 m s-1
1x10^6 kg s-1
g
4.8x10^5 mm-3
21 m
Uig6 top
1.9 MPa s-1
0.06 m s-1
4x10^7 kg s-1
h
5.2x10^5 mm-3
21 m
Uig6
2.5 MPa s-1
0.08 m s-1
5x10^7 kg s-1
i
1.3x10^6 mm-3
21 m
Uig7 base
4.7 MPa s-1
0.16 m s-1
8x10^7 kg s-1
j
1.5x10^6 mm-3
21 m
Uig7 top
4.8 MPa s-1
0.16 m s-1
8x10^7 kg s-1
k
8.6x10^5 mm-3
24 m
Uig8
3.1 MPa s-1
0.10 m s-1
6x10^7 kg s-1
l
≈10^6 mm-3
24 m
Waning activity
<1 MPa s-1
<0.10 m s-1
≈10^5 kg s-1
m



Figure 10